Chapter 5
Traditional Water Geothermometers and f_{CO_2}-Indicators

Abstract Traditional water geothermometers and f_{CO_2}-indicators have been thoroughly reviewed in this chapter. The solubility of different silica minerals has been recalled, but the main focus has been placed on quartz solubility, as it plays a pivotal role in water geothermometry, underscoring the effects of grain size, pH, and salinity. The different Na-K geothermometric functions proposed by different authors have been examined. Since they are all plausible, there is not a unique Na-K geothermometer, but an infinite number of Na-K geothermometers which are controlled by the exchange reaction between low-albite and variably ordered adularia, from fully ordered maximum-microcline to completely disordered high-sanidine. Consequently, there is also an infinite number of the other cation geothermometers which are controlled by exchange reactions involving adularia. In particular, the Na-K-Ca geothermometer has been split in the three separate Na-K, Na-Ca, and K-Ca functions, following the suggestions of Tonani (1980). It turns out that the Na-Ca and K-Ca geothermometers work for waters equilibrated with an unspecified Ca-Al-silicate at relatively low f_{CO_2} values, whereas they do not work for waters equilibrated with calcite under comparatively high f_{CO_2} values. This implies that the Na^2/Ca and K^2/Ca ratios represent the basis not only for geothermometers but also for f_{CO_2}-indicators, which is somewhat different from the point of view of previous authors. Although Mg concentration decreases considerably with increasing temperature, the K-Mg and Na-Mg geothermometers suffer several limitations due to different reasons, including the variable composition of chlorites and illites and the varying order-disorder of adularia, impacting the K-Mg geothermometer much more than the Na-Mg geothermometer. Hence, some words of caution are needed on the use of the very popular Na-K-$Mg^{1/2}$ triangular plot.

5.1 General Aspects of Geothermometers and f_{CO_2}-Indicators

Geothermometers and f_{CO_2}-indicators (sometimes improperly called geobarometers) are simple functions in which the chemical data of geothermal water samples are

R. Cioni and L. Marini, *A Thermodynamic Approach to Water Geothermometry*,
Springer Geochemistry, https://doi.org/10.1007/978-3-030-54318-1_5

inserted into to compute the temperature and f_{CO_2}, respectively, which are expected to be present in the zones of the geothermal aquifer where these geothermal water samples have presumably attained chemical equilibrium with hydrothermal minerals.

5.1.1 Basic Hypotheses of Geothermometry

As underscored by Fournier et al. (1974), "*There are many basic assumptions inherent in using geochemical indicators to estimate subsurface temperatures …. The usual assumptions are*:

1. *Temperature-dependent reactions occur at depth.*
2. *All constituents involved in a temperature-dependent reaction are sufficiently abundant (that is, supply is not a limiting factor).*
3. *Water-rock equilibration occurs at the reservoir temperature.*
4. *Little or no re-equilibration or change in composition occurs at lower temperatures as the water flows from the reservoir to the surface.*
5. *The hot water coming from deep in the system does not mix with cooler shallow ground water*."

The f_{CO_2}-indicators rely on similar hypotheses. Often, the hypotheses 4 and 5 are not satisfied, especially for thermal springs. In fact, the geothermal liquid frequently mixes with shallow waters or separates a vapor phase or precipitates one or more mineral phases, during the ascent towards the surface. If so, the effects of these secondary processes have to be properly modeled for a correct application of geothermometers and f_{CO_2}-indicators as already recognized by Fournier and Truesdell (1974).

The purpose of this chapter is to review the traditional geothermometers and f_{CO_2}-indicators, both to provide a picture of the present state of the art and to underscore the needs for possible improvements.

5.1.2 Historical Overview

The first attempt to use silica as a water geothermometer was probably done by Bödvarsson (1960) and Bödvarsson and Palmason (1961) who adopted the concentration of dissolved SiO_2, c_{SiO_2}, of the thermal springs in the low temperature areas in Iceland as an indicator of aquifer temperature, T, using the simple relation (c_{SiO_2} in mg/kg; T in °C): $T = c_{SiO_2} - 25$. However, this can be considered a qualitative geothermometer at best.

Morey et al. (1962) investigated the solubility of quartz in water, in the temperature range from 25 to 300 °C, by means of laboratory experiments. They calibrated two quartz solubility relations, one at P_{H_2O} of 1000 atm, the other at water saturation pressure using the results of their own experiments and those of Kennedy (1950).

In the conclusive section of the paper, Morey et al. (1962) wrote that "*it is probable that the silica contents of many hot springs are controlled by equilibrium between dissolved silica and quartz at relatively shallow depths where temperatures are above* 150 °C. *The waters from many springs and geysers in Yellowstone National Park are unsaturated in silica with respect to silica gel at the vent temperatures,* 80°–95 °C. *However, these waters are saturated in silica with respect to the solubility of quartz at temperatures of* 175°–275 °C." For the first time, quartz solubility was used as a real geothermometer.

Mahon (1966) utilized the quartz solubility curves of Morey et al. (1962) and the dissolved silica concentration in waters discharged from the geothermal wells of Wairakei, New Zealand, suitably corrected for steam separation, to evaluate the temperatures present in the geothermal reservoir. Fournier and Rowe (1966) described the method for calculating aquifer temperatures from the silica concentration of high-discharge, boiling springs and wet-steam wells assuming equilibrium with quartz at depth. The quartz geothermometer was thus thoroughly established and tested in the 60s. Since then, dissolved silica in hot spring waters and geothermal well discharges has been extensively used as a tool to estimate aquifer temperature.

More or less at the same time, it was observed that the Na/K concentration ratio of thermal waters decreases with increasing temperature and tables and/or diagrams displaying the atomic Na/K ratios versus temperature were generated using both results of laboratory experiments and water compositions of geothermal wells and hot springs (White 1965, 1968; Ellis and Mahon 1967; Ellis 1970; Mercado 1970). The ion exchange reaction between coexisting Na- and K-feldspars was generally invoked to explain the Na/K ratio—temperature relation (e.g., White 1965; Ellis 1970). Nevertheless, the possible role of Na and K micas instead of one of the two feldspars or both of them was discussed by Fournier and Truesdell (1970). These authors underscored also the changes in the Na/K ratio during the ascent of thermal waters from the deep aquifer to the surface discharge due to mineral-solution reactions as well as the possible effects of complex ion formation.

The studies of hydrothermal alteration mineralogy (e.g., Browne 1970, 1978) and geochemical modeling of mineral-solution equilibria and irreversible mass transfer during water-rock interaction in high-temperature hydrothermal systems (e.g., Helgeson, 1968, 1969; Helgeson et al. 1969, 1970) provided further evidence on the role of temperature-dependent reactions involving hydrothermal minerals and aqueous species in controlling water geothermometers.

Based on this knowledge, the solubility of different SiO_2 polymorphs in water was used to calibrate silica geothermometers (e.g., Fournier and Rowe 1962; Fournier 1973; Arnórsson 1970, 1975; Fournier and Potter 1982a, b; Arnórsson et al. 1983a) and ion exchange reactions involving suitable hydrothermal minerals were invoked to derive or substantiate ionic solute geothermometers, such as the Na–K geothermometer (e.g., Fournier 1979; Arnórsson et al. 1983a; Giggenbach 1988), the Na–K–Ca geothermometer (Fournier and Truesdell 1973), and the K–Mg geothermometer (Giggenbach et al. 1983; Giggenbach 1988), as well as the K–Ca f_{CO_2}-indicator (Giggenbach 1984, 1988).

These simple functions have been used in a countless number of studies and are still widely used today although some limitations became apparent through the years. Finally, a theoretical justification for ionic solute geothermometers and f_{CO_2}-indicators was found by Guidi et al. (1990) and Chiodini et al. (1991) who elaborated on the early suggestion of Fournier and Truesdell (1970) concerning the possible influence of complex ion formation.

5.1.3 *The Simple Form of Most Geothermometric Equations*

Although polynomial equations were used for some geothermometers, such as the quartz solubility functions of Fournier and Potter (1982a, b), Von Damm et al. (1991), Manning (1994), Shibue (1996), and Gunnarsson and Arnórsson (2000) (see Sect. 5.2.2) and the Na–K geothermometer of Arnórsson (2000; see Sect. 5.3.1), most geothermometers are written in the simple form:

$$\mathrm{T(^\circ C)} = \frac{\mathrm{A}}{\log \mathrm{K} - \mathrm{B}} - 273.15. \tag{5.1}$$

In Eq. (5.1), K is the thermodynamic equilibrium constant of the reaction controlling the geothermometer and the meaning of A and B constitutes the subject of this discussion. Suitable examples are the dissolution reactions of quartz and chalcedony:

$$\text{quartz} = \mathrm{SiO_{2(aq)}} \tag{5.2}$$

$$\text{chalcedony} = \mathrm{SiO_{2(aq)}} \tag{5.3}$$

and the albite-adularia exchange reaction:

$$\text{albite} + \mathrm{K^+} = \text{adularia} + \mathrm{Na^+}. \tag{5.4}$$

The thermodynamic equilibrium constants of reactions (5.2), (5.3), and (5.4) can be written in the following simplified forms:

$$\mathrm{K_{Qtz}} \cong m_{\mathrm{SiO_{2(aq)}}} \tag{5.5}$$

$$\mathrm{K_{Chc}} \cong m_{\mathrm{SiO_{2(aq)}}} \tag{5.6}$$

$$\mathrm{K_{Ab-Adl}} \cong m_{\mathrm{Na^+}} \big/ m_{\mathrm{K^+}} \tag{5.7}$$

assuming that: (i) solid phases are pure (see Sect. 2.1.2), which is reasonable for silica minerals and alkali feldspars (see Sects. 4.2, and 4.10), (ii) the activity coefficient of dissolved silica is 1, which is realistic for neutral species (see Sect. 2.3.3), and (iii) the activity coefficients of Na^+ and K^+ ions are nearly equal, which is true (or nearly so) for ions of the same charge if the B-dot equation is used (see Sect. 2.3.3).

As already recalled in Sect. 2.1.4, the temperature dependence of the thermodynamic equilibrium constant K of any reaction is expressed by the van't Hoff relation, Eq. (2.22). Assuming that the standard isobaric heat capacity of the reaction, $\Delta C^{o}_{P,r}$, is equal to zero, Eq. (2.22) is easily integrated and rearranged, obtaining:

$$\log K_T = -\frac{\Delta H^o_r}{2.303 \cdot R \cdot T} + \log K_{T_r} + \frac{\Delta H^o_r}{2.303 \cdot R \cdot T_r}. \tag{5.8}$$

The natural logarithm of the thermodynamic equilibrium constant and the standard Gibbs free energy of reaction, ΔG°_r, are linked by Eq. (2.12), which can be written in the following form, for $T = T_r$ and adopting the decimal logarithm of K instead of its natural logarithm:

$$\log K_{T_r} = -\frac{\Delta G^o_r}{2.303 \cdot R \cdot T_r}. \tag{5.9}$$

Let us now insert Eq. (5.9) into Eq. (5.8) and reorganize the obtained relation, recalling Eq. (2.1) rewritten for $T = T_r$:

$$\Delta G^o_r = \Delta H^o_r - T_r \cdot \Delta S^o_r. \tag{5.10}$$

In this way, one finds:

$$\log K_T = -\frac{\Delta H^o_r}{2.303 \cdot R \cdot T} + \frac{\Delta S^o_r}{2.303 \cdot R}. \tag{5.11}$$

Let us now solve Eq. (5.1) with respect to log K expressing the temperature in Kelvin degrees:

$$\log K = \frac{A}{T(K)} + B. \tag{5.12}$$

Comparison of Eqs. (5.11) and (5.12) shows that:

$$A = -\frac{\Delta H^o_r}{2.303 \cdot R} \tag{5.13}$$

$$B = \frac{\Delta S^o_r}{2.303 \cdot R}. \tag{5.14}$$

In other terms, the linear relation between the logarithm of the thermodynamic equilibrium constant and the inverse of the absolute temperature implies that the standard enthalpy and entropy of reaction are constant. This findings are expected because: (i) $\Delta C_P{}^{\circ}{}_r$ was assumed equal to zero in the integration of the van't Hoff equation (see above) and (ii) $\Delta C_P{}^{\circ}{}_r$ is related to the enthalpy and entropy of reaction through the relations:

$$\left(\frac{\partial\left(\Delta H_r^o\right)}{\partial T}\right)_P = \Delta C_{P,r}^o \tag{5.15}$$

$$\left(\frac{\partial\left(\Delta S_r^o\right)}{\partial T}\right)_P T = \Delta C_{P,r}^o. \tag{5.16}$$

The condition $\Delta C_P{}^{\circ}{}_r = 0$ is usually true for isocoulombic reactions, that is for reactions having the same number of ionic species of the same charge on each side. In fact, reactions (5.2), (5.3), and (5.4), and similar reactions, are isocoulombic (Puigdomènech et al. 1997). Therefore, it is reasonable to assume that the log K of these reactions, and of similar reactions as well, depends linearly on the inverse of the absolute temperature. In other terms, it is permissible to adopt Eqs. (5.1) and (5.12) for the silica and Na–K geothermometers.

5.2 The Silica Geothermometers

According to Fournier (1991), in some geothermal reservoirs, well-crystalline quartz controls undissociated SiO_2 concentration at temperatures as low as 100 °C, probably because water has been in contact with rocks for comparatively long lapses of time, whereas chalcedony (i.e., microcrystalline quartz with sub-microscopic pores) governs undissociated SiO_2 concentration up to 180 °C in the portions of geothermal systems recently affected by fracturing. Chalcedony is more soluble than quartz because the small size of its microcrystals determines large surface energies.

According to Arnórsson et al. (1983a), quartz solubility governs undissociated SiO_2 concentration above about 180 °C, whereas geothermal waters circulating in aquifers of relatively low temperatures attain metastable equilibrium with chalcedony instead of quartz.

Other silica minerals, such as α-cristobalite, opal-CT, and amorphous silica, occur in geothermal systems and may control undissociated SiO_2 concentration especially at comparatively low temperatures and/or in acidic solutions.

5.2.1 *Constant-Enthalpy Relations Expressing the Solubility of Silica Minerals in Pure Water*

The logarithm of total dissolved silica concentration in pure water in equilibrium with vapor and a silica mineral (i.e., quartz, chalcedony, α-cristobalite, opal-CT, and amorphous silica) increases linearly with decreasing values of the absolute temperature inverse, as shown by the solid black lines in Fig. 5.1. In the same diagram, the dashed blue lines apply to waters that were initially in equilibrium with these silica minerals at the considered temperatures and have experienced single-step steam separation at 100 °C, or maximum steam loss.

The solid black straight lines in Fig. 5.1 correspond to the following geothermometric functions, which were proposed by Fournier (1977) and references therein and are valid in the temperature range 0–250 °C (T is temperature, in °C, and c_{SiO_2} is total dissolved silica concentration, in mg/kg):

$$T_{Qz,F} = \frac{1309}{5.19 - \log c_{SiO_2}} - 273.15, \quad \text{for quartz} \tag{5.17}$$

$$T_{Chc,F} = \frac{1032}{4.69 - \log c_{SiO_2}} - 273.15, \text{for chalcedony} \tag{5.18}$$

$$T_{\alpha-Crs,F} = \frac{1000}{4.78 - \log c_{SiO_2}} - 273.15, \text{for}\,\alpha\text{-cristobalite} \tag{5.19}$$

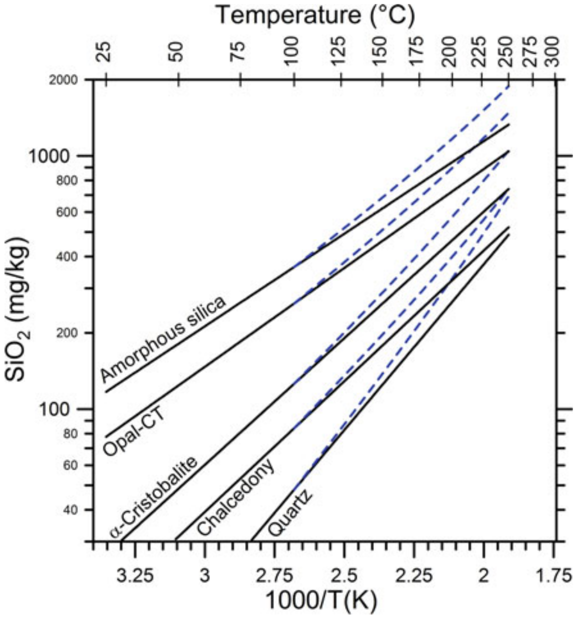

Fig. 5.1 Solid black lines indicate the solubility of several silica minerals in water, at the vapor pressure of the solution, as expressed by Eqs. (5.17)–(5.21). Dashed blue lines refer to the corresponding maximum steam loss relations, that is Eqs. (5.22)–(5.26). Equations (5.17)–(5.22) are from Fournier (1977) whereas Eqs. (5.23)–(5.26) were derived in this work

$$\mathrm{T_{Opl,F}} = \frac{781}{4.51 - \log \mathrm{c_{SiO_2}}} - 273.15, \text{ for opal - CT} \tag{5.20}$$

$$\mathrm{T_{A-SiO_2,F}} = \frac{731}{4.52 - \log \mathrm{c_{SiO_2}}} - 273.15, \text{ for amorphous silica.} \tag{5.21}$$

The plot of Fig. 5.1 and Eqs. (5.17)–(5.21) indicate that, among the silica minerals, amorphous silica has the highest solubilities, quartz has the lowest solubilities, while chalcedony, α-cristobalite, and opal-CT exhibit intermediate solubilities.[1]

Fournier (1977) and references therein proposed also the following maximum-steam-loss quartz geothermometer:

$$\mathrm{T_{Qz,msl,F}} = \frac{1522}{5.75 - \log \mathrm{c_{SiO_2}}} - 273.15. \tag{5.22}$$

Similar maximum-steam-loss geothermometric functions for the other silica minerals, corresponding to the dashed blue lines in Fig. 5.1, are as follows (this work):

$$\mathrm{T_{Chc,msl,F}} = \frac{1227}{5.20 - \log \mathrm{c_{SiO_2}}} - 273.15, \text{ for chalcedony} \tag{5.23}$$

$$\mathrm{T_{\alpha\text{-}Crs,msl,F}} = \frac{1195}{5.29 - \log \mathrm{c_{SiO_2}}} - 273.15, \text{ for } \alpha\text{-cristobalite} \tag{5.24}$$

$$\mathrm{T_{Opl,msl,F}} = \frac{976}{5.02 - \log \mathrm{c_{SiO_2}}} - 273.15, \text{ for opal - CT} \tag{5.25}$$

$$\mathrm{T_{Am.SiO_2,msl,F}} = \frac{926}{5.03 - \log \mathrm{c_{SiO_2}}} - 273.15, \text{ for amorphous silica.} \tag{5.26}$$

Based on data from geothermal wells in Iceland, Arnórsson et al. (1983a) performed an empirical calibration of the chalcedony geothermometer obtaining the following function:

$$\mathrm{T_{Chc,A}} = \frac{1112}{4.91 - \log \mathrm{c_{SiO_2}}} - 273.15, \tag{5.27}$$

which is valid from 25 to 180 °C. Arnórsson et al. (1983a) did not calibrate the quartz geothermometer, because their analytical data were inadequate, but recommended the use of the following function, in the temperature range 180–300 °C:

$$\mathrm{T_{Qz,A}} = \frac{1164}{4.90 - \log \mathrm{c_{SiO_2}}} - 273.15. \tag{5.28}$$

---

[1] Opal-CT was identified as β-cristobalite by Fournier (1977), but this erroneous identification was corrected in later papers.

Rimstidt (1997) presented results for quartz solubility measurements in pure water at 21, 50, 74, and 96 °C and 1 bar, in which equilibrium was attained from undersaturation. The duration of the two runs at 21 °C was 4917 days (~13.5 years) whereas the other runs lasted 54 to 210 days. Rimstidt's results indicate that quartz solubility at 25 °C is 11.0 ± 1.1 mg/kg, which is significantly higher than the results given by Eq. (5.17), 6.3 mg/kg, and Eq. (5.28), 9.9 mg/kg, although the latter should not be used at 25 °C.

Rimstidt (1997) reviewed the available experimental data for the temperature range 0–300 °C and obtained the following linear regression relationship ($N = 71$; $R^2 = 0.994$):

$$\mathrm{Log}\, m_{\mathrm{SiO_{2(aq)}}} = -1107.12(\pm 10.77) \cdot \mathrm{T}^{-1} - 0.0254(\pm 0.0247). \tag{5.29}$$

Equation (5.29) corresponds to the following geothermometric relation:

$$\mathrm{T_{Qz,R}} = \frac{1107.12}{4.753 - \log c_{\mathrm{SiO_2}}} - 273.15, \tag{5.30}$$

in which the uncertainties are disregarded.

Strictly speaking, undissociated silica concentration, $c_{\mathrm{SiO_{2(aq)}}}$, should appear in silica geothermometers instead of total dissolved silica concentration, $c_{\mathrm{SiO_2}}$, because the equilibrium condition between the aqueous solution and the considered silica mineral, $\mathrm{SiO_{2(s)}}$, involves undissociated silica, $\mathrm{SiO_{2(aq)}}$, as expressed by the following general reaction:

$$\mathrm{SiO_{2(s)}} = \mathrm{SiO_{2(aq)}}. \tag{5.31}$$

Reactions (5.2) and (5.3) involve quartz and chalcedony, respectively, and are special cases of the general reaction (5.31). The thermodynamic equilibrium constant of reaction (5.31) can be considered nearly equal to $\mathrm{SiO_{2(aq)}}$ molality:

$$\mathrm{K_{SiO_{2(s)}}} \cong m_{\mathrm{SiO_{2(aq)}}} \tag{5.32}$$

for the reasons already given above for Eqs. (5.5) and (5.6).

To investigate the relation between the concentrations of total dissolved silica and undissociated silica (or silicic acid) as a function of pH, we write the dissociation reaction of undissociated silica:

$$\mathrm{SiO_{2(aq)}} + \mathrm{H_2O} = \mathrm{H^+} + \mathrm{HSiO_3^-} \tag{5.33}$$

and the corresponding thermodynamic equilibrium constant:

$$\mathrm{K} = \frac{a_{\mathrm{HSiO_3^-}} \cdot a_{\mathrm{H^+}}}{a_{\mathrm{SiO_{2(aq)}}} \cdot a_{\mathrm{H_2O}}}. \tag{5.34}$$

Assuming that the aqueous solution is relatively dilute, then $a_{H_2O} = 1$. Hypothesizing that activity coefficients are equal or close to 1, and recalling that $a_{H^+} = 10^{-pH}$ and $K = 10^{-pK}$, Eq. (5.34) can be rearranged as:

$$\frac{m_{HSiO_3^-}}{m_{SiO_{2(aq)}}} = \frac{10^{-pK}}{10^{-pH}} = 10^{pH-pK} \tag{5.35}$$

Consequently, the following conditions hold true: $m_{HSiO_3^-} = m_{SiO_{2(aq)}}$ at pH = pK, $m_{HSiO_3^-} = 0.1 \cdot m_{SiO_{2(aq)}}$ at pH = pK − 1, $m_{HSiO_3^-} = 0.01 \cdot m_{SiO_{2(aq)}}$ at pH = pK − 2, and so on. For instance, since pK = 9.04 at 250 °C, it follows that $m_{SiO_{2(aq)}} = m_{HSiO_3^-}$ at pH = 9.04, $m_{HSiO_3^-} = 0.1 \cdot m_{SiO_{2(aq)}}$ at pH = 8.04, $\mathrm{m}_{HSiO_3^-} = 0.01 \cdot m_{SiO_{2(aq)}}$ at pH = 7.04, and so on. Since, the pK of silicic acid dissociation varies from 10.3 to 8.8, in the 0–350 °C range (Fig. 5.2) and the pH of reservoir liquids is usually in the range 5–7, being constrained by water-rock reactions, in general, total dissolved SiO_2 concentration is nearly equal to undissociated SiO_2 concentration, under reservoir conditions.

However, loss of acid gases (CO_2 and H_2S) upon steam separation (boiling) increases significantly the pH of the liquid phase. Upon attainment of pH values higher than 7.8–9.3, depending on temperature, total dissolved silica concentration becomes significantly greater than undissociated silica concentration due to the presence of significant amounts of silicate ion produced through reaction (5.33). Therefore, it is advisable to insert undissociated silica concentration into silica geothermometers instead of total dissolved silica concentration, to get rid of these possible pH effects. The pH effect on quartz solubility was underscored *inter alias* by Crerar

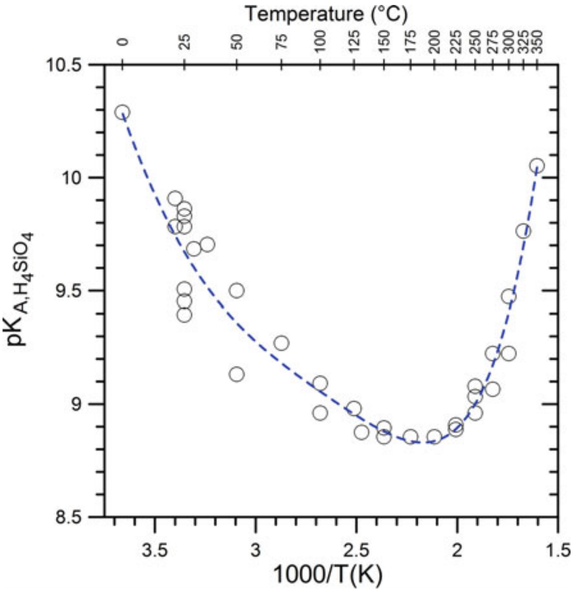

Fig. 5.2 Temperature dependence of the pK of the silicic acid dissociation (reaction 5.33), based on different experimental data (from Fleming and Crerar 1982 and references therein)

and Anderson (1971), who determined quartz solubility in the SiO_2–H_2O–NaOH system, and Arnórsson (1975), who discussed the increase in pH upon flashing due to extensive removal of dissolved CO_2 and H_2S from liquid water into the vapor phase.

The linear relation between the absolute temperature inverse and log c_{SiO_2} or log $c_{SiO_{2(aq)}}$, for all the silica geothermometers, is due to the fact that reaction (5.31) is isocoulombic, as already underscored in Sect. 5.1.3. Besides, based on Eq. (5.13):

(i) The slope of the quartz and chalcedony geothermometers of Fournier (1977), Eqs. (5.17) and (5.18), respectively, is consistent with ΔH°_r values of 5991 cal mol^{-1} and 4723 cal mol^{-1}, respectively, for the corresponding dissolution reactions.

(ii) The slope of the quartz and chalcedony geothermometric functions of Arnórsson et al. (1983a), Eqs. (5.27) and (5.28), respectively, is consistent with ΔH°_r values of 5327 cal mol^{-1} and 5089 cal mol^{-1}, respectively, for the dissolution reactions of these two silica minerals.

(iii) The slope of the quartz geothermometer of Rimstidt (1997), Eqs. (5.30), is consistent with a ΔH°_r value of 5067 cal mol^{-1} for the dissolution reaction of quartz.

In Fig. 5.3, these enthalpies of quartz and chalcedony dissolution are compared with those predicted by SUPCRT92 (Johnson et al. 1992) as a function of temperature, at water saturation pressure, based on the thermodynamic properties of Helgeson et al. (1978). From 100 to 275 °C, the ΔH°_r values of the quartz and chalcedony geothermometers of Arnórsson et al. (1983a), the chalcedony geothermometer of Fournier (1977), and the quartz geothermometer of Rimstidt (1997) agree with the ΔH°_r values given by SUPCRT92 for quartz and chalcedony, 5150 ± 87 and 4782 ± 87 cal mol^{-1},

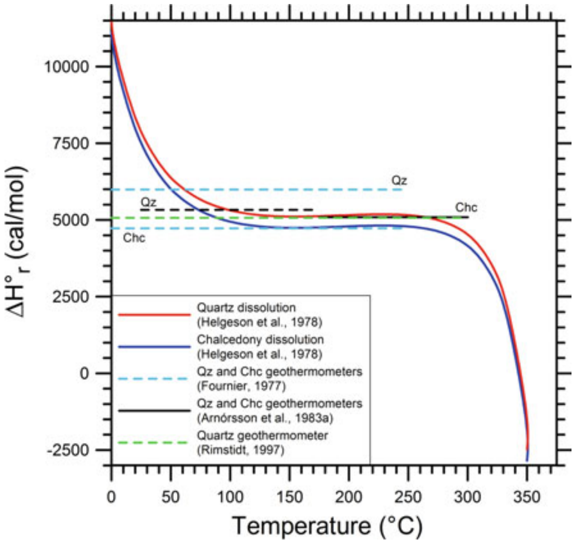

Fig. 5.3 Enthalpy of quartz and chalcedony dissolution predicted by SUPCRT92 as a function of temperature, at water saturation pressure, based on the thermodynamic properties of Helgeson et al. (1978) and ΔH°_r values consistent with the quartz and chalcedony geothermometers of Fournier (1977) and Arnórsson et al. (1983a) and the quartz geothermometer of Rimstidt (1997)

respectively, on average. In contrast, the $\Delta H°_r$ values of the quartz geothermometer of Fournier (1977) is higher than the $\Delta H°_r$ values of quartz dissolution computed using SUPCRT92 by 820 cal mol^{-1} on average.

To be noted that the $\Delta H°_r$ values of SUPCRT92 show limited variations in the temperature range 100–275 °C, whereas the SUPCRT92 enthalpies deviate progressively from the $\Delta H°_r$ values of silica geothermometers towards higher values below 100 °C and towards lower values above 275 °C. Therefore, based on SUPCRT92 predictions, the constant-enthalpy quartz and chalcedony geothermometers are expected to give increasingly wrong results both below 100 °C and above 275 °C.

5.2.2 *Variable-Enthalpy Relations Expressing Quartz Solubility in Pure Water*

Since the constant-enthalpy silica geothermometers do not describe properly the solubility of quartz and chalcedony below 100 °C and above 275 °C, variable-enthalpy relations were proposed by Fournier and Potter (1982a, b), Von Damm et al. (1991), Manning (1994), Shibue (1996), and Gunnarsson and Arnórsson (2000). The first four of these equations involve the density of H_2O or its molar volume and reproduce quartz solubility both in the liquid and vapor phases.

Fournier and Potter (1982a) used the experimental results obtained by different authors (Kennedy 1950; Morey and Hesselgesser 1951a; Wyart and Sabatier 1955; Khitarov 1956; Kitahara 1960; Van Lier et al. 1960; Morey et al. 1962; Siever 1962; Weill and Fyfe 1964; Anderson and Burnham 1965; Heitmann 1965; Stewart 1965, unpublished data; Semonova and Tsilkis, 1970; Crerar and Anderson 1971; Seward 1974; Hemley et al. 1980) at temperatures from 20 to 900 °C and at pressures up to 10 kbar, to express quartz solubility in pure water as a function of the absolute temperature and the specific volume of pure water, either liquid or gaseous, through the following relation:

$$\log m_{\mathrm{SiO_2}} = \mathrm{A} + \mathrm{B} \cdot \log \mathrm{V} + \mathrm{C} \cdot (\log \mathrm{V})^2 \tag{5.36}$$

where V is the specific volume of H_2O ($cm^3\ g^{-1}$), and:

$$\begin{aligned}
\mathrm{A} &= -4.66206 + 0.0034063 \cdot \mathrm{T} + 2179.7 \cdot \mathrm{T}^{-1} \\
&\quad - 1.1292 \times 10^6 \cdot \mathrm{T}^{-2} + 1.3543 \times 10^8 \cdot \mathrm{T}^{-3} \\
\mathrm{B} &= -0.0014180 \cdot \mathrm{T} - 806.97 \cdot \mathrm{T}^{-1} \\
\mathrm{C} &= 3.9465 \times 10^{-4} \cdot \mathrm{T}.
\end{aligned}$$

Inserting the specific volume of pure water, at saturation temperatures and pressures, from Lemmon et al. (2017)[2] into Eq. (5.36), computed quartz solubility in the

---

[2] Data were obtained from the website https://webbook.nist.gov/chemistry/fluid/

liquid phase increases gradually with temperature, up to a maximum of 771.2 mg/kg at 339 °C, and decreases quickly above 360 °C, attaining a value close to 310 mg/kg at the critical temperature of pure water, 374 °C.[3] In contrast, the solubility of quartz in steam is less than 1 mg/kg below 270 °C and increases steeply close to the critical temperature, reaching 10.0 mg/kg at 322 °C, 30.7 mg/kg at 347 °C, 103.4 mg/kg at 368 °C, and 259.5 mg/kg at 373.9 °C.

In a separate scientific paper, Fournier and Potter (1982b) used the equation of Fournier and Potter (1982a) to compute the solubility of quartz in pure H_2O, at the vapor pressure of the solution, in both the liquid and gas (steam) phases, at 5 °C intervals up to the critical point. The obtained results are closely reproduced by the following polynomial function:

$$T_{Qz,FP} = C_1 + C_2 \cdot c_{SiO_2} + C_3 \cdot c_{SiO_2}^2 + C_4 \cdot c_{SiO_2}^3 + C_5 \cdot \log c_{SiO_2} \qquad (5.37)$$

in which $T_{Qz,FP}$ is in °C, $C_1 = -4.2198 \times 10^1$, $C_2 = 2.8831 \times 10^{-1}$, $C_3 = -3.6686 \times 10^{-4}$, $C_4 = 3.1665 \times 10^{-7}$, and $C_5 = 7.7034 \times 10^1$. The quartz geothermometer of Fournier and Potter (1982b), i.e., Eq. (5.37), can be applied to dilute aqueous solutions in the temperature range 20–330 °C.

As detailed in the next section, Von Damm et al. (1991) derived an equation describing quartz solubility in NaCl solutions of molality up to 0.5 m, which can be applied to pure water as well. Inserting the specific volume of pure water, at saturation temperatures and pressures, from Lemmon et al. (2017) into Eq. (5.41), calculated quartz solubility in liquid water increases gradually with temperature, up to a maximum of 739.0 mg/kg at 343 °C, and decreases rapidly above 360 °C, attaining a value close to 329 mg/kg at the critical temperature of pure water. In contrast, the solubility of quartz in steam is <1 mg/kg below 263 °C and increases steeply near the critical temperature, attaining 10.2 mg/kg at 319 °C, 30.0 mg/kg at 344 °C, 105.7 mg/kg at 367 °C, and 278.3 mg/kg at 373.9 °C.

Manning (1994) measured the solubility of quartz in pure water at pressures of 5 to 20 kbar and temperatures of 500 to 900 °C by means of crushed-quartz and single-crystal experiments. He considered the results of his experiments, those of Hemley et al. (1980) and Walther and Orville (1983) as well as the quartz solubilities computed at 25, 50, 100, and 150 °C, up to 5 kbar, by means of the equation of Fournier and Potter (1982a). Manning (1994) regressed all these data against T (in K) and ρ_{H_2O} (in g cm^{-3}) obtaining the following relation:

$$\log m_{SiO_2} = A(T) + B(T) \cdot \log \rho_{H_2O} \qquad (5.38)$$

where

$$A(T) = 4.2620 - \frac{5764.2}{T} + \frac{1.7513 \times 10^6}{T^2} - \frac{2.2869 \times 10^8}{T^3}$$

---

[3] The SiO_2 concentration at the critical point was computed by averaging the values of the liquid and vapor at 373.9 °C.

$$B(T) = 2.8454 - \frac{1006.9}{T} + \frac{3.5689 \times 10^5}{T^2}.$$

According to Manning (1994), Eq. (5.38) reproduces measured quartz solubilities up to 20 kbar and 900 °C and can be extrapolated to pressures higher than 20 kbar. Inserting the specific volume of pure water, at saturation temperatures and pressures, from Lemmon et al. (2017) into Eq. (5.38), quartz solubility in the liquid phase growths progressively with temperature, up to a maximum of 700 mg/kg at 341 °C, and decreases rapidly above 360 °C, attaining a value close to 263 mg/kg at the critical temperature of pure water. In contrast, the solubility of quartz in the gas phase is less than 1 mg/kg below 292 °C and rises suddenly near the critical temperature, reaching 10.3 mg/kg at 337 °C, 30.5 mg/kg at 356 °C, 104.1 mg/kg at 371 °C, and 215.3 mg/kg at 373.9 °C.

Shibue (1996) used 424 experimental data on quartz solubility in pure water from different studies (Kennedy 1950; Morey and Hesselgesser 1951a, b; Wyart and Sabatier 1955; Morey et al. 1962; Siever 1962; Weill and Fyfe 1964; Anderson and Burnham 1965, 1967; Crerar and Anderson 1971; Novgorodov 1975, 1977; Hemley et al. 1980; Ragnarsdottir and Walther 1983; Walther and Orville 1983; Manning 1994) and derived the following equation (T in K; P in bar; ρ_{H_2O} in g cm^{-3}):

$$\begin{aligned}\ln m_{SiO_2} = {} & -1.51914 + 1.99970 \cdot \ln \rho_{H_2O} \\ & - \frac{2636.78}{T} + 0.00387766 \cdot T + \frac{0.0198582 \cdot P}{T}\end{aligned} \tag{5.39}$$

which is valid up to 10 kbar and 900 °C. Inserting the density of pure water, at saturation temperatures and pressures, from Lemmon et al. (2017) into Eq. (5.39), quartz solubility in liquid water increments more and more with temperature, up to a maximum of 720.6 mg/kg at 341 °C, and decreases quickly above 360 °C, attaining a value close to 289 mg/kg at the critical temperature of pure water. In contrast, the solubility of quartz in steam is <1 mg/kg below 279 °C and increases abruptly approaching the critical temperature, attaining 10.3 mg/kg at 330 °C, 31.0 mg/kg at 352 °C, 108.3 mg/kg at 370 °C, and 239.5 mg/kg at 373.9 °C.

Gunnarsson and Arnórsson (2000) considered the experimental data on quartz solubility in water from several studies (Kennedy 1950; Fournier 1960; Kitahara 1960; Van Lier et al. 1960; Morey et al. 1962; Siever 1962; Crerar and Anderson 1971; Mackenzie and Gees 1971; Hemley et al. 1980; Rimstidt 1997; Gíslason et al. 1997) and proposed the following relation (T in K):

$$\log m_{SiO_2(aq)} = -34.188 + 197.47 \cdot T^{-1} - 5.851 \times 10^{-6} \cdot T^2 + 12.245 \cdot \log T. \tag{5.40}$$

Equation (5.40) is valid at water saturation pressure in the temperature range 0 to 350 °C.

All the functions expressing quartz solubility in pure water, both the constant-enthalpy relations presented in the previous section and the variable-enthalpy equations introduced in this section, are shown in the diagrams of SiO_2 concentration versus temperature of Fig. 5.4 and SiO_2 concentration (in logarithmic scale) versus the absolute temperature inverse of Fig. 5.5.

The solubility of quartz and chalcedony, at saturation temperatures and pressures, computed by means of the program SUPCRT92 (Johnson et al. 1992), based on the thermodynamic data of quartz and chalcedony from Helgeson et al. (1978) and those of aqueous SiO_2 from Shock et al. (1989), are also displayed in this diagram, together with the results of the polynomial Eq. (4.57) in Sect. 4.10.2, describing the solubility of a mechanical mixture constituted by 50% chalcedony and 50% quartz, called quartz/chalcedony in brief, at saturation temperatures and pressures.

Apart from the equation of Shibue (1996) below ~160 °C and the relations of Fournier (1977) and Fournier and Potter (1982a, b) below ~120 °C, all the functions describing quartz solubility in pure water are positioned between the solubility curves of quartz and chalcedony computed by means of SUPCRT92. This suggests that the differences between the experimental data of different authors might be ascribable,

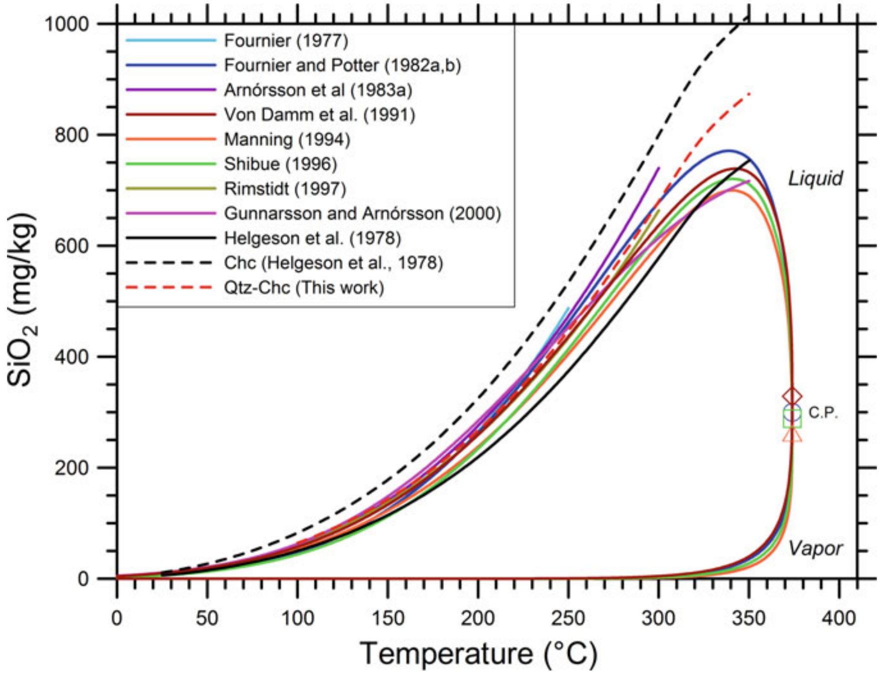

Fig. 5.4 Diagram of SiO_2 concentration versus temperature showing the constant-enthalpy and the variable-enthalpy equations expressing quartz solubility in pure water, at saturation temperatures and pressures. The blue circle, ruby red diamond, orange triangle, and green square indicate the SiO_2 concentration at critical point (C.P.) according to Fournier and Potter (1982a), Von Damm et al. (1991), Manning (1994), and Shibue (1996), respectively

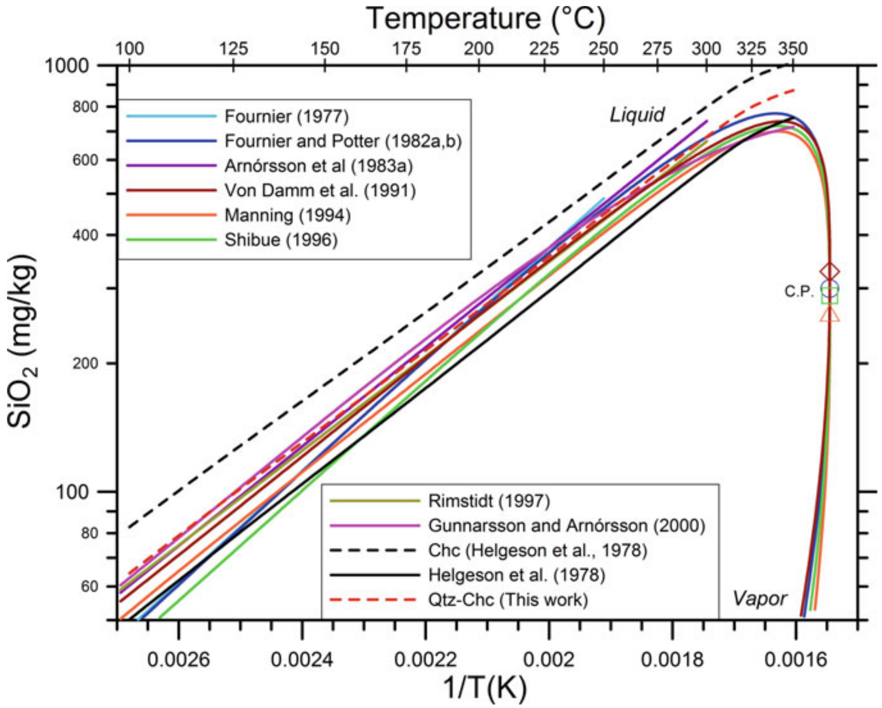

Fig. 5.5 Diagram of SiO_2 concentration (in logarithmic scale) versus absolute temperature inverse showing the constant-enthalpy and the variable-enthalpy equations describing quartz solubility in pure water, at saturation temperatures and pressures. The blue circle, ruby red diamond, orange triangle, and green square indicate the SiO_2 concentration at critical point (C.P.) according to Fournier and Potter (1982a), Von Damm et al. (1991), Manning (1994), and Shibue (1996), respectively

at least partly, to the different grain size of quartz crystals in equilibrium with the aqueous solution, as proposed by Azaroual et al. (1997) for the geothermal fluids of the Paris Basin. In fact, quartz microcrystals (i.e., chalcedony) are more soluble than quartz crystals, as already noted above. Accepting this explanation, it can be inferred that the quartz/chalcedony polynomial Eq. (4.57) describes the solubility of quartz crystals of average grain size, being representative of the central tendency.

The four variable-enthalpy relations of Fournier and Potter (1982a), Von Damm et al. (1991), Manning (1994), and Shibue (1996) reproduce the marked decrease in quartz solubility in the liquid phase and the steep increase in quartz solubility in the vapor phase occurring at temperatures approaching the critical point of pure water.

Moreover, the liquid and vapor branches of these four functions converge at the critical point, but there are considerable differences between the SiO_2 concentration value at the critical point, which varies from 263 to 329 mg/kg, as already noted above. In principle, SiO_2 concentrations in the liquid phase higher than the critical value correspond to two different temperatures of quartz equilibrium, one situated along the ascending part of the liquid branch of these four functions, the other positioned along the descending portion.

The other equations are characterized by a continuous increment of quartz solubility with increasing temperature and, consequently, they are unable to reproduce quartz solubility neither in the liquid phase at temperatures approaching the critical point nor in the vapor phase. Moreover, at temperatures higher than 250–275 °C there are large differences among these functions.

Consequently, the four variable-enthalpy equations of Fournier and Potter (1982a), Von Damm et al. (1991), Manning (1994), and Shibue (1996) can be applied up to the critical point of pure water, whereas the other relations cannot be used above temperatures varying from 250 to 350 °C, different from case to case.

5.2.3 *Quartz Solubility in Salt Solutions*

Fournier et al. (1982) measured the solubility of quartz in 2, 3, and 4 molal NaCl solutions at 350 °C and pressures varying from 180 to 500 bar using the gold bag hydrothermal apparatus of Seyfried et al. (1979). Quartz solubility in each of the considered NaCl solutions resulted to be greater than that in pure water over the whole pressure interval considered in the study, but the ratio between quartz solubility in NaCl solutions and in pure water decreases with increasing pressure. Fournier et al. (1982) underscored that the previous measurements of quartz solubility in NaCl solutions carried out by Kitahara (1960) are too high due to the high pH caused by reaction of elemental silver and NaCl with production of NaOH, AgCl, and H_2. According to Fournier et al. (1982), also quartz solubilities in NaCl solutions measured by Ganeyev (1975) might be affected by similar problems whereas quartz solubilities in NaCl solutions determined by Hemley et al. (1980) are reliable.

As anticipated in previous section, Von Damm et al. (1991) measured quartz solubility in seawater at temperatures of 200, 300, 363, 400, and 450 °C and pressures from 200 to 1000 bar performing the experiments in the modified Dickson apparatus of Seyfried et al. (1979). The 100 data thus obtained were merged with three data for 0.5 M NaCl (Hemley et al. 1980) and 391 for pure water from distinct sources (Kennedy 1950; Morey and Hesselgesser 1951b; Wyart and Sabatier 1955; Khitarov 1956; Kitahara 1960; Van Lier et al. 1960; Morey et al. 1962; Siever 1962; Weill and Fyfe 1964; Anderson and Burnham 1965; Heitmann 1965; Sommerfeld 1967; Semonova and Tsilkis 1970; Crerar and Anderson 1971; Ragnarsdottir and Walther 1983; Walther and Orville 1983). The whole dataset includes 494 quartz solubility data covering the temperature interval 45–900 °C and the pressure range <1–9860 bar. According to Von Damm et al. (1991), quartz solubility is described by the following equation:

$$\ln m_{\mathrm{SiO_2 \cdot bH_2O}} = \mathrm{A} + \mathrm{B} \cdot \ln \rho_{\mathrm{F}} + \left(\mathrm{C} + \mathrm{D} \cdot \mathrm{T}^2\right) \cdot \mathrm{T}^{-1} + \mathrm{E} \cdot \mathrm{P} \cdot \mathrm{T}^{-1} \qquad (5.41)$$

in which ρ_F is density of the aqueous fluid in g cm^{-3}, P is pressure in bar, T is temperature in K, and coefficients are as follows: A = −2.32888, B = 1.79547, C = −2263.62, D = 0.00407350, and E = 0.0398808. In spite of the empirical derivation of Eq. (5.41), its terms are present in theoretical models describing quartz solubility. For instance: the coefficient A depends on the hydration number of dissolved silica, the weight fraction of free water, the activity coefficient of dissolved silica and water, as well as the effects of pressure on the activity coefficient of dissolved silica and water; the coefficient B is the hydration number of dissolved silica; the term $(C + D \cdot T^2)$ is equal to $-\Delta H/R$; the coefficient E is equal to $\Delta V/R$. Equation (5.41) may hold for ionic strengths higher than that of seawater, provided that coefficient A is suitably modified. However, Von Damm et al. (1991) did not test the model at high ionic strengths due to the lack of data.

Shibue (1996) used available experimental data to derive three empirical equations describing quartz solubility in pure water [i.e., Eq. (5.39) in previous section] as well as in $H_2O + CO_2$ and $H_2O + NaCl$ fluids. In particular, the relation for $H_2O + NaCl$ fluids was based on the experimentally measured quartz solubilities of Anderson and Burnham (1967), Novgorodov (1975), Hemley et al. (1980), and Fournier et al. (1982). For $H_2O + CO_2$ and $H_2O + NaCl$ fluids, the weight fraction of water in the solvent, F, the density of the aqueous fluid, ρ_F, and an empirical constant, Θ, were used as additional parameters. The ratio of quartz solubility in the aqueous fluid, $m_{SiO_2,F}$, to that in pure water, $m_{SiO_2,W}$, at the same P, T, was assumed to be expressed by the relation:

$$\ln\left(\frac{m_{SiO_2,F}}{m_{SiO_2,W}}\right) = \Theta \cdot \ln\left(\frac{\rho_F \cdot F}{\rho_{H_2O}}\right). \tag{5.42}$$

Densities of $H_2O + NaCl$ fluids were calculated by Shibue (1996) using the equations of Anderko and Pitzer (1993). The obtained equation describing quartz solubility in $H_2O + NaCl$ fluids is:

$$\ln m_{SiO_2,F} = A + B \cdot \ln \rho_F + C \cdot T^{-1} + D \cdot T + E \cdot P \cdot T^{-1} + \Theta \cdot \ln\left(\frac{\rho_F \cdot F}{\rho_{H_2O}}\right) \tag{5.43}$$

in which P is pressure in bar, T is temperature in K, densities are in g cm^{-3}, F is defined above, and coefficients are as follows: A = −1.51914, B = 1.99970, C = −2636.78, D = 0.00387766, E = 0.0198582, and Θ = 3.24740. The equation of Shibue (1996) for $H_2O + NaCl$ fluids differs from that of Von Damm et al. (1991) for the presence of an additional term, namely the last term on the right in Eq. (5.43), which is defined by Eq. (5.42) and does not appear in Eq. (5.41). Equation (5.43) applies to $H_2O + NaCl$ fluids with NaCl concentrations up to 33.6 wt%, at pressures from 0.2 to 2 kbar and temperatures from 200 to 700 °C.

To calculate the molality of aqueous SiO_2 in water-salt-CO_2 fluids in equilibrium with quartz, Akinfiev and Diamond (2009) proposed the following relation:

$$\log \mathrm{m}_{\mathrm{SiO_2}} = \mathrm{A(T)} + \mathrm{B(T)} \cdot \log \frac{18.0152}{\mathrm{V}^*_{\mathrm{H_2O}}} + 2 \cdot \log x_{\mathrm{H_2O}} \tag{5.44}$$

in which A(T) and B(T) are the two polynomials of the equation of Manning (1994), i.e., Eq. (5.38), and $x_{\mathrm{H_2O}}$ and $\mathrm{V}^*_{\mathrm{H_2O}}$ are the mole fraction and the effective partial molar volume of H_2O in the fluid, respectively. In turn, $\mathrm{V}^*_{\mathrm{H_2O}}$ is calculated from the equation:

$$\mathrm{V}_{\mathrm{mix}} = x_{\mathrm{H_2O}} \cdot \mathrm{V}^*_{\mathrm{H_2O}} + \sum x_{\mathrm{s}} \cdot \mathrm{V}_{\mathrm{s}} \tag{5.45}$$

where $\mathrm{V}_{\mathrm{mix}}$ is the molar volume of the fluid mixture (in $\mathrm{cm^3\ mol^{-1}}$) and x_{s} and V_{s} are the mole fraction and the intrinsic volume of the s solute, respectively. For the binary system H_2O–NaCl, Eq. (5.45) simplifies as follows:

$$\mathrm{V}_{\mathrm{mix}} = x_{\mathrm{H_2O}} \cdot \mathrm{V}^*_{\mathrm{H_2O}} + (1 - x_{\mathrm{H_2O}}) \cdot \mathrm{V}_{\mathrm{NaCl}} \tag{5.46}$$

with the intrinsic volume of NaCl equal to $30.8 \pm 1.3\ \mathrm{cm^3\ mol^{-1}}$. For pure water, the relation of Akinfiev and Diamond (2009), i.e., Eqn (5.44), becomes equal to that of Manning (1994) i.e., Eq. (5.38). The density model of Akinfiev and Diamond (2009) has been coded by Ronald Bakker into the program package LonerAP (Bakker 2003), which may be downloaded, free of charge, at the website: http://fluids.unileoben.ac.at/Computer.html.

We used the equations of Von Damm et al. (1991) and Akinfiev and Diamond (2009) to calculate quartz solubility in liquid seawater, at saturation temperatures and pressures, considering the molar volumes and densities of seawater from Bischoff and Rosenbauer (1985)[4]. Results are shown in Fig. 5.6, together with quartz solubility in pure water, at saturation temperatures and pressures, which was computed by means of the equations of Von Damm et al. (1991) and Manning (1994).

The two seawater curves mimic the corresponding pure water curves, apart from the flat portion close to the critical temperature of seawater, 408 °C (Bischoff 1991), which might be due to uncertainties in relevant data. Moreover, the two seawater curves depart progressively from the corresponding pure water curves, indicating that quartz becomes more and more soluble in seawater, compared to pure water, with increasing temperature. Some details are given below.

For instance, at 200 °C, quartz solubility increases by 6.4 mg/kg, from 259.3 mg/kg in pure water to 265.7 mg/kg in seawater, according to Von Damm et al. (1991), and by 5.4 mg/kg, from 237.7 mg/kg in pure water to 243.1 mg/kg in seawater, according to Akinfiev and Diamond (2009).

At 250 °C, quartz solubility growths by 24.1 mg/kg, from 436.4 mg/kg in pure water to 460.5 mg/kg in seawater, according to Von Damm et al. (1991), and by 23.0 mg/kg, from 404.8 mg/kg in pure water to 427.8 mg/kg in seawater, according to Akinfiev and Diamond (2009).

---

[4] The equation of Shibue (1996) was not used because it cannot be applied along the saturation curve of seawater.

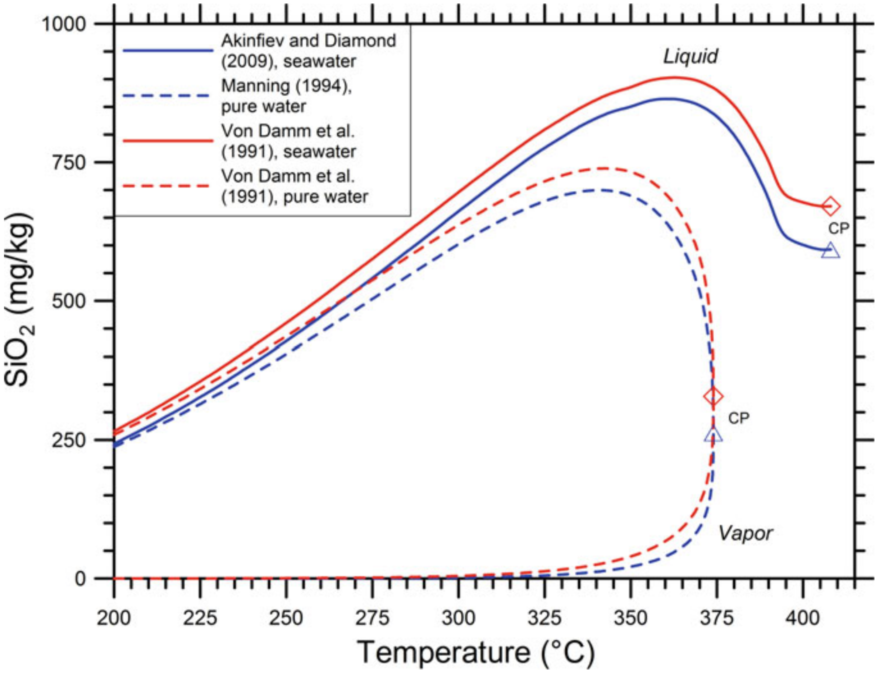

Fig. 5.6 Quartz solubility in liquid seawater, at saturation temperatures and pressures, computed by means of the equations of Von Damm et al. (1991) and Akinfiev and Diamond (2009), as a function of temperature. Quartz solubility in pure water, at saturation temperatures and pressures, computed by means of the equations of Von Damm et al. (1991) and Manning (1994) is also shown for comparison. The blue triangles and the red diamonds indicate the SiO_2 concentration at critical point (C.P.)

At 300 °C, quartz solubility increments by 59.3 mg/kg, from 636.7 mg/kg in pure water to 696.0 mg/kg in seawater, according to Von Damm et al. (1991), and by 59.4 mg/kg, from 602.0 mg/kg in pure water to 661.4 mg/kg in seawater, according to Akinfiev and Diamond (2009).

At 350 °C, quartz solubility increases by 153.0 mg/kg, from 732.6 mg/kg in pure water to 885.6 mg/kg in seawater, according to Von Damm et al. (1991), and by 160.8 mg/kg, from 689.7 mg/kg in pure water to 850.5 mg/kg in seawater, according to Akinfiev and Diamond (2009).

At 370 °C quartz solubility growths by 317.8 mg/kg, from 578.2 mg/kg in pure water to 896.0 mg/kg in seawater, according to Von Damm et al. (1991), and by 337.1 mg/kg, from 515.7 mg/kg in pure water to 852.8 mg/kg, according to Akinfiev and Diamond (2009).

Therefore, the increase in quartz solubility in seawater with respect to pure water is relatively similar in both cases, that is considering either the two curves of Von Damm et al. (1991) or the curves of Akinfiev and Diamond (2009) and Manning (1994), whereas the differences between the two seawater curves reflect essentially the differences between the two pure water curves, which are computed according to Von Damm et al. (1991) and Manning (1994), respectively.

5.2.4 The Preferred Silica Geothermometers

It is useful to compare the increase in quartz solubility in seawater with respect to pure water (see previous section) with the difference in solubility between quartz/chalcedony [polynomial Eq. (4.57), see Sect. 4.10.2] and quartz computed by means of the program SUPCRT92 (Johnson et al. 1992), using the thermodynamic data of quartz from Helgeson et al. (1978) and those of aqueous SiO_2 from Shock et al. (1989). All solubilities are at saturation temperatures and pressures.

At 200 °C, the difference in solubility between quartz/chalcedony and quartz, 47.7 mg/kg, is 7.5–8.8 times higher than the increase in quartz solubility in seawater with respect to pure water, 5.4–6.4 mg/kg.

At 250 °C, the difference in solubility between quartz/chalcedony and quartz, 72.8 mg/kg, is 3.0–3.2 times higher than the increase in quartz solubility in seawater with respect to pure water, 23.0–24.1 mg/kg.

At 300 °C, the difference in solubility between quartz/chalcedony and quartz, 101.6 mg/kg, is 1.7 times higher than the increase in quartz solubility in seawater with respect to pure water, 59.3–59.4 mg/kg.

At 350 °C, the situation inverts and the increase in quartz solubility in seawater with respect to pure water, 153.0–160.8 mg/kg becomes 1.3 times higher than the difference in solubility between quartz/chalcedony and quartz, 120.3 mg/kg.

Summing up, only at temperatures higher than 300 °C, the increment in quartz solubility caused by NaCl addition to pure water (~3.2 wt% corresponding to ~0.55 mol/kg) is more important than the increase in solubility due to the larger grain size of quartz crystal. Among the reservoir liquids considered in this work, the NaCl effect on quartz solubility is significant only for the high-salinity, high-temperature liquids of Salton Sea (with Cl concentrations in the range 116,000–162,000 mg/kg in most cases) and to, a lower degree, of Asal (with Cl concentrations of 66,800 to 74,600 mg/kg).

For these reasons, solubility of quartz/chalcedony was generally adopted, in this work, as preferred silica geothermometer for the neutral liquids of salinity significantly lower than the seawater value and temperature in the range 180–350 °C. Following Arnórsson et al. (1983a), the solubility of chalcedony was instead adopted for the same kind of liquids below 180 °C.

5.2.5 The Silica Versus Enthalpy Plot

As underscored by Fournier (1991), in data processing/interpretation, it is often advisable to use the diagram of silica versus enthalpy instead of the plot of silica versus temperature, because enthalpy can be involved in enthalpy balances (whereas this is not possible for temperature) and for other reasons given below. Therefore, the quartz solubility curve for pure water according to Fournier and Potter (1982a) was reported in the silica versus enthalpy plot of Fig. 5.7 by combining the silica concentrations given by Eq. (5.36), at saturation temperatures and pressures, with the enthalpies of pure water from the Steam Tables (Lemmon et al. 2017; see above) at the same conditions.

Besides, the curve expressing the solubility of quartz/chalcedony in pure liquid water [polynomial Eq. (4.57), see Sect. 4.10.2], again at saturation temperatures and pressures, was added to the diagram. As temperature increases above 313 °C, the quartz/chalcedony curve deviates more and more from the Fournier and Potter curve. In contrast, below 313 °C, the two curves are relatively close to each other, with differences in SiO_2 concentration lower than 20 mg/kg and average absolute deviation of 13 mg/kg.

In the silica versus enthalpy plot, the solubility of quartz in pure water (liquid and steam), at saturation temperatures and pressures, according to Fournier and

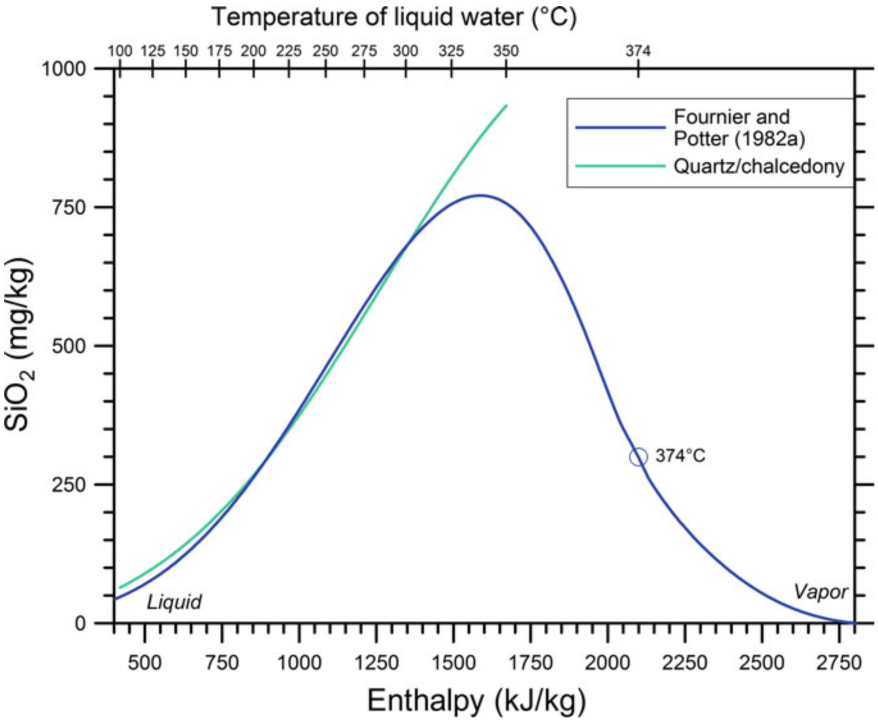

Fig. 5.7 Solubility of quartz in pure liquid water and in steam, at saturation temperatures and pressures, as a function of enthalpy (from Fournier and Potter 1982a). The blue circle indicates the SiO_2 concentration at critical point (C.P.). The solubility of quartz/chalcedony in pure liquid water, at saturation temperatures and pressures, is also shown

Potter (1982a), is represented by a bell-shaped symmetrical curve, which reaches its maximum of 771.2 mg/kg at 1587.4 kJ/kg, corresponding to 339 °C, and decreases with a further increase in enthalpy. Therefore, at a given enthalpy, there is only one value of dissolved silica, while at a given temperature there are two values of dissolved silica, one for the liquid phase and one for the steam phase (see Fig. 5.4). This is another good reason for using the diagram of silica versus enthalpy (Fig. 5.7) instead of the plot of silica versus temperature (Fig. 5.4).

Two possible quartz solubility curves in seawater, computed by means of the equations of Von Damm et al. (1991) and Akinfiev and Diamond (2009), and the related quartz solubility curves in pure water, computed using the functions of Von Damm et al. (1991) and Manning (1994), are shown in the silica versus enthalpy plot of Fig. 5.8.

Also the solubility of quartz in seawater is described by bell-shaped curves similar to that of pure water, apart from the flat part close to the critical temperature of

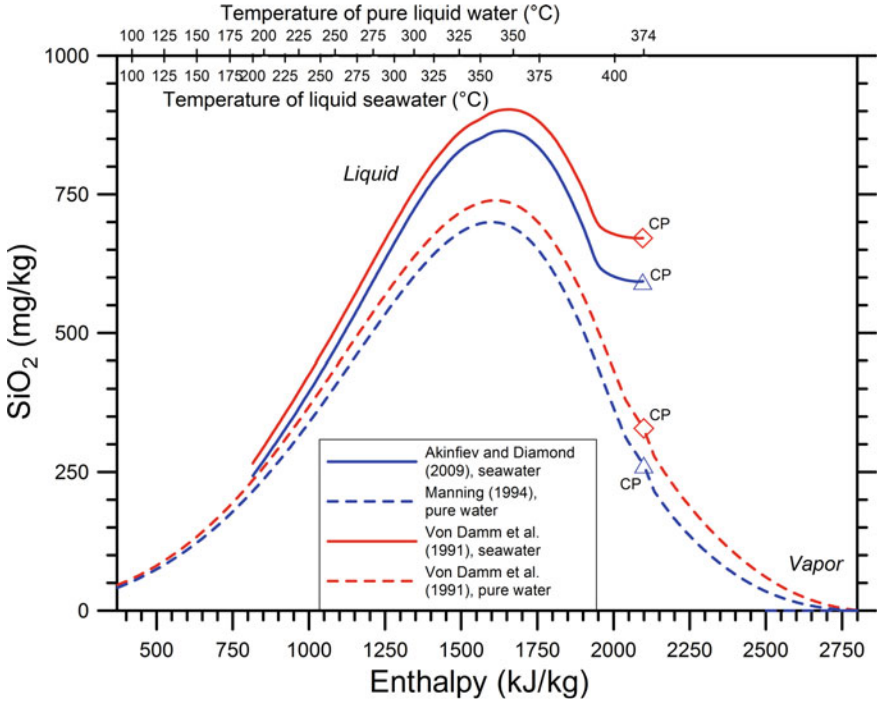

Fig. 5.8 Quartz solubility in liquid seawater, at saturation temperatures and pressures, computed using the equations of Von Damm et al. (1991) and Akinfiev and Diamond (2009), as a function of enthalpy. Quartz solubility in pure water, at saturation temperatures and pressures, calculated by means of the equations of Von Damm et al. (1991) and Manning (1994) is also shown for comparison. The blue triangles and the red diamonds indicate the SiO_2 concentration at critical point (C.P.)

seawater, 408 °C (Bischoff 1991), which might be due to uncertainties in pertinent data. As expected, the two seawater curves are situated above the two pure water curves because quartz solubility increases with increasing salt concentration, as already discussed in Sect. 5.2.3.

Quartz solubility curves in seawater can be of interest for high-salinity geothermal liquids. In most cases, however, the quartz solubility curve in pure water represents a suitable approximation and the basis for different geothermometric techniques, such as the silica mixing model (Truesdell and Fournier 1977), the silica boiling model (Fournier 1991), and the quartz geothermometry for wells with excess enthalpy (excess steam) discharges. These topics are treated in the next sections.

5.2.6 The Silica Mixing Model

Assuming conservation of enthalpy and conservative behavior for dissolved SiO_2, that is adopting the silica mixing model of Truesdell and Fournier (1977), the silica versus enthalpy plot reporting the quartz/chalcedony solubility curve for pure water can be used to determine the temperature of the thermal endmember involved in mixed water(s). In the ideal case, in which the cold endmember is known and the mixture is unaffected either by conductive heat losses or gain/loss of dissolved SiO_2, the intersection of the straight line drawn through the cold endmember and the mixed water with the quartz/chalcedony solubility curve gives the initial silica content and the enthalpy of the thermal endmember (Fig. 5.9 a).

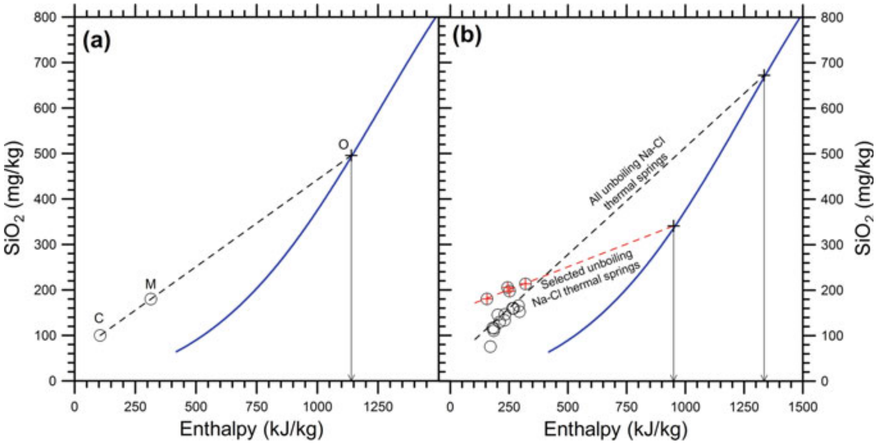

Fig. 5.9 Enthalpy-silica plot illustrating the application of the silica mixing model (Truesdell and Fournier 1977) to both **a** the ideal case in which the cold endmember C is known and the mixture M is unaffected either by conductive heat losses or gain/loss of dissolved SiO_2 and **b** the Na–Cl unboiling thermal springs of San Marcos, Guatemala (data from Marini et al. 1998)

This graphical exercise corresponds to solve a system constituted by the silica-enthalpy relation equivalent to the polynomial Eq. (4.57), see Sect. 4.10.2:

$$\begin{aligned} c_{SiO_2,O} = & -20.195 + 0.21658 \cdot Ho - 2.9378 \times 10^{-4} \cdot H_0^2 \\ & + 7.2745 \times 10^{-7} \cdot Ho^3 - 2.5453 \times 10^{-10} \cdot Ho^4 \end{aligned} \tag{5.47}$$

the enthalpy balance:

$$H_M = H_C \cdot (1 - x) + H_O \cdot x \tag{5.48}$$

and the mass balance:

$$c_{SiO_2,M} = c_{SiO_2,C} \cdot (1 - x) + c_{SiO_2,O} \cdot x. \tag{5.49}$$

In Eqs. (5.47)–(5.49), pedices O, C, and M refer to the reservoir water (i.e., the thermal endmember), the shallow water (i.e., the cold endmember), and the mixture, respectively, whereas x is the mass fraction of the thermal endmember in the mixture.

In real situations, mixed waters are more or less scattered due to conductive cooling and loss or (less likely) gain of dissolved SiO_2. Reconstruction of a reasonable mixing line requires use of linear regression through the most representative samples, which are presumably not affected (or least affected) by conductive cooling and loss (or gain) of dissolved SiO_2. In fact, if the mixtures are affected by heat losses through conduction, the enthalpy of the thermal endmember is overestimated, whereas if mixed waters are influenced by SiO_2 losses, the enthalpy of the thermal endmember is underestimated.

In the case of the Na–Cl unboiling thermal springs of San Marcos, Guatemala (data from Marini et al. 1998), the linear regression equation through all the samples intersects the quartz/chalcedony solubility curve at an enthalpy of 1335 kJ/kg, corresponding to a temperature of 298 °C (Fig. 5.9b). This temperature is too high for the thermal endmember, based on the results of other geothermometric techniques (Marini et al. 1998 and references therein). In contrast, the line drawn through the four springs less affected by SiO_2 loss (identified by the red crosses) leads to an estimated enthalpy of 950 kJ/kg for the thermal endmember. This enthalpy value corresponds to a temperature close to 220 °C, which is within the range indicated by the silica boiling model for the boiling springs present in the area (see next section).

5.2.7 *The Silica Boiling Model*

The silica versus enthalpy plot with the quartz/chalcedony solubility curve for pure water allows also a quick determination of the silica concentration and enthalpy of the initial liquid before boiling assuming (i) equilibrium between quartz/chalcedony and the aqueous solution under reservoir conditions, (ii) conservation of enthalpy during the travel of the liquid phase from the reservoir to the surface discharge point, which is a realistic assumption for the irreversible adiabatic process taking place in geothermal wells and high-flow rate natural geothermal manifestations, and (iii) occurrence of single-step vapor/liquid separation at surface conditions, i.e., 100 °C, 1.013 bar at sea level. Under these assumptions, the enthalpy and silica concentration of the initial liquid before boiling are given by the intersection of the line joining the boiled liquids and the steam point at 100 °C, 1.013 bar (code V) with the quartz/chalcedony solubility curve, as shown by the silica versus enthalpy plot for the boiling springs of San Marcos, Guatemala (Fig. 5.10).

This graphical exercise corresponds to solve a system constituted by the silica-enthalpy relation (5.47), the enthalpy balance:

$$H_O = H_L \cdot (1 - y) + H_V \cdot y, \tag{5.50}$$

and the mass balance:

$$c_{SiO_2,O} = c_{SiO_2,L} \cdot (1 - y) + c_{SiO_2,V} \cdot y, \tag{5.51}$$

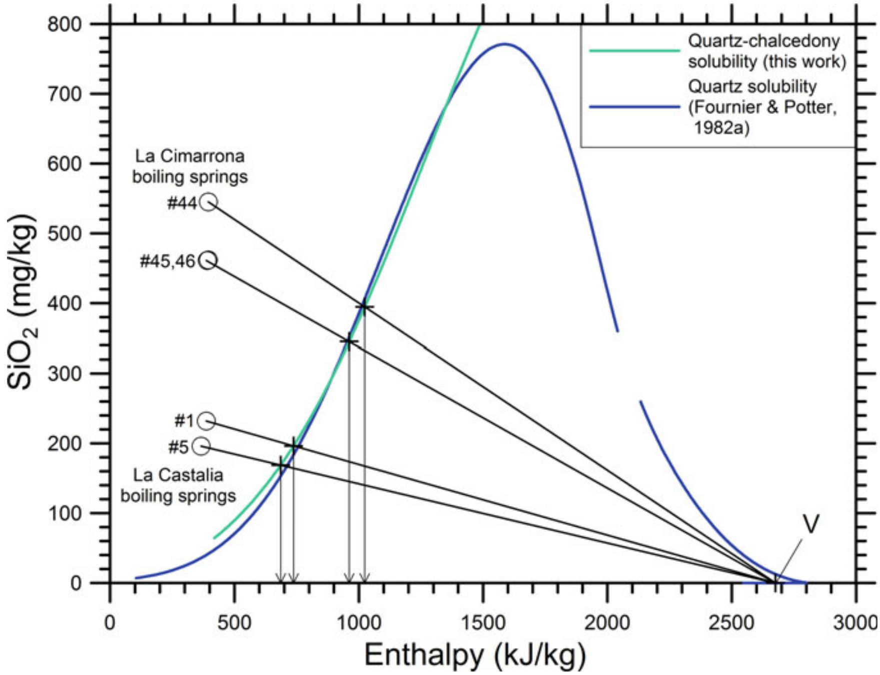

Fig. 5.10 Plot of silica versus enthalpy for the boiling springs of La Cimarrona and La Castalia, San Marcos area, Guatemala (circles, data from Marini et al., 1998), also showing both quartz solubility in pure water (from Fournier and Potter 1982a) and quartz/chalcedony solubility in pure water (this work), at saturation temperatures and pressures (see legend; modified from Fournier 1991)

where subscripts O, L, and V refer to the deep reservoir water, the separated liquid, and the separated vapor, respectively, whereas y is the mass steam fraction. At vapor/liquid separation conditions of 100 °C, 1.013 bar, $SiO_{2,V}$ can be assumed equal to zero and Eqs. (5.51) reduces to:

$$c_{SiO_2,O} = c_{SiO_2,L} \cdot (1 - y). \tag{5.52}$$

At these separation conditions, $H_L = 419.17$ kJ/kg and $H_V = 2675.6$ kJ/kg.

For La Cimarrona springs (# 44, 45, and 46) with $c_{SiO_2,L}$ of 461–545 mg/kg, H_O and $c_{SiO_2,O}$ turn out to be 961.1–1023.9 kJ/kg and 345.3–394.7 mg/kg, respectively, corresponding to quartz/chalcedony equilibrium temperatures of 224–237 °C. For La Castalia springs # 1 and #5, with $c_{SiO_2,L}$ of 232 and 196 mg/kg, the obtained H_O values are 737.8 and 686.4 kJ/kg and the resulting $c_{SiO_2,O}$ values are 196.4 and 168.8 mg/kg, corresponding to quartz/chalcedony equilibrium temperatures of 163 and 174 °C, respectively. These temperature values are moderately smaller than those proposed by Marini et al. (1998), i.e., 240 °C for La Cimarrona and 185 °C for La Castalia.

5.2.8 *Silica Geothermometry for Wells with Excess Enthalpy (Excess Steam) Discharges*

The excess enthalpy (excess steam) discharge is generally caused by the entry of excess steam into these wells, together with the reservoir liquid phase, although other models are possible as discussed by Arnórsson et al. (2007), see also Sect. 3.1.2. Since the excess steam dilutes the liquid, concentrations on a total-discharge basis decrease for non-volatile solutes and increase for gas species.

In many liquid-dominated systems, the excess steam comes from the vapor cap which is typically situated on top of the aquifer hosting the single liquid phase. Examples are Wairakei in New Zealand, Svartsengi in Iceland, and Olkaria in Kenya. In some systems, the steam cap is present in the natural state before the onset of exploitation, whereas in other systems, the steam cap develops due to pressure drawdown caused by the exploitation. The vapor cap is generally characterized by pressures and temperatures close to those of maximum enthalpy for saturated steam, 236 °C, 31.2 bar [5] (e.g., Ingebritsen and Sorey 1988; Arnórsson et al. 2007). Therefore, in the following discussion, the reservoir vapor is assumed to be at these P, T conditions and to have enthalpy of 2803.2 kJ/kg. Of course, the enthalpy of the reservoir vapor can be properly fixed if different data are available.

Let us assume also that liquid samples are collected from the weir box at atmospheric pressure. If so, the enthalpy of the separated steam is 2675.6 kJ/kg. Although the difference between these two enthalpies is less than 5%, it is important to consider

---

[5] The reason for these peculiar conditions in vapor-dominated systems were discussed by James (1968) and White et al. (1971) based on the pressure-enthalpy diagram for pure water.

the proper enthalpy values to minimize uncertainties on the quartz/chalcedony temperature of the reservoir fluid, which is hypothesized to be a pure saturated liquid phase.

The quartz/chalcedony geothermometric method is graphically presented in Fig. 5.11 for the sample collected from the Olkaria well OW-709 with discharge enthalpy of 1921 kJ/kg and SiO_2 concentration at the weir box of 649 mg/kg (Karingithi et al. 2010).

First, we plot the weir box sample on the silica versus enthalpy diagram associating the SiO_2 concentration to the enthalpy of the separated liquid phase, 419.17 kJ/kg (black triangle).

Second, we draw the black solid line connecting the separated liquid point and the separated steam point, with enthalpy of 2675.6 kJ/kg and SiO_2 concentration of 0 mg/kg (black square).

Third, we place the point representative of total discharge along this black solid line at enthalpy of 1921 kJ/kg, resulting in a SiO_2 concentration of 217.0 mg/kg (green circle).

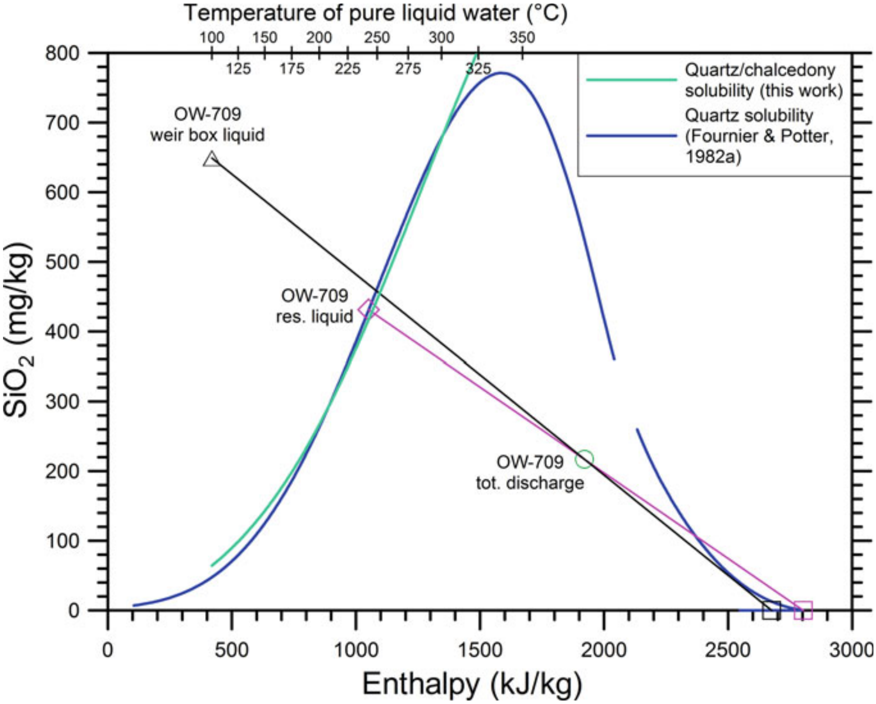

Fig. 5.11 Plot of silica versus enthalpy for the sample collected from the Olkaria well OW-709 (data from Karingithi et al. 2010), also showing both quartz solubility in pure water (from Fournier and Potter 1982a) and quartz/chalcedony solubility in pure water (this work), at saturation temperatures and pressures (see legend). The black square refers to the steam separated at atmospheric conditions. The pink square represents reservoir steam. See text for other explanations and discussion

Fourth, we draw the pink solid line from the reservoir steam point, with enthalpy of 2803.2 kJ/kg and SiO_2 concentration of 0 mg/kg (pink square) through the total discharge point (green circle). The intersection of this line and the quartz/chalcedony solubility curve (pink diamond) constrains the reservoir liquid enthalpy at 1064.18 kJ/kg and its silica concentration at 427.8 mg/kg, corresponding to a reservoir temperature of 245.5 °C. The mass fraction of reservoir vapor results to be 0.493.

Instead of this graphical exercise, we can first compute the SiO_2 concentration in total discharge, $c_{SiO_2,TD}$, using the following relation:

$$c_{SiO_2,TD} = c_{SiO_2,WB} \cdot (1 - y) \tag{5.53}$$

where $c_{SiO_2,WB}$ is the silica concentration in the separated liquid at the weir box and y is the mass steam fraction at the same atmospheric P,T conditions, which is calculated from total discharge enthalpy, H_{TD}:

$$y = \frac{H_{TD} - H_{L,WB}}{H_{V,WB} - H_{L,WB}}, \tag{5.54}$$

where indices L,WB and V,WB refer to the separated liquid at the weir box and the separated vapor at the weir box, respectively.

Second, we solve the system constituted by the silica-enthalpy relation (5.47), the silica mass balance:

$$c_{SiO_2,TD} = c_{SiO_2,RL} \cdot (1 - x) + c_{SiO_2,RV} \cdot x \tag{5.55}$$

and the enthalpy balance:

$$H_{TD} = H_{RL} \cdot (1 - x) + H_{RV} \cdot x \tag{5.56}$$

where subscripts RL and RV refer to the reservoir liquid and the reservoir vapor, respectively, and x stands for the mass fraction of reservoir vapor.

Table 5.1 lists the main results, including the mass fraction of reservoir vapor and the quartz/chalcedony temperature of the reservoir liquid, for all the Olkaria wells sampled by Karingithi et al. (2010), together with the input data used both in calculations and to prepare the silica versus enthalpy plot of Fig. 5.12.

Twenty five of the thirty samples have fraction of reservoir vapor varying from 0.1 and 0.9, whereas the remaining four samples have fraction of reservoir vapor varying between 0.095 and 0.001. Only ten samples have quartz/chalcedony temperatures, $T_{Qz/Chc}$, comparable with reported aquifer temperatures, T_R, within ± 5 °C. Thirteen samples have absolute differences between $T_{Qz/Chc}$ and T_R varying from 6 to 15 °C. Seven samples have even higher absolute differences between $T_{Qz/Chc}$ and T_R, ranging from 18 to 60 °C. Most of these differences are probably related to the definition of the aquifer temperature, which was computed by Karingithi et al. (2010) by taking the average of the temperatures given by the quartz and Na–K geothermometers.

Table 5.1 Results of the quartz/chalcedony geothermometer for the Olkaria wells sampled by Karingithi et al. (2010), most of which have high mass fractions of reservoir vapor, x. T_R is the reservoir temperature reported by the authors in their Table 4

Well	H_{TD}	$c_{SiO_2,WB}$	$y_{,WB}$	$c_{SiO_2,TD}$	H_{RL}	$c_{SiO_2,RL}$	x	$T_{Qz/Chc}$	T_R
	kJ/kg	mg/kg		mg/kg	kJ/kg	mg/kg		°C	°C
OW-02	1839	643	0.629	238.4	1066.15	429.5	0.445	245.9	251
OW-05	2599	624	0.966	21.2	764.10	211.5	0.900	180.4	240
OW-10	2531	773	0.936	49.5	950.50	337.2	0.853	221.4	262
OW-11	1894	597	0.654	206.8	1033.51	402.5	0.486	239.1	246
OW-15	2140	576	0.763	136.7	996.20	372.5	0.633	231.2	242
OW-16	1534	502	0.494	254.0	985.13	363.8	0.302	228.8	228
OW-19	1871	548	0.643	195.4	1002.45	377.5	0.482	232.5	229
OW-20	2541	778	0.940	46.4	940.50	329.7	0.859	219.3	254
OW-26	1881	657	0.648	231.4	1071.94	434.3	0.467	247.1	247
OW-28	2446	625	0.898	63.6	942.65	331.3	0.808	219.8	239
OW-29	2158	609	0.771	139.7	1014.68	387.2	0.639	235.1	243
OW-30i	2196	768	0.787	163.2	1099.77	458.0	0.644	252.8	262
OW-30ii	2196	701	0.787	149.0	1063.15	427.0	0.651	245.3	259
OW-10	2535	638	0.938	39.8	878.90	285.2	0.861	206.0	242
OW-15	1899	604	0.656	207.9	1037.67	405.9	0.488	239.9	246
OW-16	1384	573	0.428	328.0	1039.69	407.6	0.195	240.4	237
OW-19	1823	622	0.622	235.0	1054.04	419.4	0.440	243.4	253
OW-23	2191	653	0.785	140.2	1036.27	404.8	0.654	239.6	242
OW-25	2516	641	0.929	45.3	900.45	300.4	0.849	210.7	253
OW-202	1104	320	0.304	222.9	838.26	257.7	0.135	197.0	193
OW-301	1653	855	0.547	387.5	1195.28	541.7	0.285	272.0	262
OW-302	1234	744	0.361	475.3	1149.36	501.0	0.051	262.9	256
OW-304D	1672	364	0.555	161.9	867.10	277.1	0.416	203.4	190
OW-306	1037	551	0.274	400.1	1032.00	401.3	0.003	238.7	224
OW-709	1921	649	0.666	217.0	1064.18	427.8	0.493	245.5	245
OW-714	1303	739	0.392	449.5	1144.78	497.0	0.095	262.0	267
OW-719	1259	588	0.372	369.1	1052.87	418.4	0.118	243.1	241
OW-901	1854	529	0.636	192.6	990.32	367.9	0.476	229.9	220
OW-902	1108	477	0.305	331.4	976.50	357.1	0.072	227.0	209
OW-903	953	443	0.237	338.2	952.07	338.4	0.001	221.8	207

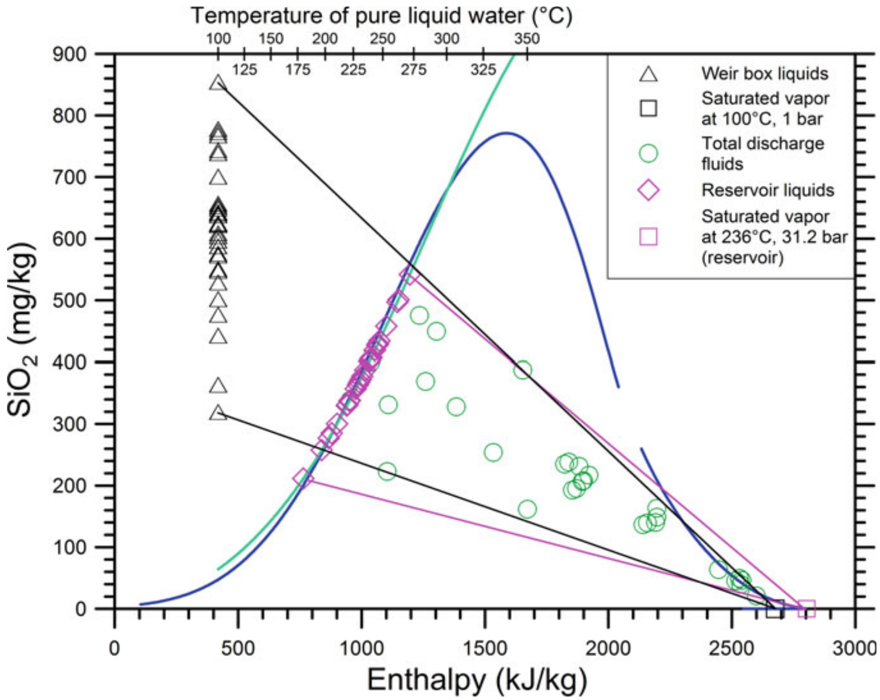

Fig. 5.12 Plot of silica versus enthalpy for all the samples collected from the Olkaria wells by Karingithi et al. (2010), also showing both quartz solubility in pure water (from Fournier and Potter 1982b; blue curves) and quartz/chalcedony solubility in pure water (this work; aquamarine curve), at saturation temperatures and pressures. The two solid black lines enclose the separated liquids collected at the weir box, whereas the two solid pink lines encompass the reservoir liquids. See text for other explanations and discussion

Finally, it must be underscored that the silica-enthalpy diagram and related calculations can be applied not only to wells with excess enthalpy discharges but also to wells discharging bi-phase fluids produced through boiling of single-phase reservoir liquids either unaffected by steam gain/loss or affected by steam loss. The well discharges unaffected by steam gain/loss are situated along the quartz/chalcedony solubility curve in the silica-enthalpy diagram, whereas the well discharges affected by steam loss, similar to the boiling springs, are positioned to the left of the quartz/chalcedony solubility curve having negative x values.

5.2.9 Relation Between Undissociated SiO_2 and Aquifer Temperature for the Selected Reservoir Liquids

The concentration of undissociated silica, $SiO_{2(aq)}$, of the 1013 selected reservoir liquids is contrasted with the aquifer temperature (or reservoir temperature or reference temperature) in the correlation diagrams of Fig. 5.13. The solubility of quartz/chalcedony (see Sect. 4.10.2), at saturation temperatures and pressures, is also shown in these diagrams, together with the solubilities of quartz and chalcedony, at saturation temperatures and pressures, constrained by the thermodynamic data of quartz and chalcedony from Helgeson et al. (1978) and of aqueous SiO_2 from Shock et al. (1989).

Most reservoir liquids are positioned along the solubility curves of quartz/chalcedony or chalcedony because their aquifer temperatures were assumed to be equal to either the quartz/chalcedony temperature given by Eq. (4.57) above 180 °C or the chalcedony temperature given by Eq. (5.18) at lower temperatures. This assumption was generally adopted owing to the lack of information on aquifer temperatures.

A number of reservoir liquids are positioned between the solubility curves of quartz and chalcedony, due to attainment of equilibrium with quartz crystals of different grain size, as suggested by Azaroual et al. (1997) for the geothermal fluids of the Paris Basin. Some samples are found slightly above (to the left of) the chalcedony solubility curve due to moderate supersaturation with this silica mineral or underestimation of the aquifer temperature.

All the reservoir liquids from Salton Sea and some from other fields, namely five from Los Azufres and three from Cerro Prieto (Fig. 5.13b), one from Fushime (Fig. 5.13c), four from Rotokawa (Fig. 5.13e), and two from Mofete (Fig. 5.13f) are located significantly below (to the right of) the solubility curve of quartz. These shifts are ascribable to either overestimation of the reference temperature or, more likely, loss of SiO_2 through precipitation of amorphous silica.

All previous findings are not surprising recalling that the rate of quartz dissolution/precipitation depends strongly on temperature and is comparatively fast at high temperatures and very slow at low temperatures (e.g., Marini 2006 and references therein). This explains why: (i) in the geothermal aquifers of medium to high temperature (generally > 180 °C), reservoirs liquids attain equilibrium with respect to quartz or quartz/chalcedony, after relatively long water-rock interaction processes and (ii) precipitation of quartz or quartz/chalcedony does not occur during the relatively fast upflow of the reservoir liquids, even though saturation with respect to these solid phases is largely exceeded.

In contrast, amorphous silica precipitates relatively fast when saturation is exceeded, thus representing an upper threshold on the silica concentrations attainable in many natural aqueous environments.

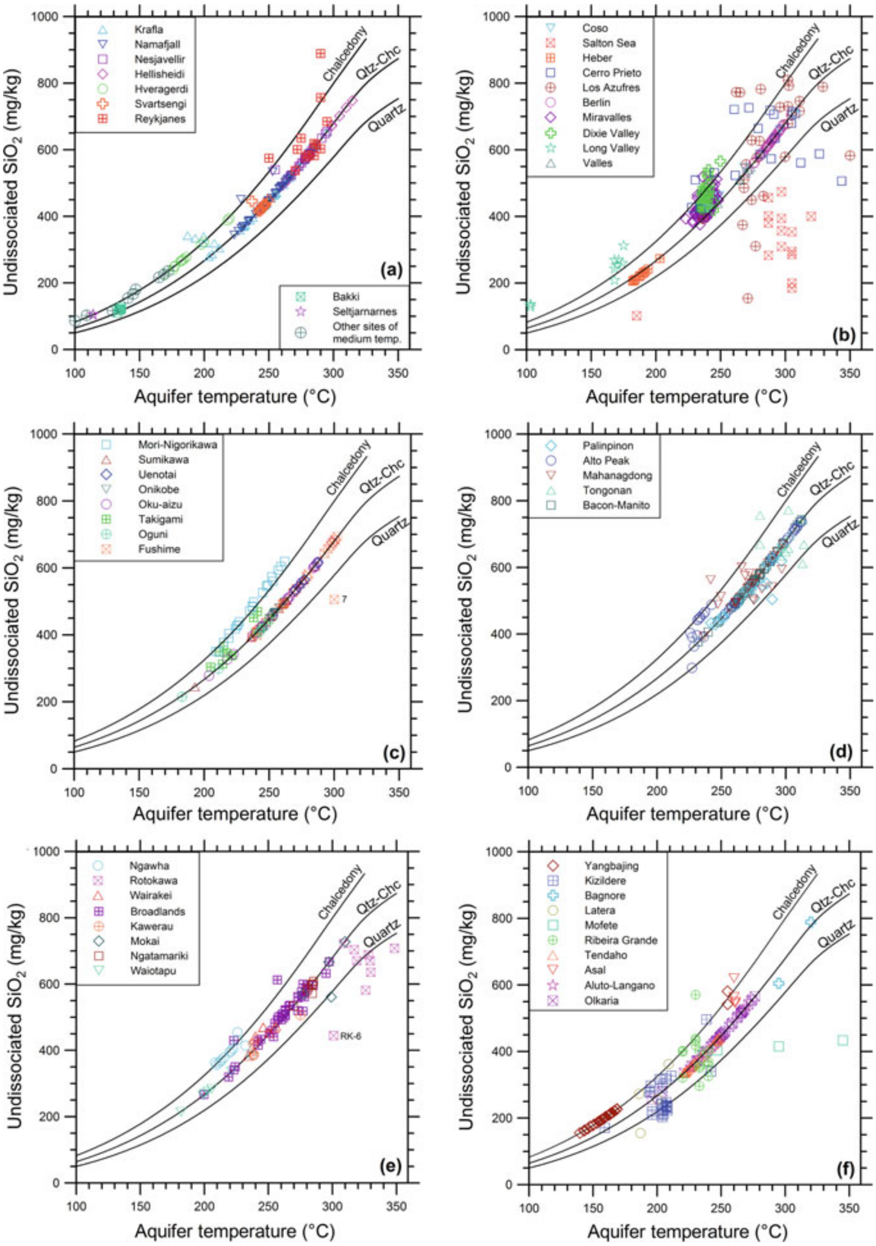

Fig. 5.13 Correlation diagrams of undissociated silica versus aquifer temperature for the selected reservoir liquids from **a** Iceland, **b** Northern-Central America, **c** Japan, **d** The Philippines, **e** New Zealand, and **f** miscellaneous geothermal systems. The solubility of quartz/chalcedony, at saturation temperatures and pressures, computed using the polynomial Eq. (4.57), is also shown in these plots, together with the solubilities of quartz and chalcedony, at saturation temperatures and pressures, constrained by the thermodynamic data of quartz and chalcedony from Helgeson et al. (1978) and of aqueous SiO_2 from Shock et al. (1989)

5.3 The Na–K Geothermometers

There are more than a few Na–K geothermometers in the literature as detailed in the next sections. These geothermometric equations were used in a large number of studies since the ‘60s and are still extensively used today. One of the main advantages of the Na–K geothermometers is that they are not affected by steam separation and are weakly influenced by mixing, provided that the Na and K concentrations of the diluting water are much lower than those of the liquid coming from the geothermal reservoir (e.g., Fournier 1981). According to several authors, the Na–K geothermometer is likely to re-adjust slower than the silica and K–Mg geothermometers in response to physical changes experienced by thermal waters and, therefore, deep Na/K-ratios are preserved upon cooling (see below for further details). We will show that alternative views on the behavior of Na–K geothermometers are possible.

5.3.1 The Na–K Geothermometric Functions Proposed by Different Authors

After the pioneering studies of White (1965, 1968), Ellis and Mahon (1967), Ellis (1970), and Mercado (1970), several geothermometric relations involving the Na/K ratio were proposed by different authors (e.g., Fournier and Truesdell 1973; Truesdell 1976; Fournier 1979; Tonani 1980; Arnórsson et al. 1983a; Giggenbach et al. 1983; Nieva and Nieva 1987; Giggenbach 1988; Kharaka and Mariner 1989; Michard 1990; Verma and Santoyo 1997; Santoyo and Díaz-González 2010; Simmons 2013).

Since the mid ‘70s, the van’t Hoff equation integrated for constant standard enthalpy of reaction (see Sect. 5.1.3) was adopted as a common practice to express the Na–K geothermometers. This is an acceptable approximation because the Na–K geothermometers are controlled by ion-exchange isocoulombic reactions, irrespective of the involved minerals. Therefore, the $\Delta C_P°_r$ is close to zero and the $\Delta H°_r$ is constant or nearly so (see Sect. 5.1.3).

As already recalled in Sect. 5.1.2, tables and diagrams showing the atomic Na/K ratios and temperatures were presented in the early studies, performed before the mid ’70s. Therefore, we have transposed these tables and diagrams in the corresponding analytical forms, obtaining Na–K relations linear with respect to the absolute temperature inverse, which are directly comparable with the more recent Na–K functions.

All the Na–K geothermometers mentioned so far are reported in Table 5.2, in which two expressions are given for convenience of the reader, one including the molal concentrations of Na and K, the other comprising the concentrations of the two alkali metals in mg/kg, although the change from one formulation to the other is straightforward. All these Na–K geothermometric functions were calibrated on a purely empirical basis, utilizing both results of laboratory experiments and water compositions of geothermal boreholes, hot springs, and fluid inclusions.

Table 5.2 Considered Na–K geothermometers with linear dependence on the absolute temperature inverse. T is temperature in °C

References	Na–K function involving molal concentrations	Na–K function involving concentrations in mg/kg	Code	Eqn. #
White (1968)	$T = \frac{504.1}{\log\left(\frac{m_{Na}}{m_K}\right) - 0.0594} - 273.15$	$T = \frac{504.1}{\log\left(\frac{c_{Na}}{c_K}\right) + 0.1712} - 273.15$	Wh68	(5.57)
Ellis (1970)	$T = \frac{801.5}{\log\left(\frac{m_{Na}}{m_K}\right) + 0.5214} - 273.15$	$T = \frac{801.5}{\log\left(\frac{c_{Na}}{c_K}\right) + 0.752} - 273.15$	El70	(5.58)
Mercado (1970)	$T = \frac{640.5}{\log\left(\frac{m_{Na}}{m_K}\right) + 0.2411} - 273.15$	$T = \frac{640.5}{\log\left(\frac{c_{Na}}{c_K}\right) + 0.4717} - 273.15$	Me70	(5.59)
Fournier and Truesdell (1973)	$T = \frac{777}{\log\left(\frac{m_{Na}}{m_K}\right) + 0.47} - 273.15$	$T = \frac{777}{\log\left(\frac{c_{Na}}{c_K}\right) + 0.70} - 273.15$	FoTr73	(5.60)
Truesdell (1976)	$T = \frac{855.6}{\log\left(\frac{m_{Na}}{m_K}\right) + 0.6267} - 273.15$	$T = \frac{855.6}{\log\left(\frac{c_{Na}}{c_K}\right) + 0.8573} - 273.15$	Tr76	(5.61)
Fournier (1979)	$T = \frac{1217}{\log\left(\frac{m_{Na}}{m_K}\right) + 1.252} - 273.15$	$T = \frac{1217}{\log\left(\frac{c_{Na}}{c_K}\right) + 1.483} - 273.15$	Fo79	(5.62)
Tonani (1980)	$T = \frac{833}{\log\left(\frac{m_{Na}}{m_K}\right) + 0.55} - 273.15$	$T = \frac{833}{\log\left(\frac{c_{Na}}{c_K}\right) + 0.78} - 273.15$	To80	(5.63)
Arnórsson et al. (1983a), 25–250 °C	$T = \frac{933}{\log\left(\frac{m_{Na}}{m_K}\right) + 0.762} - 273.15$	$T = \frac{933}{\log\left(\frac{c_{Na}}{c_K}\right) + 0.993} - 273.15$	Ar83, LT	(5.64)
Arnórsson et al. (1983a), 250–350 °C	$T = \frac{1319}{\log\left(\frac{m_{Na}}{m_K}\right) + 1.468} - 273.15$	$T = \frac{1319}{\log\left(\frac{c_{Na}}{c_K}\right) + 1.699} - 273.15$	Ar83, HT	(5.65)
Giggenbach (1988)	$T = \frac{1390}{\log\left(\frac{m_{Na}}{m_K}\right) + 1.52} - 273.15$	$T = \frac{1390}{\log\left(\frac{c_{Na}}{c_K}\right) + 1.75} - 273.15$	Gi88	(5.66)

(continued)

Table 5.2 (continued)

References	Na–K function involving molal concentrations	Na–K function involving concentrations in mg/kg	Code	Eqn. #
Nieva and Nieva (1987)	$\mathrm{T} = \frac{1178}{\log\left(\frac{m_{\mathrm{Na}}}{m_{\mathrm{K}}}\right)+1.239} - 273.15$	$\mathrm{T} = \frac{1178}{\log\left(\frac{c_{\mathrm{Na}}}{c_{\mathrm{K}}}\right)+1.470} - 273.15$	NiNi87	(5.67)
Kharaka and Mariner (1989)	$\mathrm{T} = \frac{1180}{\log\left(\frac{m_{\mathrm{Na}}}{m_{\mathrm{K}}}\right)+1.08} - 273.15$	$\mathrm{T} = \frac{1180}{\log\left(\frac{c_{\mathrm{Na}}}{c_{\mathrm{K}}}\right)+1.31} - 273.15$	KhMa89	(5.68)
Michard (1990)	$\mathrm{T} = \frac{1170}{\log\left(\frac{m_{\mathrm{Na}}}{m_{\mathrm{K}}}\right)+1.42} - 273.15$	$\mathrm{T} = \frac{1170}{\log\left(\frac{c_{\mathrm{Na}}}{c_{\mathrm{K}}}\right)+1.65} - 273.15$	Mi90	(5.69)
Verma and Santoyo (1997)[a]	$\mathrm{T} = \frac{1289}{\log\left(\frac{m_{\mathrm{Na}}}{m_{\mathrm{K}}}\right)+1.384} - 273.15$	$\mathrm{T} = \frac{1289}{\log\left(\frac{c_{\mathrm{Na}}}{c_{\mathrm{K}}}\right)+1.615} - 273.15$	VeSa97	(5.70)
Santoyo and Díaz-González (2010)[b]	$\mathrm{T} = \frac{876.3}{\log\left(\frac{m_{\mathrm{Na}}}{m_{\mathrm{K}}}\right)+0.6469} - 273.15$	$\mathrm{T} = \frac{876.3}{\log\left(\frac{c_{\mathrm{Na}}}{c_{\mathrm{K}}}\right)+0.8775} - 273.15$	SaDi10	(5.71)
Simmons (2013)	$\mathrm{T} = \frac{315}{\log\left(\frac{m_{\mathrm{Na}}}{m_{\mathrm{K}}}\right)-0.467} - 273.15$	$\mathrm{T} = \frac{315}{\log\left(\frac{c_{\mathrm{Na}}}{c_{\mathrm{K}}}\right)-0.2364} - 273.15$	Si13	(5.72)

[a] Uncertainty of ±76 units on A and ±0.179 units on B
[b] Uncertainty of ±26.26 units on A and ±0.0508 units on B

The Na–K geothermometric function of White (1968) corresponds to curve B in his Fig. 2, in which other four curves are depicted. It is derived from Fig. 2 of Ellis and Mahon (1967) and is valid from 60 to 700 °C. Owing to this wide temperature range, this function has a relatively high uncertainty.

The Na–K geothermometer of Ellis (1970) is expected to work in a much smaller temperature range, from 175 to 300 °C, because the aluminum-silicate equilibria are not certain at temperatures lower than ca. 175–200 °C, according to the author. Ellis (1970) noted that "*with cooling of water, e.g., through boiling on rising towards the surface, the Na/K exchange reaction is slower to readjust than the silica equilibrium. A memory of deep temperatures is carried upwards, but the temperatures indicated by the silica and the Na/K method may disagree, the latter showing a higher temperature. The Na/K ratio can for example indicate whether or not higher temperatures exist beneath the depth of drilling (Mahon* 1970*). The Na/K method is a more reliable method for estimating deep temperatures from spring flows, but for drillhole discharges, the silica method is capable of giving more accurate temperatures at the production levels.*"

The Na–K geothermometric relation of Mercado (1970) was calibrated with the geothermal liquids discharged from ten Cerro Prieto wells, whose temperatures range from 130 to 375 °C.

Truesdell (1976) reports two Na–K geothermometric equations, one based on Ellis and White diagrams, the other from Fournier and Truesdell (1973). As underscored by Truesdell (1976) as well, the Na–K geothermometer is less affected by re-equilibration and near-surface dilution than are the silica geothermometers, but it fails at temperatures below 100–120 °C.

The Na–K geothermometric function of Fournier (1979) was calibrated using data from boreholes drilled in geothermal systems in a wide variety of geological environments and spanning a large temperature interval, from 80 to 340 °C. Fournier (1979) noted that most waters from aquifers with temperatures higher than 80–100 °C have Na/K ratios intermediate between those of the aqueous solutions in equilibrium with low-albite and maximum-microcline and those of the waters in saturation with high-albite and high-sanidine, based on the thermodynamic data of Helgeson (1969).

According to Fournier (1979), at temperatures greater than 100–150 °C, exchange of Na^+ and K^+ ions between coexisting alkali feldspars may govern the Na/K ratio in most natural waters. At temperatures lower than 100–150 °C, either equilibrium is not attained or other solid phases, such as clays, micas, and zeolites control dissolved Na and K. Consequently, the Na–K geothermometer usually works well for waters from aquifers with temperature higher than 150–200 °C, but overestimates reservoir temperatures for waters from environments where temperatures is less than 100 °C approximately.

Tonani (1980) proposed to use the Na–K geothermometer together with the Ca–Na and Ca–K functions[6] obtained from the Na–K–Ca geothermometer of Fournier and Truesdell (1973) because the simultaneous use of the three separate geothermometers (two of which are independent) has the advantage of allowing some degree

---

[6] These functions are presented in Sect. 5.4.

of internal cross-checking, which is impossible by using a linear combination of the geothermometers, like the Na–K–Ca geothermometer of Fournier and Truesdell (1973).

Arnórsson et al. (1983a) presented two distinct equations, one for temperatures from 25 to 250 °C, the other for higher temperatures, up to 350 °C. Arnórsson et al. (1983a) underscored that the Na/K ratios given by these two functions agree with those fixed by equilibrium coexistence of the aqueous solution with low-albite and maximum-microcline, based on the thermodynamic data of Helgeson (1969). In contrast, the thermodynamic data of Helgeson et al. (1978) give a much worse fit. Arnórsson et al. (1983a) presented also two temperature functions to be used with activities of Na^+ and K^+ ions. One is linear in 1/T and is valid from 25 to 250 °C. The other is a polynomial equation and can be used from 25 to 350 °C. They agree within few degrees with Eq. (5.64) and (5.65) and therefore are not considered any further here below.

Giggenbach (1988) calibrated a Na–K relationship (already reported by Giggenbach et al. 1983) based on the analytical data of a large number of deep well discharges, including those of Fournier (1979) and Fournier and Potter (1979). The maximum Na/K ratios at a given temperature were considered to constrain the Na–K geothermometric function, assuming that equilibrium Na/K ratios are approached from lower values, which are initially controlled by rock dissolution.

Nieva and Nieva (1987) devised a systematic, computerized procedure, taking into account the six distinct exchange reactions involving pair of cations (Na^+, K^+, Ca^{2+}, and Mg^{2+}) and some combinations of such reactions. The Na–K geothermometer of Nieva and Nieva (1987) applies to waters with total cation content (sum of the concentrations of $Na + K + Mg + Ca$) > 8 meq/L and $\%Mg \leq 3.5$.

The Na–K geothermometer of Kharaka and Mariner (1989) was developed to evaluate the temperatures at depth in sedimentary basins, which are generally in the range 30–200 °C. Moreover, these environments have water salinities and pressures usually much greater than those occurring in geothermal systems sustained by magmatic processes.

The empirical Na–K geothermometer of Michard (1990) was calibrated with waters interacting with granitic rocks at temperatures lower than 150 °C and should be used in the temperature range 50–150 °C. Aquifer temperatures were calculated by Michard (1990) using the log(Q/K) versus temperature diagram (i.e., multicomponent chemical geothermometry, see Sect. 2.3.2) and the silica, Na–K–Ca, and Na–K geothermometers. Therefore, the good correlation between the logarithm of the Na/K ratio and the absolute temperature inverse is partly biased by a circular argument, as recognized by the author. Michard (1990) underscored that his Na–K relation is similar to the temperature dependence of the equilibrium constant of the ion exchange reaction involving albite and adularia[7].

---

[7] The thermodynamic data used by Michard (1990) are given in the report EUR 8590 FR entitled "*Recueil de données thermodynamiques concernant les équilibres eaux-minéraux dans les réservoirs géothermaux*", which was prepared by Prof. Gil Michard for the European Commission in 1983. Unfortunately, we were not able to find this report.

The function proposed by Verma and Santoyo (1997) is a refinement of the Na–K geothermometer of Fournier (1979) and was obtained by a statistical procedure consisting of detection and rejection of outliers, ordinary linear regression, and error propagation theory. Santoyo and Díaz-González (2010) adopted a similar statistical approach, but used a different geochemometric method and considered a larger and more representative chemical database of geothermal fluids. Quite surprisingly, the enthalpy term turned out to be relatively low and similar to the values of the early studies.

The function of Simmons (2013) involves the Na/K activity ratio and is empirical, being a best fit function of the data from some geothermal fields of the United States, namely Beowave, Dixie Valley, Long Valley-Mammoth, Roosevelt Hot Springs, and Raft River. It applies in the temperature range 120–270 °C. As noted by Simmons (2013), a small interval of Na/K activity ratios corresponds to a large range of temperatures due to the small slope of this empirical equation, whose usefulness needs to be proven.

In addition to the Na–K geothermometers considered so far, it is worth recalling the Na–K function of Arnórsson (2000):

$$\mathrm{T} = 733.6 - 770.551 \cdot \alpha + 378.189 \cdot \alpha^2 - 95.753 \cdot \alpha^3 + 9.544 \cdot \alpha^4, \qquad (5.73)$$

in which T is temperature in °C and $\alpha = \log(m_{\mathrm{Na}}/m_{\mathrm{K}})$. This Na–K function was calibrated theoretically, based on the equilibrium condition between the aqueous solution, pure low-albite and pure microcline, both of which were assumed to be fully ordered. Arnórsson (2000) obtained the thermodynamic properties of Na^+ and K^+ ions from Shock and Helgeson (1988) and those of low-albite and microcline from Arnórsson and Stefánsson (1999). However, the reliability of the thermodynamic data of alkali feldspar of Arnórsson and Stefánsson (1999) is questionable, as shown in Sect. 4.2.4.

The Na–K geothermometric relations obtained through use of artificial neural network (e.g., Bayram 2001; Can 2002; Serpen et al. 2009) are not considered here because they add little to the present discussion, although their performance is superior to that of the Na–K equation utilized to provide input data.

5.3.2 *Why so Many Empirical Na–K Geothermometers Were Derived in Previous Studies?*

Sixteen different empirical Na–K functions are listed in Table 5.2 and were briefly described in previous section. They might seem too many and, indeed, Arnórsson (1998) noted that "*it was in fashion that every geochemist studied the relationship between aquifer temperature and aqueous Na/K ratios in "his" wells and, as a product, came up with a new calibration. Careful assessment of experimental data has just recently resulted in a theoretical calibration of this geothermometer so all*

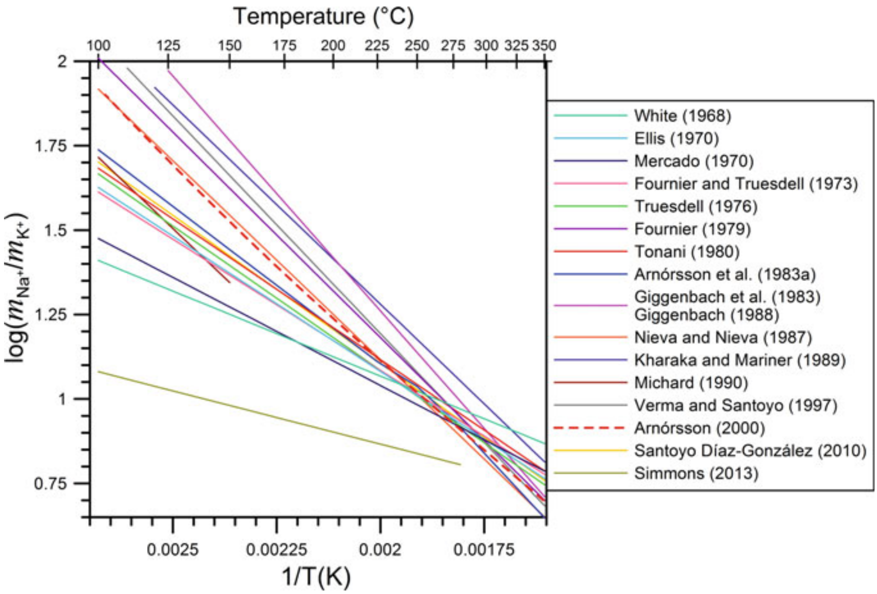

Fig. 5.14 Diagram of $\log(m_{\mathrm{Na}}/m_{\mathrm{K}})$ versus the absolute temperature inverse showing the sixteen empirical Na–K geothermometers (see legend) and the theoretical Na–K function of Arnórsson (2000). To be noted that Arnórsson et al. (1983a) presented two distinct empirical Na–K equations, one for 25 < T < 250 °C, the other for 250 < T < 350 °C

the empirical calibrations can now be forgotten". Perhaps not every geochemist calibrated his/her own Na–K geothermometer, but certainly many geochemists did so. Can we really forget about all the empirical Na–K geothermometers or should we try to understand why so many Na–K functions have been proposed in previous studies?

To answer this questions let us examine the plot of $\log(m_{\mathrm{Na}}/m_{\mathrm{K}})$ versus the absolute temperature inverse of Fig. 5.14, showing all the empirical Na–K geothermometric functions listed in Table 5.2 and the theoretical equation of Arnórsson (2000), i.e., Eq. (5.73).

If we showed this graph to a child, she/he would probably recognize pick-up sticks, a game in which a bundle of sticks are dropped as a loose bunch onto a table or the floor, jumbling into a random pile. Looking at the graph seriously, it can be noted that the scatter of the lines increases with decreasing temperature, whereas several lines converge at temperatures higher than ~250 °C. The function of Arnórsson (2000) passes more or less in the middle of the bundle, but it cannot be adopted as the best Na–K geothermometer, unless we are able to prove that the Na–K functions deviating from it are wrong because of one or more reasons which must be properly understood.

The presence of poorly equilibrated waters in the datasets chosen for calibrating the empirical Na–K geothermometers, especially the early ones, was invoked by some authors (e.g., Fournier 1979 and Giggenbach 1988) to reject the relationships characterized by low slopes. Among the three functions having the lowest slopes, those of White (1968) and Michard (1990) might actually be influenced by far-from-equilibrium aqueous solutions. However, the function of Mercado (1970) is constrained by the reservoir liquids tapped by ten Cerro Prieto wells with temperatures in the interval 130–375 °C, as noted in the previous section. Therefore, the influence of low-temperature, poorly equilibrated waters does not seem to be a convincing explanation, at least for the relation of Mercado (1970).

Further evidence on this important point is provided by the correlation diagrams of $\log(m_{\mathrm{Na}}/m_{\mathrm{K}})$ versus the absolute temperature inverse of Fig. 5.15. In these plots, most of the 1013 selected reservoir liquids are found in the same area occupied by the sixteen empirical Na–K functions and the theoretical Na–K relation of Arnórsson (2000). Based on this good correspondence between the Na–K geothermometers and the selected reservoir liquids and assuming that the latter ones or at least most of them are representative of mineral-solution thermochemical equilibrium at aquifer temperatures of 100–350 °C, it can be concluded that all the Na–K geothermometric functions are plausible, because it is possible to choose a suitable set of reservoir liquids consistent with each geothermometer.

This implies that there is not a unique Na–K geothermometer, but an infinite number of Na–K geothermometers. The Na–K functions proposed so far, therefore, are not too many but are rather a small number compared to the infinite possibilities. They should not be forgotten but rather used to gain knowledge on the identity of the minerals governing the Na–K geothermometers, another key point representing the subject of the next section.

A diagram like that of Fig. 5.15, although reporting only the six Na–K geothermometers of Truesdell (1976), Fournier (1979), Tonani (1980), Arnórsson et al. (1983a), Giggenbach et al. (1983), and Nieva and Nieva (1987), was previously presented and discussed by Fournier (1991) who concluded that "*there is no single universally best Na/K geothermometer because one may give the correct temperature in one place and an erroneous temperature in another, depending on the particular mineral assemblage (and structural state of the minerals) with which the circulating water equilibrates.*"

5.3.3 The Hydrothermal Minerals Controlling the Na–K Geothermometers

Albites and adularias were suggested as the most probable candidates by several authors (e.g., White 1965; Ellis 1970; Fournier 1979; Arnórsson et al. 1983a; Giggenbach 1988; Michard 1990), although other solid phases, such as clays, micas, and zeolites were proposed to control dissolved Na and K concentrations, especially at low temperatures (e.g., Fournier and Truesdell 1970; Fournier 1979, 1991).

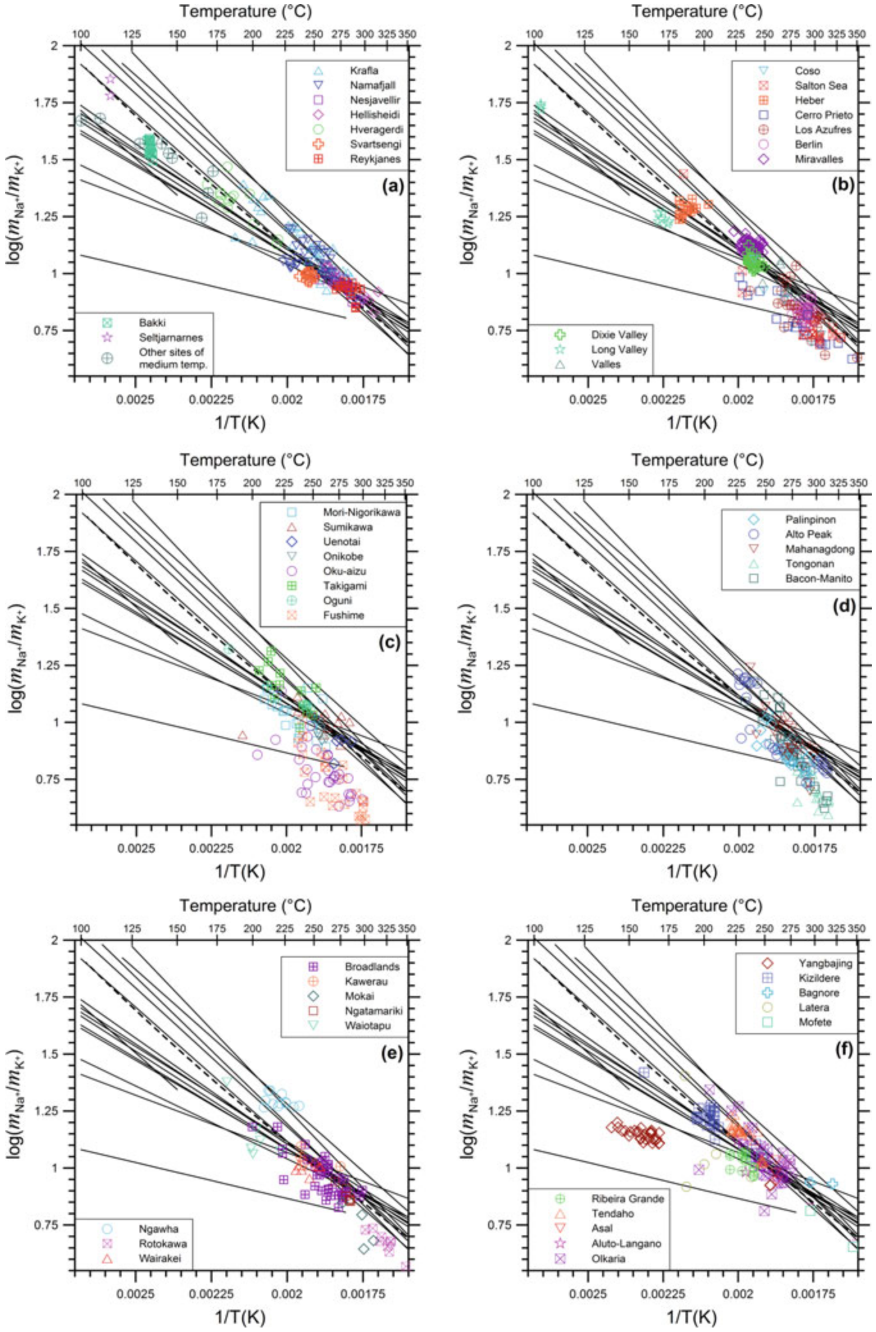

Fig. 5.15 Diagrams of $\log(m_{\mathrm{Na}}/m_{\mathrm{K}})$ versus the absolute temperature inverse showing the selected reservoir liquids from **a** Iceland, **b** Northern-Central America, **c** Japan, **d** The Philippines, **e** New Zealand, and **f** miscellaneous geothermal systems as well as the sixteen empirical Na–K geothermometers (solid black lines) and the theoretical Na–K function of Arnórsson (2000; dashed black line)

To gain more information on the minerals governing the Na–K geothermometers, it is useful to compare the ΔH°_r and ΔS°_r values of the empirical Na–K functions, calculated from their slope and intercept using Eqs. (5.13) and (5.14), with the enthalpies and entropies of the Na–K exchange reactions involving the pertinent solid phases mentioned above. Since no clays and zeolites are included in the thermodynamic dataset of Helgeson et al. (1978), the thermodynamic properties of Na–montmorillonite, K-montmorillonite, Na–clinoptilolite, and K-clinoptilolite were obtained from Wolery et al. (2007) and these four minerals were added to the SUPCRT92 database. Then, SUPCRT92 was run to calculate the thermodynamic properties of the reactions of interest, as a function of temperature at water saturation pressure. The considered reactions are:

(i) low-albite/maximum-microcline (L–Ab/Mc), low-albite/high-sanidine (L–Ab/Sa), high-albite/maximum-microcline (H–Ab/Mc), and high-albite/high-sanidine (H–Ab/Sa), all described by:

$$\mathrm{NaAlSi_3O_8 + K^+ = KAlSi_3O_8 + Na^+}. \tag{5.74}$$

(ii) paragonite/muscovite (Prg/Ms):

$$\mathrm{NaAl_3Si_3O_{10}(OH)_2 + K^+ = KAl_3Si_3O_{10}(OH)_2 + Na^+}. \tag{5.75}$$

(iii) Na–clinoptilolite/K-clinoptilolite (Na–Cpt/K–Cpt):

$$\begin{aligned} &0.909\quad \mathrm{Na_{1.1}Si_{4.9}Al_{1.1}O_{12} \cdot 3.5H_2O + K^+} \\ &\quad = 0.909\ \mathrm{K_{1.1}Si_{4.9}Al_{1.1}O_{12} \cdot 2.7H_2O + Na^+ + 0.727H_2O} \end{aligned} \tag{5.76}$$

(iv) Na–montmorillonite/K-montmorillonite (Na–Mm/K–Mm):

$$\begin{aligned} &\mathrm{3.03Na_{0.33}Mg_{0.33}Al_{1.67}Si_4O_{10}(OH)_2 + K^+} \\ &\quad = \mathrm{3.03K_{0.33}Mg_{0.33}Al_{1.67}Si_4O_{10}(OH)_2 + Na^+}. \end{aligned} \tag{5.77}$$

The correlation plot of Fig. 5.16 shows that the ΔH°_r and ΔS°_r values of the sixteen empirical Na–K geothermometric equations or at least most of them are intermediate between the enthalpies and entropies of the low-albite/high-sanidine exchange reaction and those of the low-albite/maximum-microcline exchange reaction or, less likely, of the high-albite/high-sanidine exchange reaction. In contrast, the ΔH°_r and ΔS°_r values of the sixteen empirical Na–K geothermometric equations

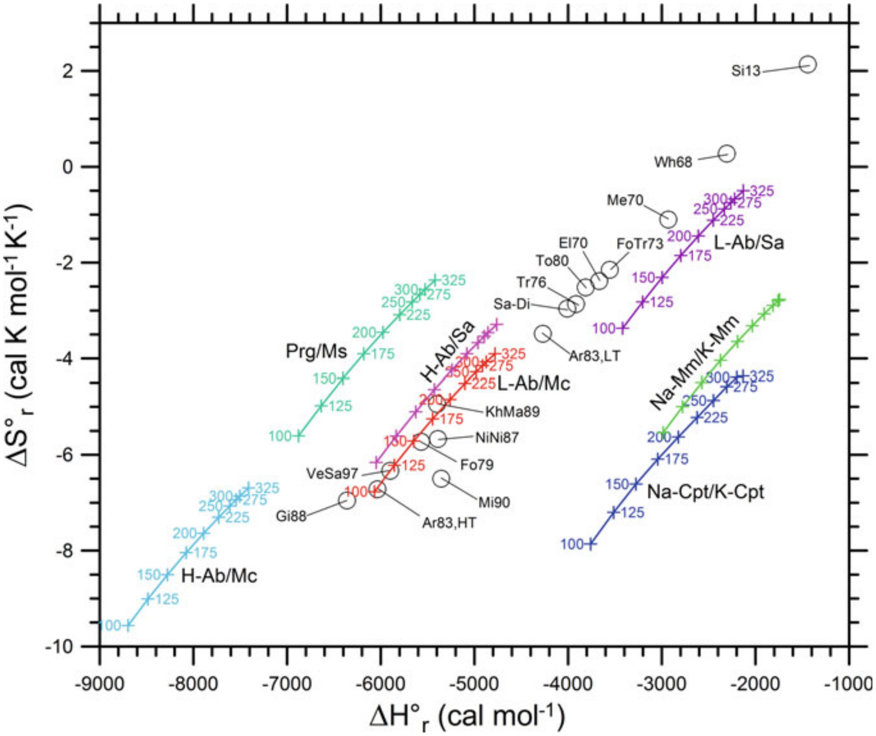

Fig. 5.16 Comparison of the temperature-independent standard enthalpies and entropies of the sixteen empirical Na–K geothermometers (open black circles), obtained from their slope and intercept, with the standard enthalpies and entropies of the Na–K exchange reactions low-albite/maximum-microcline (L–Ab/Mc), low-albite/high-sanidine (L–Ab/Sa), high-albite/maximum-microcline (H-Ab/Mc), high-albite/high-sanidine (H–Ab/Sa), paragonite/muscovite (Prg/Ms), Na-clinoptilolite/K-clinoptilolite (Na–Cpt/K–Cpt), and Na–montmorillonite/K-montmorillonite (Na–Mm/K–Mm), computed as a function of temperature at water saturation pressure using SUPCRT92

are at variance with the enthalpies and entropies of the Na–K exchange reactions comprising high-albite and maximum-microcline as well as micas, clinoptilolites, and montmorillonites.

5.3.4 Conclusive Remarks on the Na–K Geothermometers

Summing up, it appears that there is not a unique Na–K geothermometer, but that all the Na–K geothermometers proposed so far are plausible and that they are a small number compared to the infinite number of possible Na–K geothermometers, as already underscored by Fournier (1991).

Based on the ΔH°_r and ΔS°_r values of the sixteen empirical Na–K geothermometers of interest, it turns out that they are probably controlled by the exchange reactions low-albite/high-sanidine or low-albite/maximum-microcline or any "in-between" exchange reaction, involving low-albite and adularia with a degree of ordering intermediate between that of fully ordered maximum-microcline and that of completely disordered high-sanidine whereas the possible role of the high-albite/high-sanidine exchange reaction appears to be much less likely. These inferences are consistent with the indications given by the authigenic alkali feldspars occurring in sedimentary rocks and synthesized by means of hydroxide gels (see Sect. 4.2.3).

Furthermore, our conclusions represent a step forward with respect to previous findings of Bird and Norton (1981) and Bird and Helgeson (1981), who showed that the tetrahedral site distributions of Al^{3+} and Si^{4+} ions in coexisting alkali feldspars have a dramatic influence on the Na^+/K^+ activity ratio in the aqueous phase and on the temperatures given by Na–K geothermometers. According to Bird and Norton (1981) "*metastable tetrahedral ordering in alkali feldspars is a likely cause of many of the discrepancies found among alkali cation geothermometers and actual measured temperatures in geothermal systems*".

Accepting our conclusions, it follows that there is no reason to look for the universally best Na–K geothermometer, either empirical or theoretical, that can be applied everywhere because it does not exists. Rather than using the Na/K ratio as the basis for an infinite number of geothermometers, it is advisable to use it for obtaining different indications, changing completely the approach to water geothermometry. This discussion will be resumed in Chap. 6.

5.4 The Na–K–Ca Geothermometer

5.4.1 Formulation, Controlling Reactions, and Limitations/Problems of the Na–K–Ca Geothermometer

The Na–K–Ca geothermometer is one of the most popular and used empirical geothermometers, although it is affected by a certain number of limitations and problems. We consider the Na–K–Ca geothermometer immediately after the Na–K geothermometer because of the strict link between these two functions. Such a link was pointed out by Fournier and Truesdell (1973) who decided to introduce Ca in a revised and expanded Na–K geothermometer because of at least two distinct reasons. One reason is that the Na–K geothermometer does not yield reasonable results for Ca-rich waters. The other reason is that Ca^{2+} ion may have an effect upon the Na/K ratio of the aqueous solution as suggested by the reaction in which plagioclase is destructed and K-feldspar is produced with the simultaneous exchange of K^+ ion for both Na^+ and Ca^{2+} ions. Fournier and Truesdell (1973) postulated that "*aqueous*

Na–K–Ca relationships generally can be explained entirely in terms of silicate reactions even though the absolute quantity of aqueous Ca is controlled by the solubility of carbonate"[8]. According to Fournier and Truesdell (1973), the reactions involving silicate minerals and controlling Na–K–Ca relationships have net stoichiometry:

$$Na_{2/3}Ca_{1/6} - \text{solid} + K^{+} = 1/6Ca^{2+} + 2/3Na^{+} + K - \text{solid}, \tag{5.78}$$

above 100 °C, and:

$$Ca_{2/3} - \text{solid} + K^{+} + 1/3Na^{+} = 2/3Ca^{2+} + KNa_{1/3} - \text{solid} \tag{5.79}$$

below 100 °C. Fournier and Truesdell (1973) did not provide the temperature dependence of the log K of reactions (5.78) and (5.79), but only the following overall relation (concentrations in mg/kg):

$$T(°C) = \frac{1647}{\log(c_{Na}/c_{K}) + \beta \cdot [\log(\sqrt{c_{Ca}}/c_{Na} + 2.06] + 2.47} - 273.15, \tag{5.80}$$

in which β may be equal to 1/3 or 4/3. To choose the proper value of β, Fournier and Truesdell (1973) suggested to proceed as follows: Express the concentrations of dissolved species in units of molality and calculate $\log(\sqrt{Ca}/Na)$. If $\log(\sqrt{Ca}/Na)$ is positive, compute the Na–K–Ca temperature for $\beta = 4/3$. The obtained Na–K–Ca temperature is correct, if it is <100 °C. Otherwise, recalculate the Na–K–Ca temperature for $\beta = 1/3$. However, β can be assumed equal to 1/3 for aquifer temperature >100 °C, as is the case of the 1013 reservoir liquids of interest.

Precipitation of calcite causes an overestimation of the equilibrium temperature obtained by means of the Na–K–Ca function, as already recognized by Fournier and Truesdell (1973). Mixing has limited effects on the Na–K–Ca geothermometer if the high-temperature water has salinity much greater than the low-temperature water and if the fraction of the geothermal water is higher than 0.2–0.3. Otherwise, the effects of mixing on the Na–K–Ca geothermometer should be taken into consideration, as discussed by Fournier (1981).

Fournier and Potter (1979) noted that many Mg-rich waters have high Na–K–Ca temperatures, well above 150 °C, which are unexpected considering that all high-temperature (>175 °C) waters discharged from boreholes drilled into active geothermal systems have low concentrations of Mg relative to the other dissolved cations. Therefore, based on the value of $R = [Mg/(Mg + Ca + K)] \cdot 100$, with concentrations expressed in equivalent units, Fournier and Potter (1979), proposed two different temperature corrections, Δt_{Mg} (in °C), that should be subtracted from

---

[8] Actually, this hypothesis is erroneous because Ca^{2+} activity cannot be constrained by both calcite and a Ca–Al-silicate at the same time, as hypothesized by Fournier and Truesdell (1973). In case of coexistence of calcite and a Ca–Al-silicate, calcite fixes the activity of the carbonate species of reference [either $CO_{2(aq)}$ or HCO_3^{-} or CO_3^{2-}], whereas the Ca–Al-silicate constrains the activity of Ca^{2+} ion. However, Fournier and Truesdell (1973) excluded calcite and CO_2 from reactions (5.78) and (5.79).

the Na–K–Ca temperature, T. For 5 < R < 50 and T > 70 °C:

$$\Delta t_{Mg} = 10.66 - 4.7415 \cdot R + 325.87 \cdot (\log R)^2 - 1.032 \times 10^5 \cdot \frac{(\log R)^2}{T} - 1.968 \times 10^7 \cdot \frac{(\log R)^2}{T^2} + 1.605 \times 10^7 \cdot \frac{(\log R)^3}{T^2}. \tag{5.81}$$

For 0.5 < R < 5:

$$\Delta t_{Mg} = -1.03 + 59.971 \cdot \log R + 145.05 \cdot (\log R)^2 - 36711 \cdot \frac{(\log R)^2}{T} - 1.67 \times 10^7 \cdot \frac{\log R}{T^2}. \tag{5.82}$$

Irrespective of the R value, the Mg correction should not be applied if Δt_{Mg} is negative. Moreover, Fournier and Potter (1979) suggested that Mg-rich waters may be unsuitable for the application of geothermometers because high Mg concentrations indicate the occurrence of water-rock reactions at relatively low temperatures, causing not only Mg acquisition but also possible changes in the concentrations of other dissolved constituents.

The behavior of the Na–K–Ca geothermometer has stimulated the interest of several authors, who approached this topic both theoretically and experimentally. Shikazono (1976) and Michard and Fouillac (1976) provided a thermodynamic interpretation of the Na–K–Ca geothermometer.

Shikazono (1976) underscored that in NaCl aqueous solutions in equilibrium with typical hydrothermal minerals at fixed temperature, the logarithms of Na^+, K^+, and Ca^{2+} molalities are linear functions of the logarithm of Cl^- molality. The linear functions involving alkali cations have slope 1, whereas those comprising alkali-earth cations have slope 2.

According to Michard and Fouillac (1976), above 100 °C, the Na–K–Ca geothermometer is controlled by the equilibration of the aqueous solution with K-feldspar and a plagioclase of nearly constant composition close to $Ab_{0.8}An_{0.2}$. In contrast, below 100 °C, water chemistry is assumed to be controlled by the relative dissolution kinetics of relevant minerals and the Na–K–Ca geothermometer would be chiefly explained by the increasing salinity with temperature.

Janecki et al. (1986) performed laboratory experiments at 260, 280, 300, 320, and 340 °C, reacting granite disks in 10 mmol/kg NaCl solutions and in mixed solutions containing 10 mmol/kg NaCl and 0.1 mmol/kg $CaCl_2$. Hydrothermal batch reactors were used for all the experiments, keeping total pressure at 272 bar, except one run that was performed in a flow-through reactor. According to Janecki et al. (1986), variations in solution chemistry closely follow the empirical Na–K–Ca geothermometric function although weak deviations were observed at 340 °C. Primary minerals composing the granite were etched. Authigenic minerals recognized at the end of the runs comprise minor quantities of Fe–, Mg–, Ca-rich clay minerals and a Ca-silicate (truscottite or a similar phase) at all temperatures, a Ca-zeolite (possibly faujasite) below 300 °C, feldspar overgrowths (apparently albitic) above 300 °C, and amphibole overgrowths at 340 °C.

Benjamin et al. (1983) performed a thorough review of the Na–K–Ca geothermometer. Through the least-squares fit of the Fournier and Truesdell data, they obtained the following revised Na–K–Ca geothermometric relations:

$$\mathrm{T(°C)} = \frac{22200}{64.2 - \log(\mathrm{Na/K}) + 6.3 \cdot \log(\sqrt{\mathrm{Ca}}/\mathrm{Na})} - 273.15 \tag{5.83}$$

$$\mathrm{T(°C)} = \frac{1416}{\log(\mathrm{Na/K}) + 0.055 \cdot \log(\sqrt{\mathrm{Ca}}/\mathrm{Na}) + 1.69} - 273.15 \tag{5.84}$$

Equation (5.83) applies to $T \leq 100$ °C and it is of little interest for us, whereas Eq. (5.84) is valid for $T > 100$ °C and deserves more attention. It is consistent with a $\Delta H°_r$ of -6480 ± 260 cal mol^{-1} and a $\Delta S°_r$ of -7.74 ± 0.50 cal mol^{-1} K^{-1}. The error on the stoichiometric coefficient β is ± 0.053, whereas the error on the computed temperatures varies from 10 to 25 °C.

Benjamin et al. (1983) performed also experimental studies reacting separately two granodiorites and a basalt with distilled water, both in a fixed-temperature circulation system, at 200 and 300 °C, and in a controlled-temperature-gradient circulation system, at 72, 119, 161, 209, 270, and 310 °C, for 1440 h. Pressure was kept at 1/3 kbar in all the experiments. The duration of the fixed-temperature experiments was 6579 and 5816 h for those with the granodiorites and 3600 h for that with the basalt. Concentrations of Na, K, and Ca attained steady state after 2–4 weeks approximately, but cation ratios stabilized in a few days. Overgrowths of zeolites, usually Ca-rich, and clay minerals of variable composition were found over the primary minerals at the end of the runs. Based on their analytical results, Benjamin et al. (1983) computed a stoichiometric coefficient β of 0.98 ± 0.10 for the Na–K–Ca geothermometric function as well as a $\Delta H°_r$ of $-10{,}300 \pm 1100$ cal mol^{-1} and a $\Delta S°_r$ of -13.3 ± 1.7 cal mol^{-1} K^{-1} for its controlling reaction which was written as follows:

$$\begin{aligned} &\mathrm{K^+ + 0.02NaAlSi_3O_8 + 0.49CaAl_2Si_2O_8 + 1.96SiO_2} \\ &\quad = \mathrm{0.02Na^+ + 0.49Ca^{2+} + KAlSi_3O_8} \end{aligned} \tag{5.85}$$

adopting a stoichiometric coefficient of K^+ ion equal to 1. Reaction (5.85) is essentially a Ca-K exchange reaction with a marginally involvement of Na^+ ion. Benjamin et al. (1983) were forced to interpret their experimental results in this way, owing to the lack of thermodynamic data for zeolites and clay minerals, although they recognized that feldspar endmembers do not govern solution chemistry. To be noted that the $\Delta H°_r$ and $\Delta S°_r$ values and the stoichiometric coefficient β derived from the results of the hydrothermal experiments are significantly different from those obtained through the least-squares fit of the Fournier and Truesdell data for T > 100 °C. These differences suggest that the hydrothermal experiments did not reproduce the water-rock reactions controlling Na–K–Ca relations in natural geothermal systems.

Pope et al. (1987) performed another experimental study in which a powdered peralkaline rhyolite was reacted with distilled water in separate runs with 0.1 M NaCl and 0.01 M $NaHCO_3$ at different temperatures in the range 100–500 °C, mostly at 200 and 300 °C, maintaining total pressure at 1 kbar. Reactants were sealed inside gold capsules. Run durations were usually 2–3 weeks, with some longer experiments to control the attainment of equilibrium or steady-state conditions. No alteration mineral was detected by SEM and XRD analyses but the presence of alteration minerals in small quantities cannot be excluded. The Na–K–Ca geothermometer works well for the experiments with 0.1 M NaCl. In fact, the mean computed Na–K–Ca temperatures are 191 ± 14 °C and 297 ± 14 °C, at 200 and 300 °C, respectively. In contrast, the Na–K–Ca temperatures are lower than the experimental values by 10–50 °C for the experiments with 0.01 M $NaHCO_3$. These poor results are ascribable, at least partly, to the low Ca concentrations, which are close to detection limit at 200 °C and are generally below detection limit at 300 °C.

5.4.2 Performance of the Na–K–Ca Geothermometer for the Selected Reservoir Liquids

The temperature given by the Na–K–Ca geothermometer of Fournier and Truesdell (1973) for the 1013 selected reservoir liquids is contrasted with the aquifer temperature in the binary diagrams of Fig. 5.17.

Among the Icelandic geothermal systems (Fig. 5.17a), the average absolute deviation of the Na–K–Ca temperature from the reservoir temperature is: (i) 18 ± 10 (1σ) °C for the high-temperature (>175 °C), low-salinity reservoir liquids of Hellisheidi, Hveragerdi, Krafla, Namafjall, and Nesjavellir; (ii) 35 ± 12 °C for the high-temperature reservoir liquids of Reykjanes; (iii) 6 ± 3 °C for the high-temperature reservoir liquids of Svartsengi; (iv) 11 ± 5 °C for the medium-temperature (<175 °C) Icelandic reservoir liquids. The Na–K–Ca geothermometer has a good performance at Svartsengi and a very poor behavior at Reykjanes, although both systems are similar, being partly recharged by seawater. The Na–K–Ca geothermometer has a poor performance for the high-temperature (>175 °C), low-salinity reservoir liquids, whereas it works relatively well for the medium-temperature (<175 °C) Icelandic reservoir liquids. The Na–K–Ca temperature is higher than the aquifer temperature for most liquids from Hveragerdi and the medium-temperature systems. In contrast, the Na–K–Ca geothermometer underestimates the aquifer temperature for most reservoir liquids of Hellisheidi, Krafla, Namafjall, Nesjavellir, Reykjanes, and Svartsengi.

Among the geothermal systems of Northern and Central America (Fig. 5.17b), the average absolute deviation of the Na–K–Ca temperature from the aquifer temperature is: (i) 5 ± 3 (1σ) °C for Dixie Valley; (ii) 42 ± 6 °C for Long Valley; (iii) 14 ± 6 °C

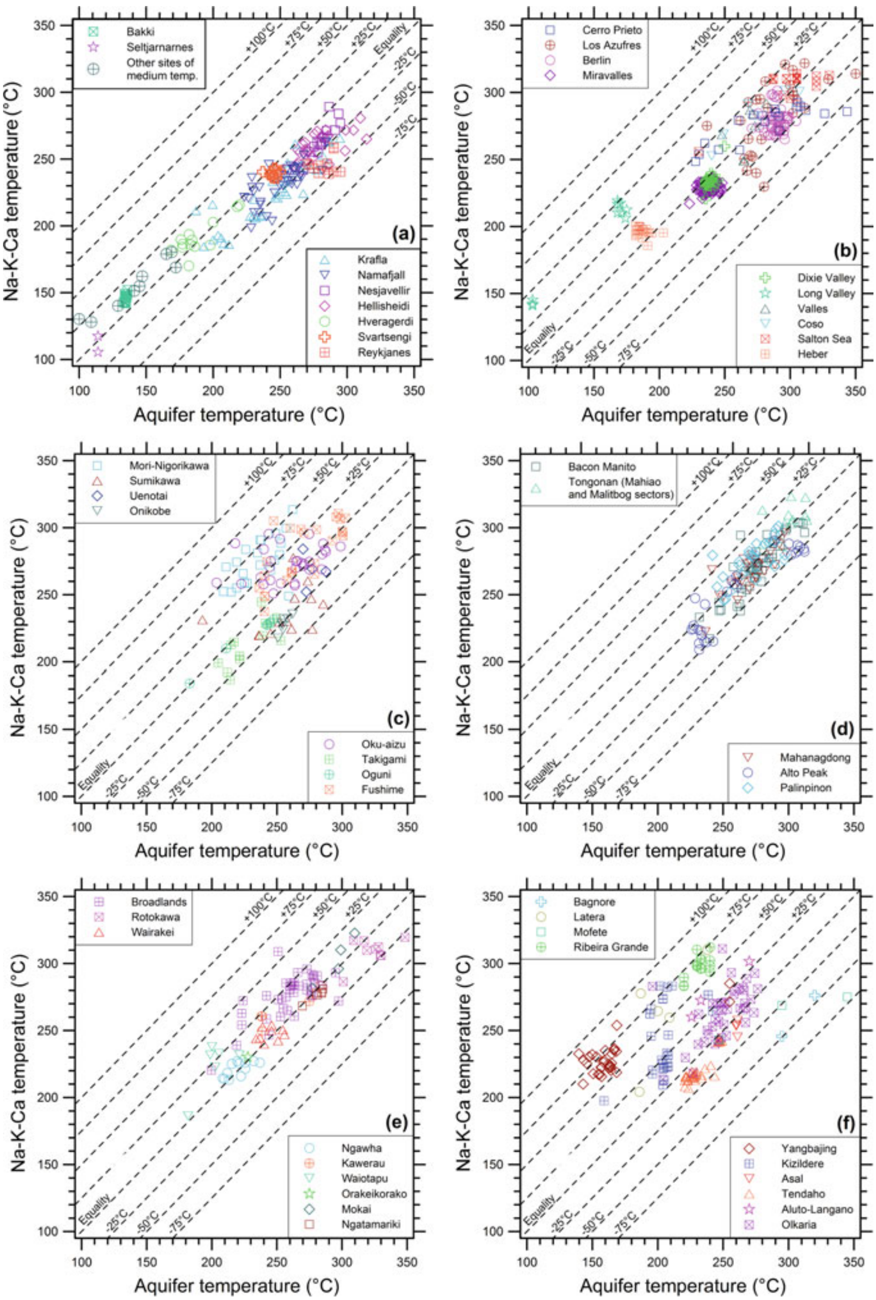

Fig. 5.17 Correlation diagrams of the temperature given by the Na–K–Ca geothermometer of Fournier and Truesdell (1973) versus the aquifer temperature for the selected reservoir liquids from **a** Iceland, **b** Northern-Central America, **c** Japan, **d** The Philippines, **e** New Zealand, and **f** miscellaneous geothermal systems

for Valles; (iv) 14 ± 8 °C for Coso; (v) 13 ± 7 °C for Salton Sea; (vi) 10 ± 5 °C for Heber; (vii) 17 ± 14 °C for Cerro Prieto; (viii) 19 ± 12 °C for Los Azufres; (ix) 14 ± 7 °C for Berlin; (x) 9 ± 4 °C for Miravalles. The Na–K–Ca geothermometer has a good performance at Dixie Valley and a relatively good performance at Miravalles and Heber, whereas its behavior is very poor at Long Valley and relatively poor in the other systems. The Na–K–Ca temperature overestimates considerably and systematically the aquifer temperature at Long Valley.

Among the geothermal systems of Japan (Fig. 5.17c), the average absolute deviation of the Na–K–Ca temperature from the reservoir temperature is: (i) 41 ± 12 (1σ) °C for Mori-Nigorikawa; (ii) 19 ± 4 °C for Sumikawa; (iii) 16 ± 5 °C for Uenotai; (iv) 27 ± 3 °C for Onikobe; (v) 18 ± 18 °C for Oku-aizu; (vi) 16 ± 10 °C for Takigami; (vii) 11 ± 7 °C for Oguni; (viii) 14 ± 14 °C for Fushime. The Na–K–Ca geothermometer has a very poor behavior at Mori-Nigorikawa and Onikobe and a poor performance is all the other geothermal systems Japan, apart from Oguni, to some extent. The Na–K–Ca temperature is higher than the reservoir temperature in most wells of Mori-Nigorikawa and in several wells of Oku-aizu and Fushime, whereas the reverse situation occurs frequently at Sumikawa, Uenotai, Onikobe, Takigami, and Oguni.

Among the geothermal systems of the Philippines (Fig. 5.17d), the average absolute deviation of the Na–K–Ca temperature from the aquifer temperature is: (i) 8 ± 7 °C for Bacon-Manito; (ii) 10 ± 9 °C for Tongonan; (iii) 8 ± 7 °C for Mahanagdong; (iv) 14 ± 10 °C for Alto Peak; (v) 10 ± 7 °C for Palinpinon. The Na–K–Ca geothermometer works well at Mahanagdong and Bacon-Manito and relatively well at Palinpinon and Tongonan. In contrast, its behavior is comparatively poor at Alto Peak, possibly due to the presence of feed zones with different characteristics as pointed out by Reyes et al. (1993). The Na–K–Ca temperatures are generally lower than aquifer temperatures, especially at Alto Peak, and to a lower extent at Mahanagdong and Bacon-Manito, whereas the opposite is true for Palinpinon and Tongonan.

Among the geothermal systems of New Zealand (Fig. 5.17e), the average absolute deviation of the Na–K–Ca temperature from the aquifer temperature is: (i) 5 ± 3 °C for Ngawha; (ii) 15 ± 8 °C for Kawerau; (iii) 22 ± 12 °C for Waiotapu; (iv) 7 ± 5 °C for Mokai; (v) 4 ± 2 °C for Ngatamariki; (vi) 18 ± 12 °C for Broadlands; (vii) 7 ± 4 °C for Wairakei; (viii) 15 ± 8 °C for Rotokawa. The Na–K–Ca geothermometer has a good performance at Ngawha, Mokai, Ngatamariki, and Wairakei, whereas its behavior is poor at Kawerau, Rotokawa, Broadlands, and especially at Waiotapu. The Na–K–Ca temperature overestimates significantly the aquifer temperature in most wells of Broadlands, Kawerau, and Waiotapu, whereas the opposite occurs at Rotokawa.

Among the miscellaneous geothermal systems (Fig. 5.17f), the average absolute deviation of the Na–K–Ca temperature from the aquifer temperature is: (i) 65 ± 15 °C for Yangbajing; (ii) 35 ± 23 °C for Kizildere; (iii) 59 ± 27 °C for Latera; (iv) 33 ± 34 °C for Mofete; (v) 66 ± 6 °C for Ribeira Grande; (vi) 10 ± 5 °C for Tendaho; (vii) 8 ± 5 °C for Asal; (viii) 35 ± 4 °C for Aluto-Langano; (ix) 16 ± 15 °C for Olkaria.

The Na–K–Ca geothermometer works well at Asal, relatively well at Tendaho, but it has a very poor performance at Olkaria, Mofete, Aluto-Langano, Kizildere and especially at Latera, Yangbajing, and Ribeira Grande. The Na–K–Ca temperature overestimates considerably the reservoir temperature at Yangbajing, Ribeira Grande, Kizildere, Latera, Aluto-Langano, and in most wells of Olkaria, whereas the Na–K–Ca temperature underestimates, to different extents, the aquifer temperature at Mofete, Bagnore, Asal and Tendaho.

Loss of Ca from the aqueous solution due to precipitation of calcite or other Ca-bearing minerals is a possible reason explaining why Na–K–Ca temperatures are higher than aquifer temperatures. Although there is no relation between the performance of the Na–K–Ca geothermometer and Ca concentration for the reservoir liquids of interest, loss of Ca is expected to have a much stronger impact on Ca-poor aqueous solutions, such as Na–HCO_3 waters, than on Ca-rich aqueous solutions, such as high-salinity Na–Cl waters. Of course, this problem affects not only the Na–K–Ca geothermometer, but also all the Ca-based geoindicators.

Na–K–Ca temperatures higher than aquifer temperatures could be explained also by the lack of re-equilibration of the Na–K–Ca system upon cooling of the aqueous solutions, owing to the slow kinetics of relevant reactions. This explanation could apply not only to spring waters but also to wells discharges, especially to wells producing from a secondary shallow reservoir, in which the geothermal waters, coming from a deeper and hotter reservoir, have a relatively short residence time. For instance, this could be the case of Yangbajing. However, further data on the kinetics of relevant re-equilibration processes are needed to convert this hypothesis in a convincing explanation.

The deviations of Na–K–Ca temperatures from aquifers temperatures could also be ascribable to the different constraints controlling the activity of Ca^{2+} ion in reservoir liquids, either saturation with calcite, at high f_{CO_2} values, or saturation with a Ca–Al–silicate, at low f_{CO_2} values. Further complications are caused by the possible role of different Ca–Al-silicates, such as laumontite and other zeolites at low-temperatures (indicatively up to 200 °C), epidote, prehnite, and wairakite at temperatures of 200–300 °C, as well as grandite garnet, anorthite, pyroxene, and amphibole, above 300 °C.

Participation of variably-ordered adularias (see Sect. 5.3.4) to the exchange reactions of interest, is another possible reason for the discrepancies between Na–K–Ca temperatures and aquifer temperatures. Finally, poor knowledge or choice of the aquifer temperature cannot be excluded, although it cannot be invoked for deviations higher than a few degrees to 10 °C approximately.

5.4.3 Na–Ca and K–Ca Geothermometers

As shown by Tonani (1980), the Na–K–Ca geothermometer can be split into three temperature functions involving the Na/K, $\sqrt{Ca}/Na$, and $\sqrt{Ca}/K$ ratios. The use of three separate geothermometric functions instead of the single Na–K–Ca geothermometer is advantageous because it is possible to check if the three computed temperatures are consistent with each other or not, although only two of these three relations are mutually independent (Tonani 1980). Also Arnórsson et al. (1983a) underscored that the separate Na/K and $\sqrt{\mathrm{Ca}}/\mathrm{Na}$ cation ratios composing the Na–K–Ca geothermometer are fixed by temperature alone, if the condition of overall chemical equilibrium between the geothermal waters and the hydrothermal mineral assemblage is attained.

Based on these findings and considering that there is an infinite number of Na–K geothermometers (see 5.3), it is permissible to suppose that there is also an infinite number of Na–Ca and K–Ca geothermometers. To avoid complicating too much the following discussion, we decided to take into account the sixteen empirical Na–K geothermometers with linear dependence on the absolute temperature inverse listed in Table 5.2 only. Moreover, we decided to write the geothermometric relations we are looking for in terms of the $\mathrm{Na}^2/\mathrm{Ca}$ and K^2/Ca ratios instead of the $\sqrt{\mathrm{Ca}}/\mathrm{Na}$ and $\sqrt{\mathrm{Ca}}/\mathrm{K}$ ratios, respectively. To obtain the Na–Ca and K–Ca geothermometers of interest, first, β is assumed equal to 1/3 (consistent with T > 100 °C) and Eq. (5.80) is rewritten as (concentrations in mg/kg):

$$\log(\mathrm{c_{Na}}/\mathrm{c_K}) + 1/3 \cdot \log(\sqrt{\mathrm{c_{Ca}}}/\mathrm{c_{Na}}) = \frac{1647}{\mathrm{T} + 273.15} - 3.1567. \tag{5.86}$$

Second, Eq. (5.86) is multiplied by 2 and is suitably rearranged obtaining:

$$\log(\mathrm{c_{Na}^2}/\mathrm{c_{Ca}}) = 6 \cdot \log(\mathrm{c_{Na}}/\mathrm{c_K}) - \frac{9882}{\mathrm{T} + 273.15} + 18.9402. \tag{5.87}$$

Third, each Na–K empirical geothermometer listed in Table 5.2 is alternatively inserted into Eq. (5.87) and the relation is suitably reorganized, deriving the corresponding Na–Ca function. The related K–Ca geothermometer is then obtained either subtracting the Na–K relation multiplied by 2 from the Na–Ca equation:

$$\log(\mathrm{c_K^2}/\mathrm{c_{Ca}}) = \log(\mathrm{c_{Na}^2}/\mathrm{c_{Ca}}) - 2 \cdot \log(\mathrm{c_{Na}}/\mathrm{c_K}) \tag{5.88}$$

or through the relation:

$$\log(\mathrm{c_K^2}/\mathrm{c_{Ca}}) = 4 \cdot \log(\mathrm{c_{Na}}/\mathrm{c_K}) - \frac{9882}{\mathrm{T} + 273.15} + 18.9402. \tag{5.89}$$

The results of these simple but tedious calculations are listed in Tables 5.3 and 5.4, where two relations are given, one for molal concentrations, the other for concentrations in mg/kg, although the conversion from one form to the other is straightforward. These Na–Ca and K–Ca geothermometers are expected to work at comparatively low $f_{\mathrm{CO_2}}$ values stabilizing one of the several possible Ca–Al-silicates (see above) and destabilizing calcite.

Table 5.3 Na–Ca functions obtained from the Na–K–Ca geothermometer and the sixteen empirical Na–K geothermometers

References	Na–Ca function (molal concentrations)	Na–Ca function (concentrations in mg/kg)	Code	Eqn. #
White (1968)	$T = \frac{6857.4}{13.793 - \log\left(\frac{m_{Na}^2}{m_{Ca}}\right)} - 273.15$	$T = \frac{6857.4}{17.913 - \log\left(\frac{c_{Na}^2}{c_{Ca}}\right)} - 273.15$	Wh68	(5.90)
Ellis (1970)	$T = \frac{5073}{10.308 - \log\left(\frac{m_{Na}^2}{m_{Ca}}\right)} - 273.15$	$T = \frac{5073}{14.428 - \log\left(\frac{c_{Na}^2}{c_{Ca}}\right)} - 273.15$	El70	(5.91)
Mercado (1970)	$T = \frac{6039}{11.990 - \log\left(\frac{m_{Na}^2}{m_{Ca}}\right)} - 273.15$	$T = \frac{6039}{16.110 - \log\left(\frac{c_{Na}^2}{c_{Ca}}\right)} - 273.15$	Me70	(5.92)
Fournier and Truesdell (1973)	$T = \frac{5220}{10.620 - \log\left(\frac{m_{Na}^2}{m_{Ca}}\right)} - 273.15$	$T = \frac{5220}{14.740 - \log\left(\frac{c_{Na}^2}{c_{Ca}}\right)} - 273.15$	FoTr73	(5.93)
Truesdell (1976)	$T = \frac{4748.4}{9.676 - \log\left(\frac{m_{Na}^2}{m_{Ca}}\right)} - 273.15$	$T = \frac{4748.4}{13.796 - \log\left(\frac{c_{Na}^2}{c_{Ca}}\right)} - 273.15$	Tr76	(5.94)
Fournier (1979)	$T = \frac{2580}{5.922 - \log\left(\frac{m_{Na}^2}{m_{Ca}}\right)} - 273.15$	$T = \frac{2580}{10.042 - \log\left(\frac{c_{Na}^2}{c_{Ca}}\right)} - 273.15$	Fo79	(5.95)
Tonani (1980)	$T = \frac{4884}{10.140 - \log\left(\frac{m_{Na}^2}{m_{Ca}}\right)} - 273.15$	$T = \frac{4884}{14.260 - \log\left(\frac{c_{Na}^2}{c_{Ca}}\right)} - 273.15$	To80	(5.96)
Arnórsson et al. (1983a), 25–250°C	$T = \frac{4284}{8.862 - \log\left(\frac{m_{Na}^2}{m_{Ca}}\right)} - 273.15$	$T = \frac{4284}{12.982 - \log\left(\frac{c_{Na}^2}{c_{Ca}}\right)} - 273.15$	Ar83, LT	(5.97)
Arnórsson et al. (1983a), 250–350°C	$T = \frac{1968}{4.626 - \log\left(\frac{m_{Na}^2}{m_{Ca}}\right)} - 273.15$	$T = \frac{1968}{8.746 - \log\left(\frac{c_{Na}^2}{c_{Ca}}\right)} - 273.15$	Ar83, HT	(5.98)

(continued)

Table 5.3 (continued)

References	Na–Ca function (molal concentrations)	Na–Ca function (concentrations in mg/kg)	Code	Eqn. #
Giggenbach (1988)	$T = \frac{1542}{4.320 - \log\left(\frac{m_{Na}^2}{m_{Ca}}\right)} - 273.15$	$T = \frac{1542}{8.440 - \log\left(\frac{c_{Na}^2}{c_{Ca}}\right)} - 273.15$	Gi88	(5.99)
Nieva and Nieva (1987)	$T = \frac{2814}{6.000 - \log\left(\frac{m_{Na}^2}{m_{Ca}}\right)} - 273.15$	$T = \frac{2814}{10.120 - \log\left(\frac{c_{Na}^2}{c_{Ca}}\right)} - 273.15$	NiNi87	(5.100)
Kharaka and Mariner (1989)	$T = \frac{2802}{6.960 - \log\left(\frac{m_{Na}^2}{m_{Ca}}\right)} - 273.15$	$T = \frac{2802}{11.080 - \log\left(\frac{c_{Na}^2}{c_{Ca}}\right)} - 273.15$	KhMa89	(5.101)
Michard (1990)	$T = \frac{2862}{4.920 - \log\left(\frac{m_{Na}^2}{m_{Ca}}\right)} - 273.15$	$T = \frac{2862}{9.040 - \log\left(\frac{c_{Na}^2}{c_{Ca}}\right)} - 273.15$	Mi90a	(5.102)
Verma and Santoyo (1997)	$T = \frac{2148}{5.130 - \log\left(\frac{m_{Na}^2}{m_{Ca}}\right)} - 273.15$	$T = \frac{2148}{9.250 - \log\left(\frac{c_{Na}^2}{c_{Ca}}\right)} - 273.15$	VeSa97	(5.103)
Santoyo and Díaz-González (2010)	$T = \frac{4624.2}{9.555 - \log\left(\frac{m_{Na}^2}{m_{Ca}}\right)} - 273.15$	$T = \frac{4624.2}{13.675 - \log\left(\frac{c_{Na}^2}{c_{Ca}}\right)} - 273.15$	SaDi10	(5.104)
Simmons (2013)	$T = \frac{7992}{16.238 - \log\left(\frac{c_{Na}^2}{c_{Ca}}\right)} - 273.15$	$T = \frac{7992}{20.359 - \log\left(\frac{c_{Na}^2}{c_{Ca}}\right)} - 273.15$	Si13	(5.105)

Table 5.4 K–Ca functions obtained from the Na–K–Ca geothermometer and the sixteen empirical Na–K geothermometers

References	K–Ca function (molal concentrations)	K–Ca function (concentrations in mg/kg)	Code	Eqn. #
White (1968)	$\mathrm{T} = \frac{7865.6}{13.674 - \log\left(\frac{m_{\mathrm{K}}^2}{m_{\mathrm{Ca}}}\right)} - 273.15$	$\mathrm{T} = \frac{7865.6}{18.255 - \log\left(\frac{c_{\mathrm{K}}^2}{c_{\mathrm{Ca}}}\right)} - 273.15$	Wh68	(5.106)
Ellis (1970)	$\mathrm{T} = \frac{6676}{11.351 - \log\left(\frac{m_{\mathrm{K}}^2}{m_{\mathrm{Ca}}}\right)} - 273.15$	$\mathrm{T} = \frac{6676}{15.932 - \log\left(\frac{c_{\mathrm{K}}^2}{c_{\mathrm{Ca}}}\right)} - 273.15$	El70	(5.107)
Mercado (1970)	$\mathrm{T} = \frac{7320}{12.472 - \log\left(\frac{m_{\mathrm{K}}^2}{m_{\mathrm{Ca}}}\right)} - 273.15$	$\mathrm{T} = \frac{7320}{17.053 - \log\left(\frac{c_{\mathrm{K}}^2}{c_{\mathrm{Ca}}}\right)} - 273.15$	Me70	(5.108)
Fournier and Truesdell (1973)	$\mathrm{T} = \frac{6774}{11.559 - \log\left(\frac{m_{\mathrm{K}}^2}{m_{\mathrm{Ca}}}\right)} - 273.15$	$\mathrm{T} = \frac{6774}{16.140 - \log\left(\frac{c_{\mathrm{K}}^2}{c_{\mathrm{Ca}}}\right)} - 273.15$	FoTr73	(5.109)
Truesdell (1976)	$\mathrm{T} = \frac{6459.6}{10.930 - \log\left(\frac{m_{\mathrm{K}}^2}{m_{\mathrm{Ca}}}\right)} - 273.15$	$\mathrm{T} = \frac{6459.6}{15.511 - \log\left(\frac{c_{\mathrm{K}}^2}{c_{\mathrm{Ca}}}\right)} - 273.15$	Tr76	(5.110)
Fournier (1979)	$\mathrm{T} = \frac{5014}{8.427 - \log\left(\frac{m_{\mathrm{K}}^2}{m_{\mathrm{Ca}}}\right)} - 273.15$	$\mathrm{T} = \frac{5014}{13.008 - \log\left(\frac{c_{\mathrm{K}}^2}{c_{\mathrm{Ca}}}\right)} - 273.15$	Fo79	(5.111)
Tonani (1980)	$\mathrm{T} = \frac{6550}{11.239 - \log\left(\frac{m_{\mathrm{K}}^2}{m_{\mathrm{Ca}}}\right)} - 273.15$	$\mathrm{T} = \frac{6550}{15.820 - \log\left(\frac{c_{\mathrm{K}}^2}{c_{\mathrm{Ca}}}\right)} - 273.15$	To80	(5.112)
Arnórsson et al. (1983a), 25–250 °C	$\mathrm{T} = \frac{6150}{10.387 - \log\left(\frac{m_{\mathrm{K}}^2}{m_{\mathrm{Ca}}}\right)} - 273.15$	$\mathrm{T} = \frac{6150}{14.968 - \log\left(\frac{c_{\mathrm{K}}^2}{c_{\mathrm{Ca}}}\right)} - 273.15$	Ar83, LT	(5.113)
Arnórsson et al. (1983a), 250–350 °C	$\mathrm{T} = \frac{4606}{7.563 - \log\left(\frac{m_{\mathrm{K}}^2}{m_{\mathrm{Ca}}}\right)} - 273.15$	$\mathrm{T} = \frac{4606}{12.144 - \log\left(\frac{c_{\mathrm{K}}^2}{c_{\mathrm{Ca}}}\right)} - 273.15$	Ar83, HT	(5.114)

(continued)

Table 5.4 (continued)

References	K–Ca function (molal concentrations)	K–Ca function (concentrations in mg/kg)	Code	Eqn. #
Giggenbach (1988)	$\mathrm{T} = \frac{4322}{7.359 - \log\left(\frac{m_{\mathrm{K}}^2}{m_{\mathrm{Ca}}}\right)} - 273.15$	$\mathrm{T} = \frac{4322}{11.940 - \log\left(\frac{c_{\mathrm{K}}^2}{c_{\mathrm{Ca}}}\right)} - 273.15$	Gi88	(5.115)
Nieva and Nieva (1987)	$\mathrm{T} = \frac{5170}{8.479 - \log\left(\frac{m_{\mathrm{K}}^2}{m_{\mathrm{Ca}}}\right)} - 273.15$	$\mathrm{T} = \frac{5170}{13.060 - \log\left(\frac{c_{\mathrm{K}}^2}{c_{\mathrm{Ca}}}\right)} - 273.15$	NiNi87	(5.116)
Kharaka and Mariner (1989)	$\mathrm{T} = \frac{5162}{9.119 - \log\left(\frac{m_{\mathrm{K}}^2}{m_{\mathrm{Ca}}}\right)} - 273.15$	$\mathrm{T} = \frac{5162}{13.700 - \log\left(\frac{c_{\mathrm{K}}^2}{c_{\mathrm{Ca}}}\right)} - 273.15$	KhMa89	(5.117)
Michard (1990)	$\mathrm{T} = \frac{5202}{7.759 - \log\left(\frac{m_{\mathrm{K}}^2}{m_{\mathrm{Ca}}}\right)} - 273.15$	$\mathrm{T} = \frac{5202}{12.340 - \log\left(\frac{c_{\mathrm{K}}^2}{c_{\mathrm{Ca}}}\right)} - 273.15$	Mi90a	(5.118)
Verma and Santoyo (1997)	$\mathrm{T} = \frac{4726}{7.899 - \log\left(\frac{m_{\mathrm{K}}^2}{m_{\mathrm{Ca}}}\right)} - 273.15$	$\mathrm{T} = \frac{4726}{12.480 - \log\left(\frac{c_{\mathrm{K}}^2}{c_{\mathrm{Ca}}}\right)} - 273.15$	VeSa97	(5.119)
Santoyo and Díaz-González (2010)	$\mathrm{T} = \frac{6376.8}{10.849 - \log\left(\frac{m_{\mathrm{K}}^2}{m_{\mathrm{Ca}}}\right)} - 273.15$	$\mathrm{T} = \frac{6376.8}{15.430 - \log\left(\frac{c_{\mathrm{K}}^2}{c_{\mathrm{Ca}}}\right)} - 273.15$	SaDi10	(5.120)
Simmons (2013)	$\mathrm{T} = \frac{8622}{15.304 - \log\left(\frac{m_{\mathrm{K}}^2}{m_{\mathrm{Ca}}}\right)} - 273.15$	$\mathrm{T} = \frac{8622}{19.886 - \log\left(\frac{c_{\mathrm{K}}^2}{c_{\mathrm{Ca}}}\right)} - 273.15$	Si13	(5.121)

In addition to the Na–Ca and K–Ca geothermometers derived from the Na–K–Ca geothermometer and the sixteen empirical Na–K geothermometers listed in Table 5.2, it is necessary to take into account the Na–Ca geothermometer of Arnórsson et al. (1983a) and the K–Ca geothermometer of Michard (1990), which were proposed as such.

Arnórsson et al. (1983a) presented a diagram of $\log(\sqrt{\mathrm{Ca}}/\mathrm{Na})$ versus the absolute temperature inverse, in which there is a large scatter of data points that was attributed to equilibrium with more than one mineral assemblage.

The $\sqrt{\mathrm{Ca}}/\mathrm{Na}$ geothermometric function of Arnórsson et al. (1983a) has a linear dependence on the absolute temperature inverse and corresponds to the following two relations identified by code Ar83b in Fig. 5.18:

$$\mathrm{T} = \frac{1120}{2.118 - \log\left(m_{\mathrm{Na}}^{2} \big/ m_{\mathrm{Ca}}\right)} - 273.15 \quad \mathrm{T} = \frac{1120}{6.238 - \log\left(\mathrm{c}_{\mathrm{Na}}^{2} \big/ \mathrm{c}_{\mathrm{Ca}}\right)} - 273.15. \tag{5.122}$$

The two associated K–Ca geothermometric functions can be computed by inserting the Na–Ca geothermometer defined by Eq. (5.122) and one of the two Na–K geothermometers of Arnórsson et al. (1983a), that is Eqs. (5.64) or (5.65), into Eq. (5.88). The K–Ca geothermometers thus obtained, identified by code Ar83b

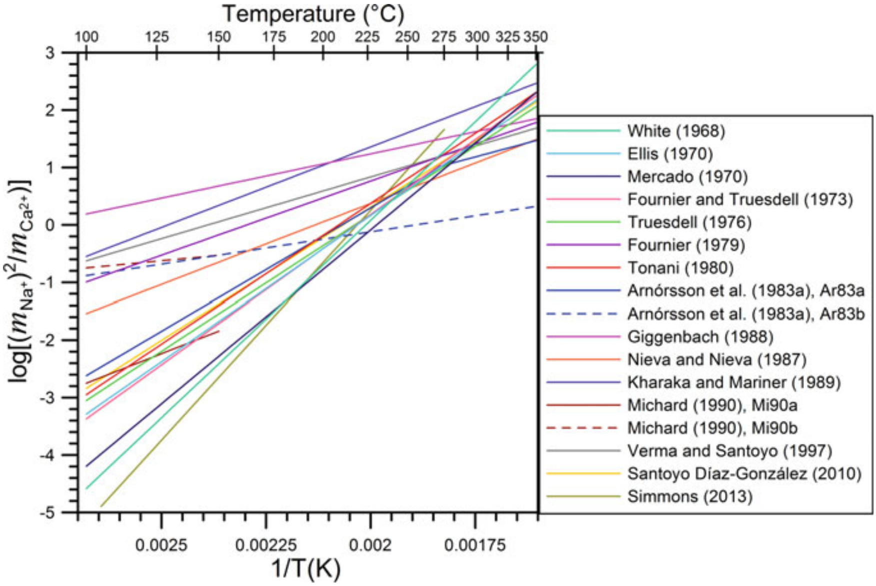

Fig. 5.18 Diagram of $\log(m_{\mathrm{Na}}^{2}/m_{\mathrm{Ca}})$ versus the absolute temperature inverse showing the sixteen Na–Ca geothermometers obtained from the sixteen empirical Na–K functions (see legend) and the Na–K–Ca geothermometer, as well as the Na–Ca geothermometers of Arnórsson et al. (1983a) and Michard (1990), indicated by codes Ar83b and Mi90b, respectively

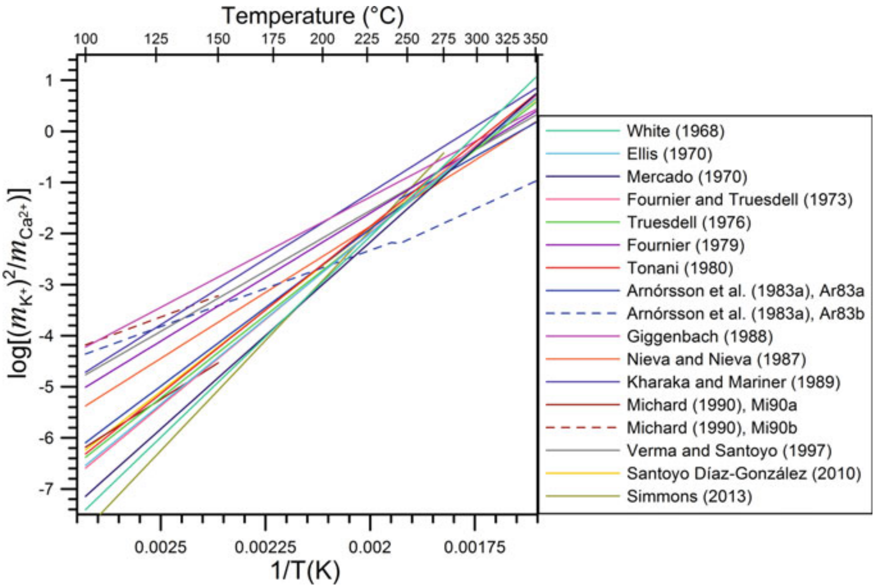

Fig. 5.19 Diagram of $\log(m_{\mathrm{K}}^2/m_{\mathrm{Ca}})$ versus the reciprocal of the absolute temperature showing the sixteen K–Ca geothermometers obtained from the sixteen empirical Na–K functions (see legend) and the Na–K–Ca geothermometer, as well as the K–Ca geothermometers of Arnórsson et al. (1983a) and Michard (1990), indicated by codes Ar83b and Mi90b, respectively

in Fig. 5.19, are:

$$\mathrm{T} = \frac{2986}{3.643 - \log(\mathrm{m}_{\mathrm{K}}^2/m_{\mathrm{Ca}})} - 273.15 \quad \mathrm{T} = \frac{2986}{8.224 - \log(\mathrm{c}_{\mathrm{K}}^2/\mathrm{c}_{\mathrm{Ca}})} - 273.15 \tag{5.123}$$

$$\mathrm{T} = \frac{3758}{5.055 - \log(m_{\mathrm{K}}^2/m_{\mathrm{Ca}})} - 273.15 \quad \mathrm{T} = \frac{3758}{9.636 - \log(\mathrm{c}_{\mathrm{K}}^2/\mathrm{c}_{\mathrm{Ca}})} - 273.15. \tag{5.124}$$

Equation (5.123) is valid from 25 to 250 °C, whereas Eq. (5.124) applies in the temperature range 250–350 °C.

Based on the chemistry of several thermal waters interacting with granitic rocks at temperatures lower than 150 °C, Michard (1990) derived a K–Ca geothermometer, corresponding to the following two equations identified by code Mi90a in Fig. 5.19:

$$\mathrm{T} = \frac{3030}{3.94 - \log(m_{\mathrm{K}}^2/m_{\mathrm{Ca}})} - 273.15 \quad \mathrm{T} = \frac{3030}{8.52 - \log(\mathrm{c}_{\mathrm{K}}^2/\mathrm{c}_{\mathrm{Ca}})} - 273.15. \tag{5.125}$$

The related Na–Ca geothermometer can be obtained inserting the K–Ca and Na–K geothermometers of Michard (1990) defined by Eqs. (5.125) and (5.69), respectively, into Eq. (5.88). The Na–Ca geothermometer thus derived is expressed by the following two relations (identified by code Mi90a in Fig. 5.18):

$$\mathrm{T} = \frac{690}{1.10 - \log\left(m_{\mathrm{Na}}^{2} \big/ m_{\mathrm{Ca}}\right)} - 273.15 \quad \mathrm{T} = \frac{690}{5.22 - \log\left(\mathrm{c}_{\mathrm{Na}}^{2} \big/ \mathrm{c}_{\mathrm{Ca}}\right)} - 273.15. \tag{5.126}$$

Equations (5.125) and (5.126) should not be used above 150 °C, because their parent functions were calibrated below this threshold.

The plot of $\log(m_{\mathrm{Na}}^2/m_{\mathrm{Ca}})$ versus the absolute temperature inverse of Fig. 5.18 shows that there are large differences among the Na–Ca geothermometric functions discussed above, with most of them converging at temperatures higher than ~250 °C, apart from Eq. (5.102) from Michard (1990) and Eq. (5.122) from Arnórsson et al. (1983a), but diverging progressively with decreasing temperature. Since each pair of Na–Ca and Na–K functions is linked by Eq. (5.87), this graph reflects largely the shape of Fig. 5.14 with the Na–Ca geothermometers of relatively low slope corresponding to the Na–K geothermometers of comparatively high slope (e.g., Giggenbach 1988) and vice versa (e.g., Simmons 2013).

The diagram of $\log(m_{\mathrm{K}}^2/m_{\mathrm{Ca}})$ versus the absolute temperature reciprocal of Fig. 5.19 is similar to those of Figs. 5.14 and 5.18. To be noted that all the K–Ca geothermometers have slope higher than the corresponding Na–Ca geothermometers and, again, the K–Ca geothermometers of comparatively small slope correspond to the Na–K geothermometers of relatively large slope (e.g., Giggenbach 1988) and vice versa (e.g., Simmons 2013), since each couple of K–Ca and Na–K functions is connected by Eq. (5.89).

In the correlation diagrams of $\log(m_{\mathrm{Na}}^2/m_{\mathrm{Ca}})$ versus the absolute temperature inverse (Fig. 5.20) and of $\log(m_{\mathrm{K}}^2/m_{\mathrm{Ca}})$ versus the absolute temperature reciprocal (Fig. 5.21), most of the 1013 selected reservoir liquids are positioned within the same area occupied by the empirical Na–Ca and K–Ca functions, respectively. Not surprisingly, a similar distribution of data points was already noted by Fournier and Truesdell (1973) in the diagrams of log ($\sqrt{\mathrm{Ca}}/\mathrm{Na}$) versus the absolute temperature reciprocal and log ($\sqrt{\mathrm{Ca}}/\mathrm{K}$) versus the absolute temperature inverse.

Nevertheless, all or most reservoir liquids of Long Valley, Mori-Nigorikawa, Yangbajing, Kizildere, Ribeira Grande, Latera, and Aluto-Langano, as well as some reservoir liquids of Broadlands, Ngawha, and Olkaria are situated above the lines defined by the K–Ca geothermometers in Fig. 5.21 and most of these samples are positioned above the lines corresponding to the Na–Ca geothermometers in Fig. 5.20. These reservoir liquids have Na–K–Ca temperature significantly higher than aquifer temperature as discussed in Sect. 5.4.2 and shown by the diagrams of Fig. 5.17.

Again, these high $\mathrm{Na}^2/\mathrm{Ca}$ and K^2/Ca log-ratios might be due to either precipitation of a Ca-bearing solid phase (typically calcite) or equilibration of the aqueous solutions

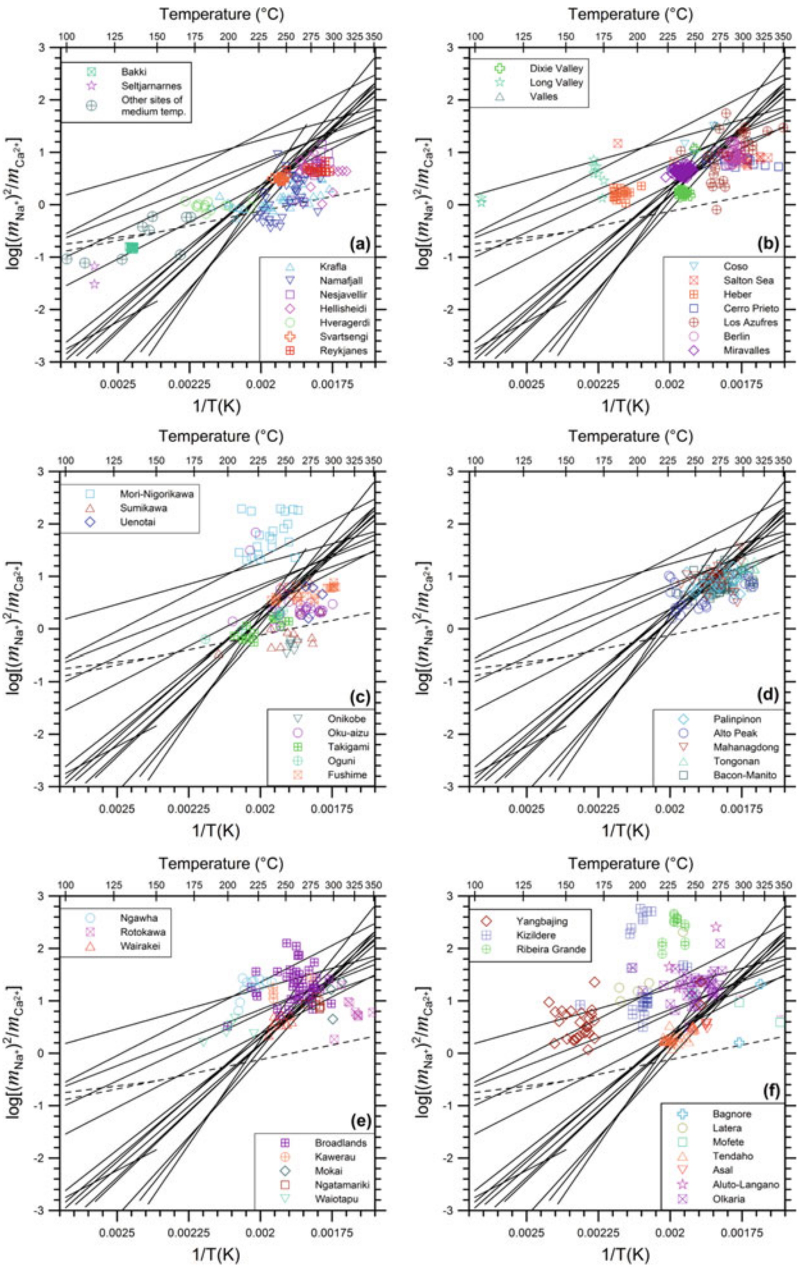

Fig. 5.20 Diagrams of $\log(m_{\mathrm{Na}}^2/m_{\mathrm{Ca}})$ versus the absolute temperature inverse showing the selected reservoir liquids from **a** Iceland, **b** Northern-Central America, **c** Japan, **d** The Philippines, **e** New Zealand, and **f** miscellaneous geothermal system, the sixteen Na–Ca geothermometers obtained from the sixteen empirical Na–K functions (see legend) and the Na–K–Ca geothermometer (solid black lines), as well as the Na–Ca functions of Arnórsson et al. (1983a) and Michard (1990), represented by dashed black lines

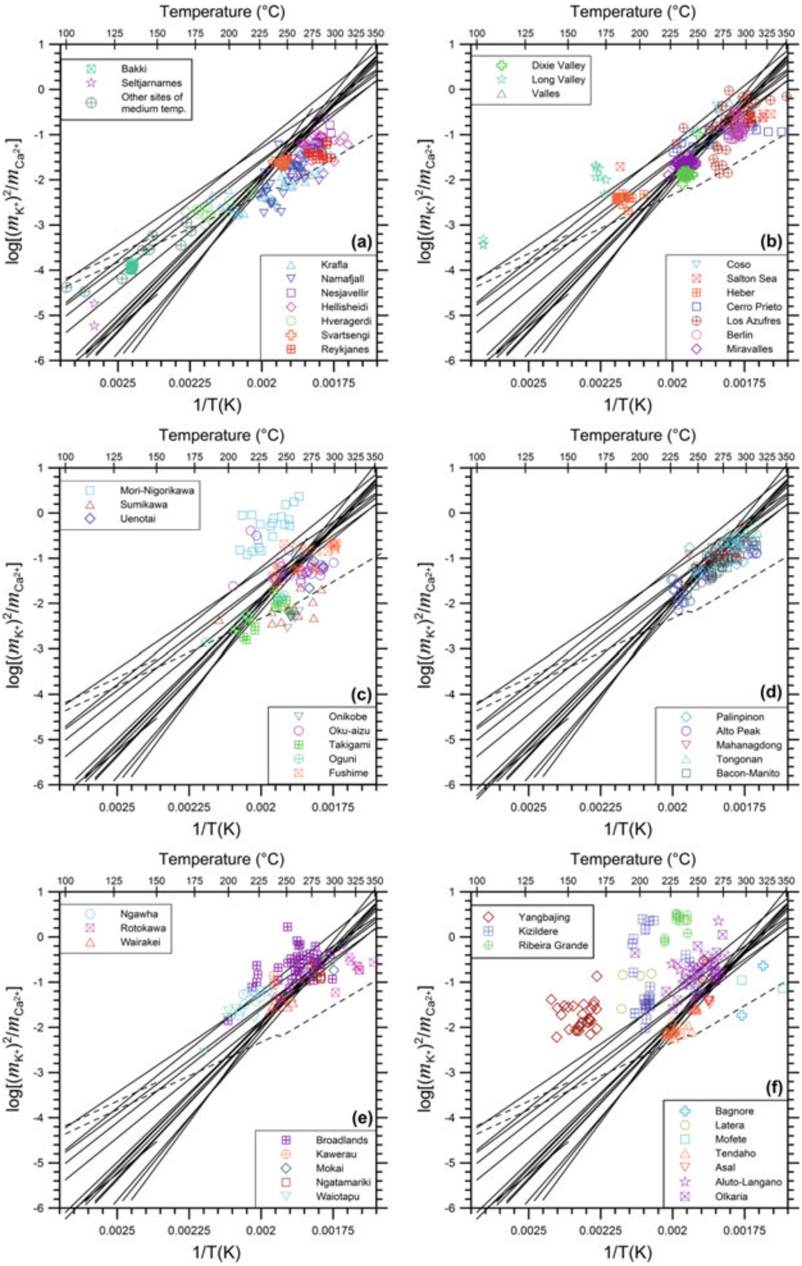

Fig. 5.21 Diagrams of $\log(m_{\mathrm{K}}^2/m_{\mathrm{Ca}})$ versus the absolute temperature inverse showing the selected reservoir liquids from **a** Iceland, **b** Northern-Central America, **c** Japan, **d** The Philippines, **e** New Zealand, and **f** miscellaneous geothermal, the sixteen K–Ca geothermometers obtained from the sixteen empirical Na–K functions (see legend) and the Na–K–Ca geothermometer (solid black lines), as well as the K-Ca functions of Arnórsson et al. (1983a) and Michard (1990), represented by dashed black lines

with calcite instead of one of the several possible Ca–Al-silicates, because of the relatively high f_{CO_2} values occurring in the geothermal reservoirs of provenance.

The Na^2/Ca and K^2/Ca log-ratios of the other reservoir liquids agree with those fixed by the Na–Ca and K–Ca geothermometers and, therefore, are probably controlled by equilibrium with one of the different Ca–Al-silicate minerals, because of the comparatively low f_{CO_2} values occurring in the related geothermal aquifers. These findings imply that the different Na–Ca and K–Ca geothermometric functions can be utilized, to some extent, to identify the governing Ca–Al-silicate minerals, as discussed in the next section.

5.4.4 *The Hydrothermal Minerals Controlling the Na–Ca and K–Ca Geothermometers*

Following the same approach adopted in Sect. 5.3.3 for the Na–K geothermometer, the $\Delta H°_r$ and $\Delta S°_r$ values of the empirical Na–Ca and K–Ca geothermometers, calculated from their slope and intercept using Eqs. (5.13) and (5.14), are compared with the standard enthalpies and entropies of the following Na–Ca exchange reactions:

$$2NaAlSi_3O_8 + 4H_2O + Ca^{2+} = CaAl_2Si_4O_{12} \cdot 4H_2O + 2SiO_2 + 2Na^+ \quad (5.127)$$

$$\begin{aligned}&2NaAlSi_3O_8 + 0.25KAlSi_3O_8 + 0.5H_2O + Ca^{2+}\\&\quad = 0.25KAl_3Si_3O_{10}(OH)_2 + 0.5Ca_2Al_3Si_3O_{12}(OH) + 4.5SiO_2 + 2Na^+\end{aligned} \quad (5.128)$$

$$\begin{aligned}&2\,NaAlSi_3O_8 + 0.5\,KAlSi_3O_8 + H_2O + Ca^{2+}\\&\quad = 0.5KAl_3Si_3O_{10}(OH)_2 + 0.5Ca_2Al_2Si_3O_{10}(OH)_2 + 4.5SiO_2 + 2Na^+\end{aligned} \quad (5.129)$$

$$2NaAlSi_3O_8 + 2H_2O + Ca^{2+} = CaAl_2Si_4O_{12} \cdot 2\,H_2O + 2SiO_2 + 2Na^+ \quad (5.130)$$

and of the following K–Ca exchange reactions:

$$2\,KAlSi_3O_8 + 4\,H_2O + Ca^{2+} = CaAl_2Si_4O_{12} \cdot 4\,H_2O + 2\,SiO_2 + 2\,K^+ \quad (5.131)$$

$$\begin{aligned}&2.25\,KAlSi_3O_8 + 0.5\,H_2O + Ca^{2+}\\&\quad = 0.25\,KAl_3Si_3O_{10}(OH)_2 + 0.5\,Ca_2Al_3Si_3O_{12}(OH) + 4.5\,SiO_2 + 2\,K^+\end{aligned} \quad (5.132)$$

$$\begin{aligned}&2.5\,KAlSi_3O_8 + H_2O + Ca^{2+}\\&\quad = 0.5\,KAl_3Si_3O_{10}(OH)_2 + 0.5\,Ca_2Al_2Si_3O_{10}(OH)_2 + 4.5\,SiO_2 + 2\,K^+\end{aligned} \quad (5.133)$$

$$2\,\mathrm{KAlSi_3O_8} + 2\,\mathrm{H_2O} + \mathrm{Ca^{2+}} = \mathrm{CaAl_2Si_4O_{12}} \cdot 2\,\mathrm{H_2O} + 2\mathrm{SiO_2} + 2\,\mathrm{K^+} \quad (5.134)$$

respectively. Laumontite [$CaAl_2Si_4O_{12} \cdot 4\ H_2O$] is involved in reactions (5.127) and (5.131), clinozoisite [$Ca_2Al_3Si_3O_{12}(OH)$] participates to reactions (5.128) and (5.132), prehnite [$Ca_2Al_2Si_3O_{10}(OH)_2$] takes part to reactions (5.129) and (5.133) and wairakite [$CaAl_2Si_4O_{12} \cdot 2\ H_2O$] plays a part in reactions (5.130) and (5.134). Among the other minerals involved in the Na–Ca and K–Ca exchange reactions of interest, maximum-microcline and high-sanidine were alternatively considered to represent K-feldspar, whereas the silica mineral was assumed to be quartz/chalcedony above 175 °C and chalcedony below 175 °C. The thermodynamic properties of these reactions were computed as a function of temperature at water saturation pressures using SUPCRT92.

The correlation diagram of Fig. 5.22 shows that the $\Delta H°_r$ and $\Delta S°_r$ values of most Na–Ca geothermometers are consistent with the standard enthalpies and entropies of the Na–Ca exchange reactions of interest computed using SUPCRT92. Only the Na–Ca functions derived from the Na–K geothermometers of White (1968), Mercado

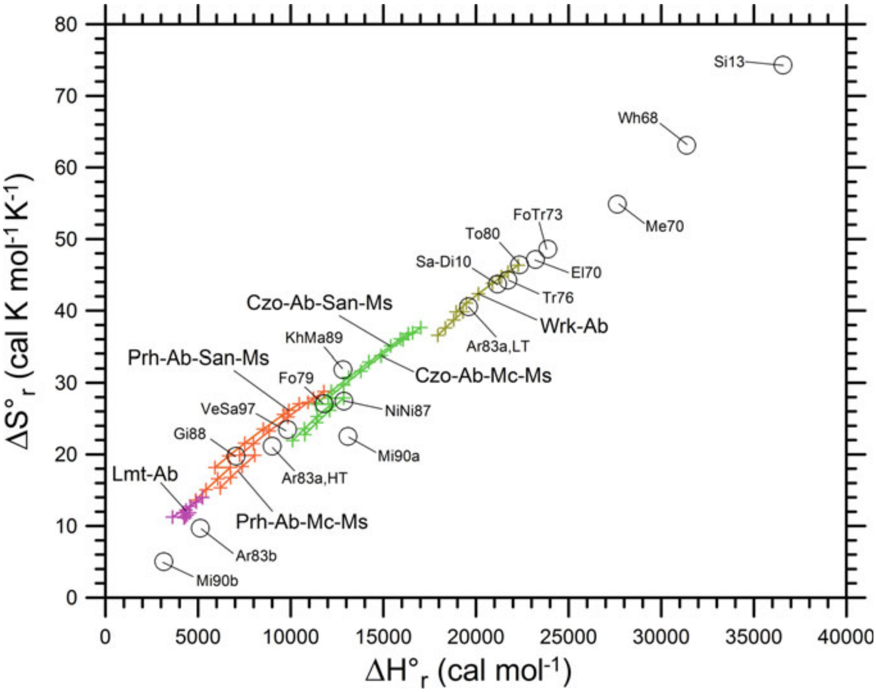

Fig. 5.22 Comparison of the temperature-independent $\Delta H°_r$ and $\Delta S°_r$ values of the empirical Na–Ca geothermometers (open black circles) with those of the Na–Ca exchange reactions involving laumontite (Lmt) or prehnite (Prh) or clinozoisite (Czo) or wairakite (Wrk), and other pertinent minerals, computed as a function of temperature at water saturation pressures using SUPCRT92

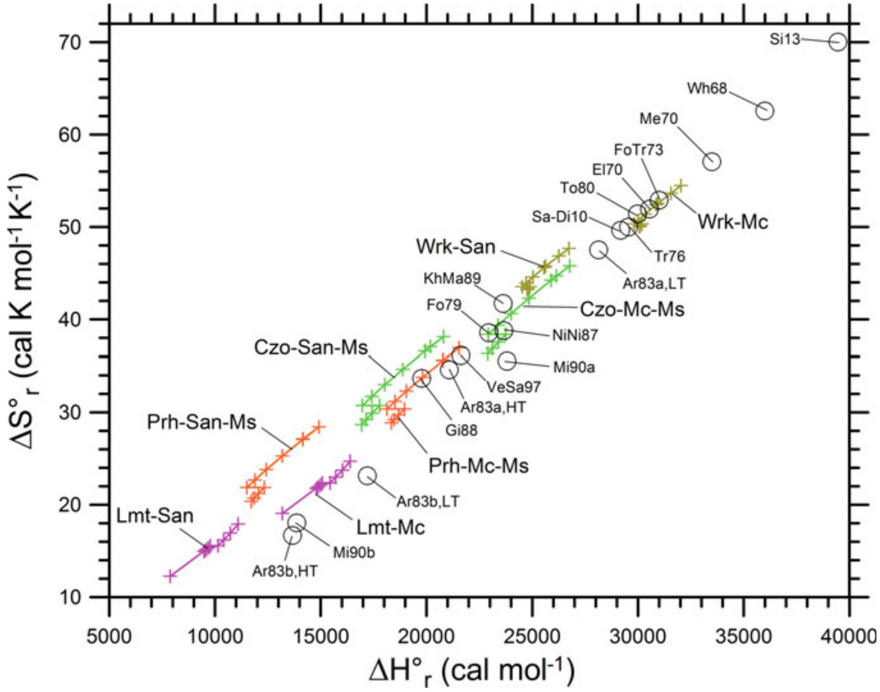

Fig. 5.23 Comparison of the temperature-independent ΔH°_r and ΔS°_r values of the empirical K–Ca geothermometers (open black circles) with those of the K–Ca exchange reactions involving laumontite (Lmt) or prehnite (Prh) or clinozoisite (Czo) or wairakite (Wrk), and other pertinent minerals, computed as a function of temperature at water saturation pressures using SUPCRT92

(1970), and Simmons (2013) have ΔH°_r and ΔS°_r values at variance with the standard enthalpies and entropies of the considered Na–Ca exchange reactions. Similar inferences can be drawn from the correlation diagram of Fig. 5.23, in which the temperature-independent standard enthalpies and entropies of the empirical K–Ca geothermometers, obtained from their slope and intercept, are contrasted with the ΔH°_r and ΔS°_r values of the K–Ca exchange reactions of interest, calculated as a function of temperature at water saturation pressures using SUPCRT92.

These findings have two implications. On the one hand, the Na–Ca and K–Ca geothermometers provide temperatures presumably controlled by the equilibrium condition between the aqueous solution of interest and a given Ca–Al-silicate, assuming that f_{CO_2} is low enough. However, it is impossible to identify the Ca–Al-silicate involved in the Na–Ca and K–Ca exchange reactions presumably controlling the Na–Ca and K–Ca geothermometers owing to their empirical nature, intrinsic and/or inherited from the parent functions, i.e., the Na–K–Ca geothermometer and a given Na–K geothermometer. On the other hand, it should be possible to calibrate theoretical Na–Ca and K–Ca geothermometers based on the exchange reactions considered in this section. This possibility will be explored in Chap. 8.

5.4.5 *Conclusive Remarks on the Na–K–Ca Geothermometer*

Summing up, the Na–Ca and K–Ca geothermometers obtained by splitting the Na–K–Ca function of Fournier and Truesdell (1973) as well as the Na–Ca geothermometer of Arnórsson et al. (1983a) and the K–Ca geothermometer of Michard (1990) work under favorable conditions, that is for waters presumably equilibrated with an unspecified Ca–Al-silicate at relatively low f_{CO_2} values. In contrast, these Na–Ca and K–Ca geothermometers do not work for waters equilibrated with calcite under comparatively high f_{CO_2} values. This implies that the Na^2/Ca and K^2/Ca ratios represent the basis not only for geothermometers but also for f_{CO_2}-indicators. Our view on this point is somewhat different from that of previous authors which is briefly summarized below.

Ellis (1970) pointed out that Ca is a potential CO_2-indicator for thermal waters, proposing a technique to evaluate deep f_{CO_2} values on the basis of Na and Ca concentrations.

As already noted in Sect. 5.4.1, Fournier and Truesdell (1973) recognized that calcite saturation controls Ca concentration, but they did not consider calcite and CO_2 in reactions (5.78) and (5.79), that were assumed to control the Na–K–Ca geothermometer by these authors.

Giggenbach (1988) summarized the results of several investigations which were carried out for providing both theoretical and experimental justifications to the Na–K–Ca geothermometer. He concluded that many problems in the use of this technique are connected with its sensitivity to differences in the CO_2 contents of geothermal fluids, especially at relatively low temperatures.[9] Therefore, Giggenbach (1988) suggested that Ca may be used to formulate a f_{CO_2}-indicator, representing the subject of the next section, rather than constituting the basis for a geothermometer.

This suggestion was later confirmed by Chiodini et al. (1991) based on the results of a mineral-solution equilibrium model (see Sect. 5.8).

5.5 The K–Ca f_{CO_2}-Indicator

5.5.1 *Relevant Reactions, Derivation, and Limitations of the K–Ca f_{CO_2}-Indicator*

According to Giggenbach (1988), it is likely that the initial CO_2 contents of deep geothermal fluids in areas affected by magmatic processes are externally controlled by variable contributions of CO_2-rich magmatic fluids and CO_2-poor meteoric waters.

---

[9] For instance, according to Paces (1975), the aqueous solution attains a steady state condition with the felsic rocks, in aquifers at temperatures below 75 °C and CO_2 partial pressures above 10^{-4} atm. Therefore, he suggested an empirical correction involving the aquifer CO_2 partial pressure to be applied to the Na–K–Ca temperature.

These deep geothermal fluids are expected to become reactive with respect to the conversion of Ca–Al-silicates to either calcite and clay minerals or calcite and K-mica. An example of the first process is the reaction:

$$2\,Ca_2Al_3Si_3O_{12}(OH) + 4\,CO_2 + 5\,H_2O = 3\,Al_2Si_2O_5(OH)_4 + 4\,CaCO_3 \quad (5.135)$$

in which the considered Ca–Al-silicate is clinozoisite. Reaction (5.135) involves the formation of kaolinite or similar minerals typical of acid alteration assemblages, such as dickite or pyrophyllite (Reyes 1990). An example of the second process is the reaction:

$$\begin{aligned} &1.5\,KAlSi_3O_8 + Ca_2Al_3Si_3O_{12}(OH) + 2\,CO_{2(g)} + H_2O \\ &\quad = 1.5\,KAl_3Si_3O_{10}(OH)_2 + 3\,SiO_2 + 2\,CaCO_3 \end{aligned} \quad (5.136)$$

in which, again, the Ca–Al-silicate is clinozoisite. The temperature dependence of reaction (5.136) and similar reactions involving Ca–Al-silicates other than clinozoisite is described by the following equation (Giggenbach 1984; f_{CO_2} in bar, T in °C):

$$\log f_{CO_2} = 0.0168\,T - 3.78, \quad (5.137)$$

which is valid from 100 to 350 °C. The univariant reaction (5.136) involves two constituents of the full equilibrium hydrothermal mineral assemblage, K-mica and K-feldspar, and represents the calcite/Ca–Al-silicate boundary. For a given temperature, calcite is stable for f_{CO_2} higher than that given by Eq. (5.137), whereas the Ca–Al-silicate mineral (either laumontite, epidote or wairakite, depending on temperature) is stable for f_{CO_2} lower than that given by Eq. (5.137).

Arnórsson and Gunnlaugsson (1985) recognized that f_{CO_2} is governed, above ~230 °C, by a buffer comprising calcite, epidote, prehnite and quartz and Arnórsson (1985) proposed that the partial pressure of CO_2 is fixed by temperature-dependent mineral-solution equilibria as described by the following relation (P_{CO_2} in bar, T in K):

$$\log P_{CO_2} = -2.81 - 5012.7 \cdot T^{-1} - 0.00919 \cdot T + 6.464 \cdot \log T. \quad (5.138)$$

Equation (5.138) agrees closely with Eq. (5.137) from 200 to 250 °C, whereas the two functions diverge progressively the one from the other below 200 °C and above 250 °C with maximum deviations of about one order of magnitude at 100 and 350 °C. Similar temperature- f_{CO_2} (or P_{CO_2}) relations were also proposed by Giggenbach (1981), Arnórsson et al. (1983a), and Arnórsson and Gunnlaugsson (1985).

According to Giggenbach (1988), the conversion of K-feldspar to K-mica promoted by CO_2 with production of calcite and a silica mineral:

$$3\,\mathrm{KA1Si_3O_8} + \mathrm{CO_{2(g)}} + \mathrm{Ca^{2+}} + \mathrm{H_2O} \\ = \mathrm{CaCO_3} + \mathrm{KAl_3Si_3O_{10}(OH)_2} + 6\mathrm{SiO_2} + 2\mathrm{K^+}, \tag{5.139}$$

is likely to occur over large portions of geothermal systems. The thermodynamic equilibrium constant of reaction (5.139) is equal to $\log(a^2_{\mathrm{K^+}}/a_{\mathrm{Ca^{2+}}}) - \log f_{\mathrm{CO_2}}$ if the solid phases and water are assumed to be pure. Moreover, the log K of reaction (5.139) is practically temperature independent, being equal to -1.66 ± 0.15, in the temperature range 50–300 °C, based on the thermodynamic data of Bowers et al. (1984). Therefore, to a first approximation, the $\mathrm{K^2/Ca}$ concentration ratio can be assumed to be a $f_{\mathrm{CO_2}}$-indicator, as described by the following equation (Giggenbach 1988; concentrations in mg/kg, $f_{\mathrm{CO_2}}$ in bar):

$$\log f_{\mathrm{CO_2}} = \log(\mathrm{c}^2_{\mathrm{K^+}}/\mathrm{c}_{\mathrm{Ca^{2+}}}) - 3.0. \tag{5.140}$$

As underscored by Giggenbach (1988), the K–Ca $f_{\mathrm{CO_2}}$-indicator is based on the hypothesis of chemical equilibrium attainment between the aqueous solution and all the solid phases participating to reaction (5.139). Therefore, the K–Ca $f_{\mathrm{CO_2}}$-indicator can be applied to the comparatively high $\mathrm{CO_2}$ fugacities at which calcite is stable and Ca–Al-silicate minerals are not, whereas it cannot be used at the relatively low $\mathrm{CO_2}$ fugacities where the Ca–Al-silicate minerals are stable and calcite is not. The threshold between these two distinct situations is defined by Eqs. (5.137) or (5.138).

5.5.2 Application of the K–Ca $f_{\mathrm{CO_2}}$-Indicator to the Selected Reservoir Liquids

Giggenbach (1988) used the K–Ca $f_{\mathrm{CO_2}}$-indicator together with the K–Mg geothermometer because these two geo-indicators are expected to equilibrate with comparable speed and under comparable conditions. Since there are several doubts on the reliability of the K–Mg geothermometer (see Sect. 5.6), the results of the K–Ca $f_{\mathrm{CO_2}}$-indicator for the 1013 selected reservoir liquids are plotted against the reference (aquifer) temperatures, instead of the K–Mg temperatures, in the diagrams of Fig. 5.24, also showing the approximate calcite/Ca–Al-silicate stability boundary or full equilibrium lines, represented by Eqs. (5.137) and (5.138).

The data points situated above the full equilibrium lines, such as all or most reservoir liquids of Long Valley (Fig. 5.24b), Mori-Nigorikawa (Fig. 5.24c), Ngawha, Kawerau, Broadlands (Fig. 5.24e), Yangbajing, Kizildere, Latera, Ribeira Grande, Aluto-Langano, and Olkaria (Fig. 5.24f) have computed $\mathrm{CO_2}$ fugacities much higher than the full equilibrium value. Indeed, it is possible that the $\mathrm{CO_2}$ fugacities of these reservoir liquids are externally controlled rather than internally fixed by mineral-solution equilibria.

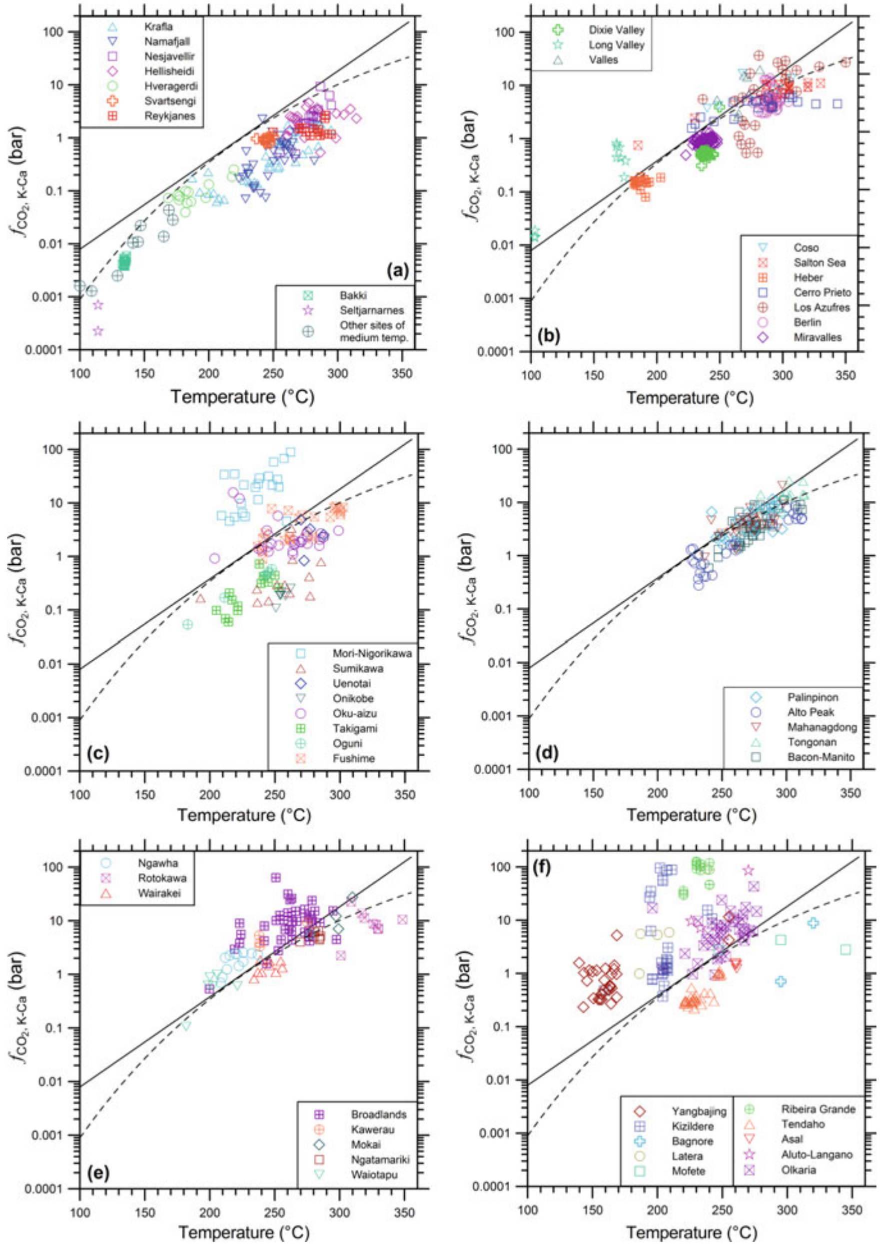

Fig. 5.24 Diagrams of the aquifer temperature versus the CO_2 fugacity computed by means of the K–Ca f_{CO_2}-indicator of Giggenbach (1988), Eq. (5.140), for the selected reservoir liquids from **a** Iceland, **b** Northern-Central America, **c** Japan, **d** The Philippines, **e** New Zealand, and **f** miscellaneous geothermal systems. The CO_2 fugacity spans six orders of magnitude and, therefore, is reported on a log scale. Also shown are the full equilibrium lines of Giggenbach (1984; solid black line), Eq. (5.137), and Arnórsson (1985; dashed black line), Eq. (5.138)

However, calcite scaling is known to occur in these systems, as reported for instance by Brown et al. (2013) for Long Valley, Yoshida (1991) for Mori-Nigorikawa, Sheppard (1984) for Ngawha, Christenson (1997) for Kawerau, Simmons and Christenson (1994) for Broadlands, Zheng et al. (2019) for Yangbajing, Tarcan et al. (2016) for Kizildere, Pieri et al. (1989) for Latera, Viveiros Pereira (2014) for Ribeira Grande, Tassew (2010) for Aluto-Langano, and Opondo (2015) for Olkaria. This process may cause a considerable decrease in Ca concentration and a related increase in both the K^2/Ca concentration ratio and in the computed CO_2 fugacity, which could overestimate the real value.

Further indications are given by the comparison of the CO_2 fugacities computed by means of the K–Ca f_{CO_2}-indicator and the corresponding CO_2 fugacities obtained through speciation calculations, generally carried out by means of the computer code WATCH, that is combining the analyses of the liquid and vapor phases separated at known pressure, temperature conditions. Such a comparison, performed through the log-log diagrams of Fig. 5.25 shows that:

(i) Most reservoir liquids of Long Valley (Fig. 5.25b), Ngawha (Fig. 5.25e) Kizildere, Aluto-Langano, and Latera (Fig. 5.25f) have CO_2 fugacities given by speciation calculations much higher than those given by the K–Ca f_{CO_2}-indicator and, therefore, they might have excess CO_2 with respect to the CO_2 concentration controlled by equilibrium coexistence of calcite, K-feldspar, K-mica and a silica mineral.

(ii) The reservoir liquids of Mori-Nigorikawa (Fig. 5.25c) and Kawerau (Fig. 5.25e) have CO_2 fugacities obtained through speciation calculations similar to those calculated using the K–Ca f_{CO_2}-indicator and, therefore, they might be close to equilibrium with calcite, K-feldspar, K-mica and a silica mineral.

(iii) Most reservoir liquids of Broadlands (Fig. 5.25e) Yangbajing, Ribeira Grande, and Olkaria (Fig. 5.24f) have CO_2 fugacities given by speciation calculations lower than those calculated using the K–Ca f_{CO_2}-indicator. Assuming that the CO_2 fugacities given by speciation calculations are reliable (which is far from certainty), the results of the K–Ca f_{CO_2}-indicator could overestimate the real values because of calcite precipitation.

Returning to consider the diagrams of Fig. 5.24, the sample points positioned below the full equilibrium line, such as the reservoir liquids from the high-temperature Icelandic geothermal systems (Fig. 5.24a), Berlin, Los Azufres (Fig. 5.24b), Fushime, Oku-aizu, Sumikawa, Uenotai (Fig. 5.24c), Alto Peak, Bacon-Manito, Mahanagdong, Palinpinon, and Tongonan (Fig. 5.24d), might indicate that comparatively low contributions of deep CO_2-rich fluids enter these geothermal aquifers from below, stabilizing the Ca–Al-silicates and destabilizing calcite. Alternatively, the low CO_2 concentrations of these reservoir liquids, or at least some of them, could be caused by aquifer boiling which is known to occur in these geothermal systems.

The log-log diagrams of the CO_2 fugacities computed by means of the K–Ca f_{CO_2}-indicator versus the corresponding CO_2 fugacities obtained through speciation calculations (Fig. 5.25) are useful for solving this dilemma. In fact:

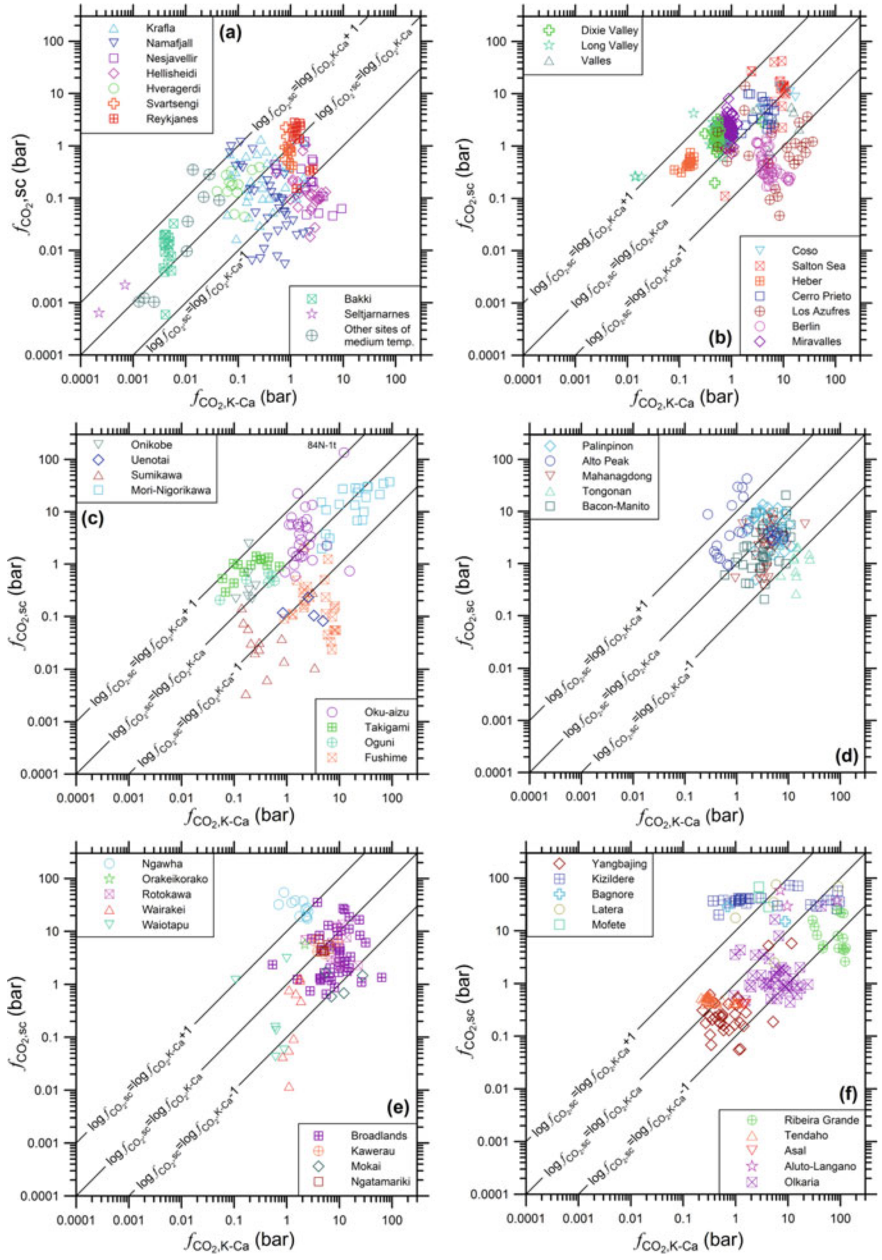

Fig. 5.25 Log-log diagrams of the CO_2 fugacities computed by means of the K–Ca f_{CO_2}-indicator versus the corresponding CO_2 fugacities obtained through speciation calculations, for the selected reservoir liquids from **a** Iceland, **b** Northern-Central America, **c** Japan, **d** The Philippines, **e** New Zealand, and **f** miscellaneous geothermal systems

(i) Most reservoir liquids of Reykjanes, Svartsengi, Hveragerdi, and Bakki (Fig. 5.25a), Oku-aizu (Fig. 5.25c), Alto Peak, Bacon-Manito, Mahanagdong, and Palinpinon (Fig. 5.25d) have CO_2 fugacities obtained through speciation calculations similar to or somewhat higher than those calculated through the K–Ca f_{CO_2}-indicator, suggesting that the occurrence of aquifer boiling is unlikely.

(ii) Several reservoir liquids of Krafla, Namafjall, Nesjavellir, Hellisheidi (Fig. 5.25a), Berlin, Los Azufres (Fig. 5.25b), Fushime, Sumikawa, Uenotai (Fig. 5.25c), and Tongonan (Fig. 5.25d), have CO_2 fugacities given by speciation calculations lower than those computed using the K–Ca f_{CO_2}-indicator, possibly because of aquifer boiling.

According to Giggenbach (1988), K and Ca concentrations can be used to evaluate reliable CO_2 fugacities only for sample points found near the full equilibrium line. However, it cannot be excluded that also these fluids might be affected by the processes mentioned above. Consequently, the results of the K–Ca f_{CO_2}-indicator have always a certain degree of uncertainty.

Further uncertainties are caused by the possible involvement of adularia of variable order-disorder degree in reactions (5.136) and (5.139) instead of fully ordered maximum-microcline as assumed by Giggenbach (1984, 1988). This discussion will be resumed in Chap. 8.

5.6 The K–Mg and Na–Mg Geothermometers

5.6.1 Relevant Reactions, Derivation, and Limitations of the K–Mg and Na–Mg Geothermometers

It was recognized long ago that the waters of high temperature (250–300 °C) and low salinity have exceptionally low Mg concentrations, typically 10–100 ppb only (Mahon 1965). Moreover, it was also understood that Mg concentrations are strongly dependent on temperature, and this relationship was attributed to equilibration of geothermal liquids with chlorites owing to their ubiquitous occurrence in the hydrothermal alteration parageneses. Ellis (1971) carried out laboratory experiments to investigate the chemistry of the aqueous solution in equilibrium with chlorite, calcite, and quartz, under controlled CO_2 partial pressures and to calibrate the temperature dependence of Mg concentration. Starting from these premises, Giggenbach (1988) assumed that the behavior of Mg in well-equilibrated geothermal waters is described by the following two reactions:

$$\begin{aligned}&0.8\,\text{muscovite} + 0.2\,\text{clinochlore} + 5.4\,\text{chalcedony} + 2K^+\\&\quad = 2.8\text{K-feldspar} + 1.6H_2O + Mg^{2+}\end{aligned}\tag{5.141}$$

and

$$\begin{aligned} &0.8 \text{ muscovite } + 0.2 \text{ clinochlore } + 5.4 \text{ chalcedony } + 2\mathrm{Na}^+ \\ &\quad = 2 \text{ albite } + 0.8\text{K-feldspar } + 1.6\mathrm{H_2O} + \mathrm{Mg}^{2+}, \end{aligned} \tag{5.142}$$

which are written involving clinochlore and muscovite as endmember components of chlorites and illites, respectively. The corresponding equilibrium constants are:

$$\mathrm{K}_{\mathrm{Mg-K}} = \frac{a_{\mathrm{Mg}^{2+}}}{a_{\mathrm{K}^+}^2} \frac{a_{\mathrm{Kfs}}^{2.8} \cdot a_{\mathrm{H_2O}}^{1.6}}{a_{\mathrm{Ms}}^{0.8} \cdot a_{\mathrm{Clc}}^{0.2} \cdot a_{\mathrm{Chc}}^{5.4}} \tag{5.143}$$

$$\mathrm{K}_{\mathrm{Mg-Na}} = \frac{a_{\mathrm{Mg}^{2+}}}{a_{\mathrm{Na}^+}^2} \frac{a_{\mathrm{Ab}}^{2} \cdot a_{\mathrm{Kfs}}^{0.8} \cdot a_{\mathrm{H_2O}}^{1.6}}{a_{\mathrm{Ms}}^{0.8} \cdot a_{\mathrm{Clc}}^{0.2} \cdot a_{\mathrm{Chc}}^{5.4}}. \tag{5.144}$$

The activities of H_2O, chalcedony, and alkali feldspars are close to unit, whereas the effects of clinochlore and muscovite incorporation into natural chlorites and illites was assessed by Giggenbach (1988) considering the data reported by Capuano and Cole (1982) for Roosevelt Hot Springs and by Walshe (1986) for a number of hydrothermal phyllosilicates.

The logarithm of clinochlore activity in the chlorites of interest varies from −4.7 to −1.3 with a mean of −2.2. The logarithm of muscovite activity in the considered illites ranges from −0.73 to −0.15 with an average of −0.33. Hence, the logarithm of the activity product $\mathrm{AP} = a_{\mathrm{Ms}}^{0.8} \cdot a_{\mathrm{Clc}}^{0.2}$ ranges from −1.5 to −0.4 with a mean of −0.7. Instead of considering this average AP, Giggenbach (1988) arbitrarily assumed an AP value of +0.3 to derive the K–Mg geothermometer, obtaining the following equations, for concentrations $\mathrm{c_i}$ in mg/kg and m_i in mol/kg:

$$\mathrm{T} = \frac{4410}{14.0 - \log(\mathrm{c_K^2} / \mathrm{c_{Mg}})} - 273.15 \quad \mathrm{T} = \frac{4410}{9.2 - \log(m_\mathrm{K}^2 / m_\mathrm{Mg})} - 273.15. \tag{5.145}$$

Giggenbach (1988) justified the choice of the AP value of +0.3 to adjust for the positions of high-temperature data points in a plot of log $(a_{\mathrm{Mg}^{2+}} / a_{\mathrm{K}^+}^2)$ versus the absolute temperature inverse (Fig. 5b of Giggenbach 1988) and with the assumption that measured temperatures of low-temperature waters are likely to underestimate their actual mineral-solution equilibrium temperatures. Moreover, Giggenbach (1988) concluded that there is no reason to favor a theoretical over the empirical calibration, because of possible uncertainties in the thermodynamic properties adopted for K-feldspar, muscovite and clinochlore, that were obtained from Bowers et al. (1984). Summing up, the K–Mg geothermometer is empirical and its derivation leaves much to be desired. Equation (5.145) is slightly different from the relation previously published by Giggenbach et al. (1983) whose intercept (entropy term) is 13.95 instead of 14.0 for concentrations in mg/kg.

In addition to the temperature dependence of the Na/K and K^2/Mg concentration ratios, Giggenbach (1988) also computed the internally consistent temperature dependence of the Na^2/Mg concentration ratio inserting Eqs. (5.66) and (5.145) into the following simple relation, written for concentrations in mg/kg:

$$\log(c_{Na}^2/c_{Mg}) = \log(c_K^2/c_{Mg}) + 2 \cdot \log(c_{Na}/c_K). \tag{5.146}$$

Because of the infinite number of possible Na–K geothermometers (see chapter 5.3), there is also an infinite number of possible Na–Mg geothermometers, which are related to the K–Mg geothermometer of Giggenbach (1988) through Eq. (5.146). However, only the sixteen empirical Na–K geothermometers, with linear dependence on the absolute temperature inverse (see Table 5.2 in chapter 5.3), were alternatively inserted into Eq. (5.146) together with K–Mg geothermometer of Giggenbach (1988) expressed by Eq. (5.145) to keep the following discussion to a simple level. In this way, the sixteen Na–Mg geothermometers listed in Table 5.5 were obtained. Again, two relations are reported, one for concentrations in mg/kg, the other for molal concentrations, although the conversion from one form to the other is straightforward.

As part of their systematic, computerized procedure, Nieva and Nieva (1987) proposed the following Na–K–Mg relation:

$$T = \frac{11140}{18.30 + 6 \cdot \log(m_{Na}/m_K) + \log(m_{Mg}/m_{Na}^2)} - 273.15. \tag{5.163}$$

Inserting the Na–K geothermometer of Nieva and Nieva (1987), i.e. Eqn (5.67), into Eq. (5.163) and rearranging, one obtains the following Na–Mg geothermometric equation (indicated by code NiNi87b) for concentrations c_i in mg/kg and m_i in mol/kg:

$$\begin{aligned} T &= \frac{4072}{10.866 - \log(m_{Na}^2/m_{Mg})} - 273.15, \\ T &= \frac{4072}{15.203 - \log(c_{Na}^2/c_{Mg})} - 273.15. \end{aligned} \tag{5.164}$$

The corresponding K–Mg geothermometer is then derived by inserting the Na–K and Na–Mg geothermometers of Nieva and Nieva (1987), that is Eqs. (5.67) and (5.164), in consistent units, into Eq. (5.146) and reorganizing:

$$\begin{aligned} T &= \frac{6428}{13.344 - \log(m_K^2/m_{Mg})} - 273.15, \\ T &= \frac{6428}{18.143 - \log(c_K^2/c_{Mg})} - 273.15. \end{aligned} \tag{5.165}$$

Table 5.5 Na–Mg geothermometers obtained from the K–Mg geothermometer of Giggenbach (1988) and different Na–K geothermometers, as indicated

Na–K references	Na–Mg function involving molal concentrations	Na–Mg function involving concentrations in mg/kg	Code	Eqn. #
White (1968)	$T = \frac{3401.8}{9.32 - \log\left(\frac{m_{Na}^2}{m_{Mg}}\right)} - 273.15$	$T = \frac{3401.8}{13.66 - \log\left(\frac{c_{Na}^2}{c_{Mg}}\right)} - 273.15$	Wh68	(5.147)
Ellis (1970)	$T = \frac{2807}{8.16 - \log\left(\frac{m_{Na}^2}{m_{Mg}}\right)} - 273.15$	$T = \frac{2807}{12.50 - \log\left(\frac{c_{Na}^2}{c_{Mg}}\right)} - 273.15$	El70	(5.148)
Mercado (1970)	$T = \frac{3129}{8.72 - \log\left(\frac{m_{Na}^2}{m_{Mg}}\right)} - 273.15$	$T = \frac{3129}{13.06 - \log\left(\frac{c_{Na}^2}{c_{Mg}}\right)} - 273.15$	Me70	(5.149)
Fournier and Truesdell (1973)	$T = \frac{2856}{8.26 - \log\left(\frac{m_{Na}^2}{m_{Mg}}\right)} - 273.15$	$T = \frac{2856}{12.60 - \log\left(\frac{c_{Na}^2}{c_{Mg}}\right)} - 273.15$	FoTr73	(5.150)
Truesdell (1976)	$T = \frac{2698.8}{7.95 - \log\left(\frac{m_{Na}^2}{m_{Mg}}\right)} - 273.15$	$T = \frac{2698.8}{12.29 - \log\left(\frac{c_{Na}^2}{c_{Mg}}\right)} - 273.15$	Tr76	(5.151)
Fournier (1979)	$T = \frac{1976}{6.70 - \log\left(\frac{m_{Na}^2}{m_{Mg}}\right)} - 273.15$	$T = \frac{1976}{11.03 - \log\left(\frac{c_{Na}^2}{c_{Mg}}\right)} - 273.15$	Fo79	(5.152)
Tonani (1980)	$T = \frac{2744}{8.10 - \log\left(\frac{m_{Na}^2}{m_{Mg}}\right)} - 273.15$	$T = \frac{2744}{12.44 - \log\left(\frac{c_{Na}^2}{c_{Mg}}\right)} - 273.15$	To80	(5.153)
Arnórsson et al. (1983a), 25–250 °C	$T = \frac{2544}{7.68 - \log\left(\frac{m_{Na}^2}{m_{Mg}}\right)} - 273.15$	$T = \frac{2544}{12.01 - \log\left(\frac{c_{Na}^2}{c_{Mg}}\right)} - 273.15$	Ar83, LT	(5.154)
Arnórsson et al. (1983a),250–350 °C	$T = \frac{1772}{6.27 - \log\left(\frac{m_{Na}^2}{m_{Mg}}\right)} - 273.15$	$T = \frac{1772}{10.60 - \log\left(\frac{c_{Na}^2}{c_{Mg}}\right)} - 273.15$	Ar83, HT	(5.155)

(continued)

Table 5.5 (continued)

Na–K references	Na–Mg function involving molal concentrations	Na–Mg function involving concentrations in mg/kg	Code	Eqn. #
Giggenbach (1988)	$\mathrm{T} = \frac{1630}{6.16 - \log\left(\frac{m_{\mathrm{Na}}^2}{m_{\mathrm{Mg}}}\right)} - 273.15$	$\mathrm{T} = \frac{1630}{10.50 - \log\left(\frac{\mathrm{c}_{\mathrm{Na}}^2}{\mathrm{c}_{\mathrm{Mg}}}\right)} - 273.15$	Gi88	(5.156)
Nieva and Nieva (1987)	$\mathrm{T} = \frac{2054}{6.72 - \log\left(\frac{m_{\mathrm{Na}}^2}{m_{\mathrm{Mg}}}\right)} - 273.15$	$\mathrm{T} = \frac{2054}{11.06 - \log\left(\frac{\mathrm{c}_{\mathrm{Na}}^2}{\mathrm{c}_{\mathrm{Mg}}}\right)} - 273.15$	NiNi87a	(5.157)
Kharaka and Mariner (1989)	$\mathrm{T} = \frac{2050}{7.04 - \log\left(\frac{m_{\mathrm{Na}}^2}{m_{\mathrm{Mg}}}\right)} - 273.15$	$\mathrm{T} = \frac{2050}{11.38 - \log\left(\frac{\mathrm{c}_{\mathrm{Na}}^2}{\mathrm{c}_{\mathrm{Mg}}}\right)} - 273.15$	KhMa89	(5.158)
Michard (1990)	$\mathrm{T} = \frac{2070}{6.36 - \log\left(\frac{m_{\mathrm{Na}}^2}{m_{\mathrm{Mg}}}\right)} - 273.15$	$\mathrm{T} = \frac{2070}{10.70 - \log\left(\frac{\mathrm{c}_{\mathrm{Na}}^2}{\mathrm{c}_{\mathrm{Mg}}}\right)} - 273.15$	Mi90	(5.159)
Verma and Santoyo (1997)	$\mathrm{T} = \frac{1832}{6.43 - \log\left(\frac{m_{\mathrm{Na}}^2}{m_{\mathrm{Mg}}}\right)} - 273.15$	$\mathrm{T} = \frac{1832}{10.77 - \log\left(\frac{\mathrm{c}_{\mathrm{Na}}^2}{\mathrm{c}_{\mathrm{Mg}}}\right)} - 273.15$	VeSa97	(5.160)
Santoyo and Díaz-González (2010)	$\mathrm{T} = \frac{2657.4}{7.91 - \log\left(\frac{m_{\mathrm{Na}}^2}{m_{\mathrm{Mg}}}\right)} - 273.15$	$\mathrm{T} = \frac{2657.4}{12.25 - \log\left(\frac{\mathrm{c}_{\mathrm{Na}}^2}{\mathrm{c}_{\mathrm{Mg}}}\right)} - 273.15$	SaDi10	(5.161)
Simmons (2013)	$\mathrm{T} = \frac{3780}{10.14 - \log\left(\frac{m_{\mathrm{Na}}^2}{m_{\mathrm{Mg}}}\right)} - 273.15$	$\mathrm{T} = \frac{3780}{14.47 - \log\left(\frac{\mathrm{c}_{\mathrm{Na}}^2}{\mathrm{c}_{\mathrm{Mg}}}\right)} - 273.15$	Si13	(5.162)

Based on the chemical characteristics of waters interacting with granitic lithotypes at temperatures lower than 150 °C, Michard (1990) derived a K–Mg geothermometer, which is defined by the following two relations (indicated by code Mi90b):

$$\begin{aligned} \mathrm{T} &= \frac{3000}{5.84 - \log\left(m_{\mathrm{K}}^{2} / m_{\mathrm{Mg}}\right)} - 273.15, \\ \mathrm{T} &= \frac{3000}{10.64 - \log\left(\mathrm{c}_{\mathrm{K}}^{2} / \mathrm{c}_{\mathrm{Mg}}\right)} - 273.15. \end{aligned} \tag{5.166}$$

The corresponding Na–Mg geothermometer is obtained inserting the Na–K and K–Mg geothermometers of Michard (1990), that is Eqs. (5.69) and (5.166), in consistent units, into Eq. (5.146) and rearranging:

$$\mathrm{T} = \frac{660}{3.00 - \log\left(m_{\mathrm{Na}}^{2} / m_{\mathrm{Mg}}\right)} - 273.15, \quad \mathrm{T} = \frac{660}{7.34 - \log\left(\mathrm{c}_{\mathrm{Na}}^{2} / \mathrm{c}_{\mathrm{Mg}}\right)} - 273.15. \tag{5.167}$$

These two functions should not be used outside the calibration range, that is above 150 °C.

Two K–Mg geothermometric functions were proposed by Fournier (1991). However, the equations listed in Table 3 of Fournier (1991) are at variance with the corresponding lines reported in the diagram of $\log(\mathrm{K}^2/\mathrm{Mg})$ versus the absolute temperature reciprocal, that is Fig. 9 of Fournier (1991). Relying on the diagram, the two K–Mg geothermometers of Fournier (1991) are defined by the following relations (indicated by code Fo91a and Fo91b) for concentrations c_{i} in mg/kg and m_{i} in mol/kg:

$$\begin{aligned} \mathrm{T} &= \frac{2680}{4.60 - \log\left(m_{\mathrm{K}}^{2} / m_{\mathrm{Mg}}\right)} - 273.15 \\ \mathrm{T} &= \frac{2680}{9.40 - \log\left(\mathrm{c}_{\mathrm{K}}^{2} / \mathrm{c}_{\mathrm{Mg}}\right)} - 273.15, \end{aligned} \tag{5.168}$$

$$\begin{aligned} \mathrm{T} &= \frac{6460}{13.30 - \log\left(m_{\mathrm{K}}^{2} / m_{\mathrm{Mg}}\right)} - 273.15 \\ \mathrm{T} &= \frac{6460}{18.10 - \log\left(\mathrm{c}_{\mathrm{K}}^{2} / \mathrm{c}_{\mathrm{Mg}}\right)} - 273.15. \end{aligned} \tag{5.169}$$

Equation (5.168) is valid for $\log(\mathrm{K}^2/\mathrm{Mg}) < 3.25$, corresponding to $\mathrm{T} < 162.5$ °C, whereas Eq. (5.169) holds for $\log(\mathrm{K}^2/\mathrm{Mg}) > 3.25$, that is for $\mathrm{T} > 162.5$ °C. The two related Na–Mg geothermometers are derived by inserting the Na–K geothermometer of Fournier (1979), Eq. (5.62), and each one of the two K–Mg geothermometers into Eq. (5.146), thus obtaining:

$$\begin{aligned} \mathrm{T} &= \frac{246}{2.097 - \log\left(m_{\mathrm{Na}}^{2} \middle/ m_{\mathrm{Mg}}\right)} - 273.15, \\ \mathrm{T} &= \frac{246}{6.434 - \log\left(\mathrm{c}_{\mathrm{Na}}^{2} \middle/ \mathrm{c}_{\mathrm{Mg}}\right)} - 273.15 \end{aligned} \tag{5.170}$$

$$\begin{aligned} \mathrm{T} &= \frac{4026}{10.797 - \log\left(m_{\mathrm{Na}}^{2} \middle/ m_{\mathrm{Mg}}\right)} - 273.15, \\ \mathrm{T} &= \frac{4026}{15.134 - \log\left(\mathrm{c}_{\mathrm{Na}}^{2} \middle/ \mathrm{c}_{\mathrm{Mg}}\right)} - 273.15. \end{aligned} \tag{5.171}$$

As shown by the diagram of $\log(m_{\mathrm{K}}^{2}/m_{\mathrm{Mg}})$ versus the absolute temperature inverse (Fig. 5.26), the high-slope K–Mg geothermometer of Fournier (1991), code Fo91b, is very close to the K–Mg function of Nieva and Nieva (1987), code NiNi87b. The K–Mg geothermometer of Giggenbach (1988) intersects these two functions at temperatures of 210–230 °C, while it progressively diverges from both relations at higher and lower temperatures. Of the two remaining K–Mg geothermometers, the low-slope function of Fournier (1991), code Fo91a, crosses the other relations, whereas that of Michard (1990), code Mi90b, is positioned somewhat above them.

The plot of $\log(m_{\mathrm{Na}}^{2}/m_{\mathrm{Mg}})$ versus the absolute temperature reciprocal (Fig. 5.27) shows that there are considerable differences among the twenty Na–Mg geothermometers, including those reported in Table 5.5, and Eqs. (5.164), (5.167), (5.170), and (5.171). The two low-slope relations of Michard (1990) and Fournier (1991), codes Mi90b and Fo91a, are limited below 150 and 160 °C, respectively. Most of the

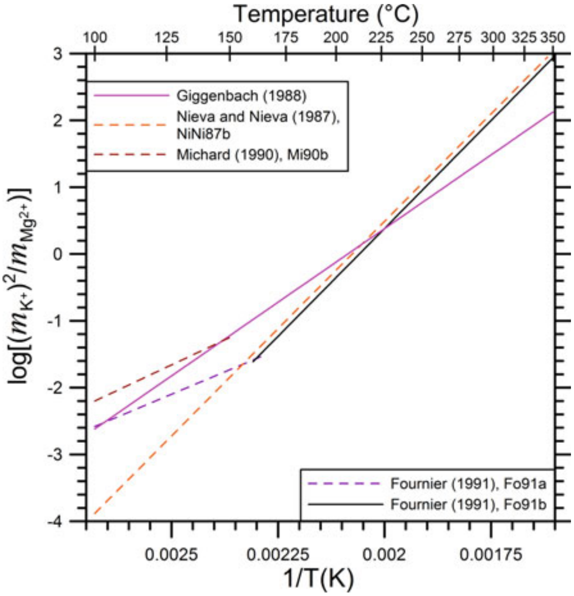

Fig. 5.26 Diagram of $\log(m_{\mathrm{K}}^{2}/m_{\mathrm{Mg}})$ versus the absolute temperature inverse showing the K–Mg geothermometers of Giggenbach (1988), Michard (1990), and Fournier (1991), as well as that obtained from the Na–K–Mg relation of Nieva and Nieva (1987)

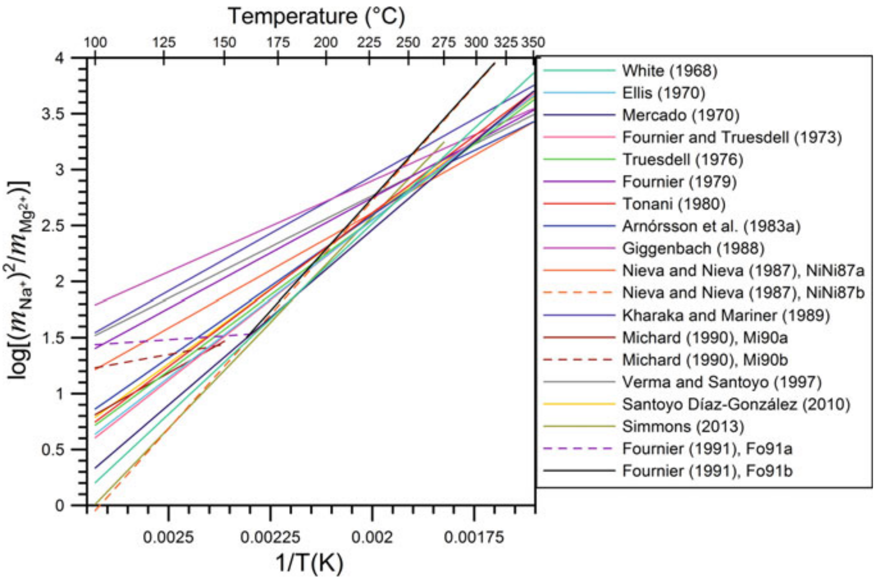

Fig. 5.27 Diagram of $\log(m^2_{\text{Na}}/m_{\text{Mg}})$ versus the absolute temperature inverse showing the sixteen Na–Mg geothermometers obtained from the K–Mg geothermometer of Giggenbach (1988) and the sixteen empirical Na–K functions (see legend) as well as the Na–Mg geothermometers related to the K–Mg geothermometers of Michard (1990) and Fournier (1991), and to the Na–K–Mg relation of Nieva and Nieva (1987)

other eighteen geothermometric functions converge at 225–275 °C, but diverge more and more at decreasing and increasing temperatures. As expected, the spread of the Na–Mg linear functions obtained from the K–Mg geothermometer of Giggenbach (1988) and the sixteen empirical Na–K functions is similar to that of the corresponding Na/K geothermometers (Fig. 5.14). To be noted that the Na–Mg geothermometers of comparatively low slope are derived from the Na–K geothermometers of relatively high slope (e.g., Giggenbach 1988) and vice versa (e.g., Simmons 2013). This is also expected, because each pair of Na–Mg and Na–K equations is interconnected by Eq. (5.146).

5.6.2 Application of the K–Mg and Na–Mg Geothermometers to the Selected Reservoir Liquids

In the correlation diagrams of $\log(m^2_{\text{K}}/m_{\text{Mg}})$ versus the absolute temperature reciprocal (Fig. 5.28) there is a large scatter of data points which are positioned both above and below the solid black lines representing the K–Mg geothermometric functions of Giggenbach (1988) and Fournier (1991), and that obtained from the Na–K–Mg

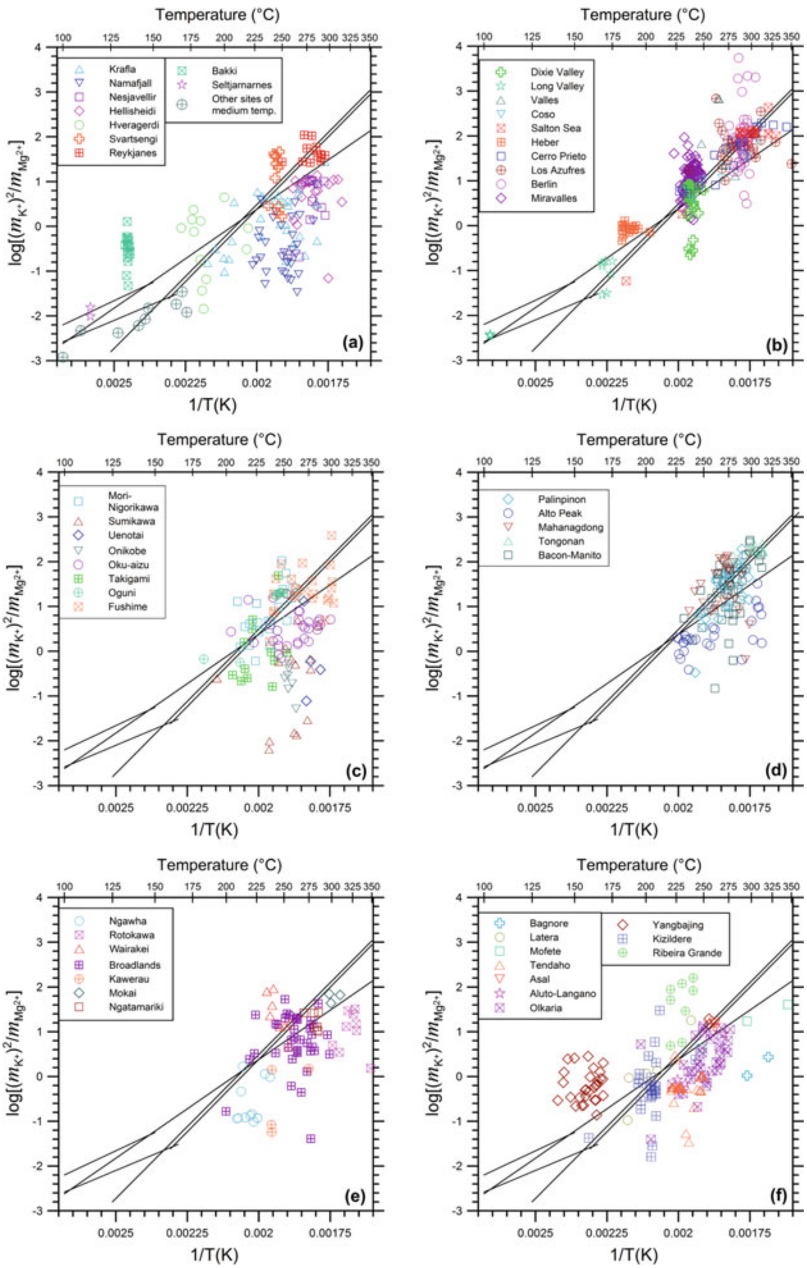

Fig. 5.28 Diagrams of $\log(m_{\mathrm{K}}^2/m_{\mathrm{Mg}})$ versus the absolute temperature inverse showing the selected reservoir liquids from **a** Iceland, **b** Northern-Central America, **c** Japan, **d** The Philippines, **e** New Zealand, and **f** miscellaneous geothermal systems as well as the K–Mg geothermometers of Giggenbach (1988), Michard (1990), Fournier (1991), and that obtained from the Na–K–Mg relation of Nieva and Nieva (1987), all represented by black solid lines

relation of Nieva and Nieva (1987). Most deviations of data points from these K–Mg geothermometers are less than ~ 1.5 log-units, but maximum shifts achieve ~2.5 log-units. Deviations of data points from the K-Mg geothermometers seem to be temperature independent. Also the binary plots of $\log(m_{\mathrm{Na}}^2/m_{\mathrm{Mg}})$ versus the absolute temperature reciprocal (Fig. 5.29) exhibit a considerable scatter of sample points which, again, are located both above and below the lines corresponding to the different Na–Mg geothermometric functions. The remarkable scatter of data points in the diagrams of Figs. 5.28 and 5.29 is probably due to different causes.

Low values of the $(m_{\mathrm{K}}^2/m_{\mathrm{Mg}})$ and $(m_{\mathrm{Na}}^2/m_{\mathrm{Mg}})$ ratios might be explained by the presence of excess magnesium due to mixing of reservoir liquids with Mg-rich external fluids coming from shallower and colder environments. Reservoir liquids with noticeable excess magnesium occur at Krafla, Namafjall, Nesjavellir, and Hellisheidi (Figs. 5.28a and 5.29a), Dixie Valley (Figs. 5.28b and 5.29b), Onikobe, Sumikawa, and Uenotai (Figs. 5.28c and 5.29c), Alto Peak (Figs. 5.28d and 5.29d), Broadlands, Kawerau, Ngawha, and Rotokawa (Figs. 5.28e and 5.29e), Bagnore, Kizildere, Olkaria, and Tendaho (Figs. 5.28f and 5.29f).

In contrast, high values of the $(m_{\mathrm{K}}^2/m_{\mathrm{Mg}})$ and $(m_{\mathrm{Na}}^2/m_{\mathrm{Mg}})$ ratios might be due to loss of magnesium, possibly because of Mg incorporation in the lattice of precipitating calcite or other solid phases. This process might be invoked for some reservoir liquids of Reykjanes, Svartsengi, Hveragerdi, and Bakki (Figs. 5.28a and 5.29a), Berlin, Los Azufres, Miravalles, and Valles (Figs. 5.28b and 5.29b), Mori-Nigorikawa, Fushime, Oguni, and Takigami (Figs. 5.28c and 5.29c), Bacon-Manito, Mahanagdong, Palinpinon, and Tongonan (Figs. 5.28d and 5.29d), Wairakei and Broadlands (Figs. 5.28e and 5.29e), Ribeira Grande, Kizildere, and Yangbajing (Figs. 5.28f and 5.29f).

High and low values of the $(m_{\mathrm{K}}^2/m_{\mathrm{Mg}})$ and $(m_{\mathrm{Na}}^2/m_{\mathrm{Mg}})$ ratios might be due to the presence of illites and especially chlorites of varying compositions, as documented by the chemical data of these hydrothermal solid phases coming from active geothermal systems, which are discussed in Sects. 4.3 and 4.4.

Still another cause might be the variable degree of ordering on the tetrahedral sites of adularia. Accepting that the differences among the Na–K geothermometers are due to the variable order-disorder degree of adularia involved in the exchange reaction with low-albite (see Sect. 5.3.4), also the differences among the K–Mg geothermometers and among the Na–Mg geothermometers could be ascribable to the same reason.

Since the stoichiometric coefficient of adularia is 0.8 in the exchange reaction (5.142) governing the Na–Mg geothermometer and 2.8 in the exchange reaction (5.141) controlling the K–Mg geothermometer, it is reasonable to hypothesize that the impact of variable ordering on the tetrahedral sites of adularia is more important on the K–Mg relation than on the Na–Mg function.

Finally, it is possible that in some systems or in some parts of a given geothermal system, the $(m_{\mathrm{K}}^2/m_{\mathrm{Mg}})$ and $(m_{\mathrm{Na}}^2/m_{\mathrm{Mg}})$ ratios are not controlled by chlorites, but by other Mg-bearing minerals, as discussed in the next section.

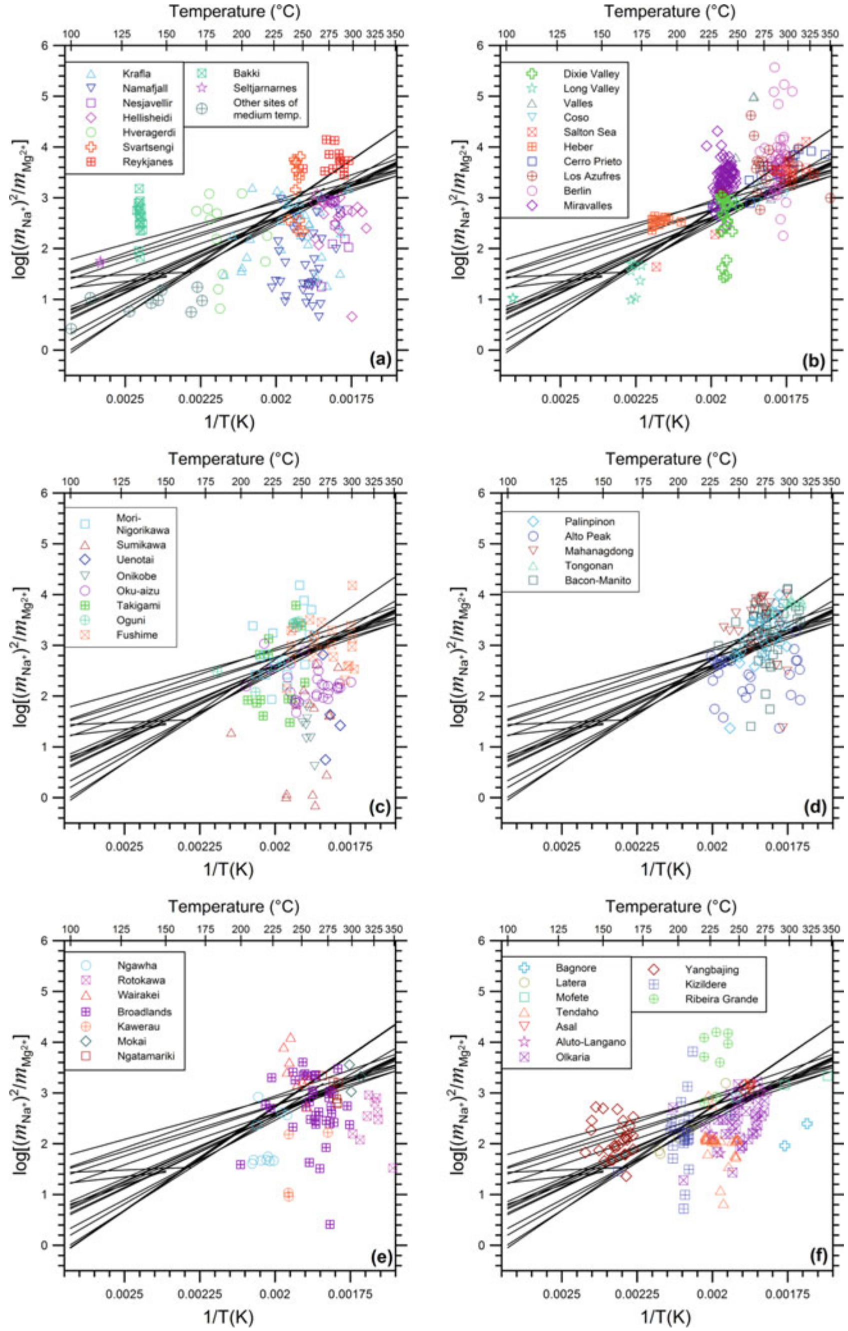

Fig. 5.29 Diagrams of $\log(m^2_{\mathrm{Na}}/m_{\mathrm{Mg}})$ versus the absolute temperature inverse showing the selected reservoir liquids from **a** Iceland, **b** Northern-Central America, **c** Japan, **d** The Philippines, **e** New Zealand, and **f** miscellaneous geothermal systems as well as different Na–Mg geothermometers (solid black lines)

5.6.2.1 The Hydrothermal Minerals Controlling the K–Mg and Na–Mg Geothermometers

As recalled above, Giggenbach (1988) assumed that the K–Mg and Na–Mg geothermometers are controlled by reactions (5.141) and (5.142), both involving clinochlore as Mg-bearing mineral. This is the only chlorite component present in the thermodynamic database of Helgeson et al. (1978), in the two distinct forms with basal spacing of 7 and 14 Å (Sect. 4.4.4).

Other Mg-bearing hydrothermal solid phases occur in active geothermal systems, such as biotite, clinopyroxene, and amphibole, generally above 275 °C, and dolomite, talc, and different clay minerals (e.g., smectites, vermiculites, and saponites), usually below 180 °C. Since no clays are included in the thermodynamic dataset of Helgeson et al. (1978), the thermodynamic properties of Na-montmorillonite, K-montmorillonite, and Mg-montmorillonite were taken from Wolery et al. (2007) and these three minerals were added to the SUPCRT92 database.

Then, the thermodynamic properties of the K–Mg and Na–Mg exchange reactions involving 7Å-clinochlore [Clc, $Mg_5Al_2Si_3O_{10}(OH)_8$], phlogopite [Phl, $KMg_3(AlSi_3)O_{10}(OH)_2$], diopside [Di, $CaMgSi_2O_6$], tremolite [Tr, $Ca_2Mg_5Si_8O_{22}(OH)_2$], ordered and disordered dolomite [Dol, $CaMg(CO_3)_2$], talc [Tlc, $Mg_3Si_4O_{10}(OH)_2$], and Mg-montmorillonite [Mg-Mnt, $Mg_{0.495}Al_{1.67}Si_4O_{10}(OH)_2$] were computed as a function of temperature at water saturation pressures using SUPCRT92. In addition to reaction (5.141), the following K–Mg exchange reactions were also considered:

$$\begin{aligned}&3.33\,KAlSi_3O_8 + 1.33\,H_2O + Mg^{2+}\\&\quad = 0.33\,KMg_3(AlSi_3)O_{10}(OH)_2 + KAl_3Si_3O_{10}(OH)_2 + 6\,SiO_2 + 2\,K^+\end{aligned} \tag{5.172}$$

$$\begin{aligned}&3.75\,KAlSi_3O_8 + 0.5\,Ca_2Al_3Si_3O_{12}(OH) + 1.5\,H_2O + Mg^{2+}\\&\quad = CaMgSi_2O_6 + 1.75\,KAl_3Si_3O_{10}(OH)_2 + 5.5\,SiO_2 + 2\,K^+\end{aligned} \tag{5.173}$$

$$\begin{aligned}&3.3\,KAlSi_3O_8 + 0.2\,Ca_2Al_3Si_3O_{12}(OH) + 1.4\,H_2O + Mg^{2+}\\&\quad = 0.2\,Ca_2Mg_5Si_8O_{22}(OH)_2 + 1.3\,KAl_3Si_3O_{10}(OH)_2 + 5\,SiO_2 + 2\,K^+\end{aligned} \tag{5.174}$$

$$\begin{aligned}&2.25\,KAlSiO_8 + 2\,CaCO_3 + 0.5\,H_2O + Mg^{2+}\\&\quad = CaMg(CO_3)_2 + 0.5\,Ca_2Al_3Si_3O_{12}(OH)\\&\qquad + 0.25\,KAl_3Si_3O_{10}(OH)_2 + 4.5\,SiO_2 + 2\,K^+\end{aligned} \tag{5.175}$$

$$\begin{aligned}&3\,KAlSi_3O_8 + 1.33\,H_2O + Mg^{2+}\\&\quad = 0.33\,Mg_3Si_4O_{10}(OH)_2 + KAl_3Si_3O_{10}(OH)_2 + 4.67\,SiO_2 + 2\,K^+\end{aligned} \tag{5.176}$$

$$6.06\,K_{0.33}Mg_{0.33}Al_{1.67}Si_4O_{10}(OH)_2 + Mg^{2+}$$

$$= 6.06\,\mathrm{Mg_{0.495}Al_{1.67}Si_4O_{10}(OH)_2} + 2\,\mathrm{K^+}. \tag{5.177}$$

Similarly, in addition to reaction (5.142), the other Na–Mg exchange reactions taken into account are:

$$\begin{aligned}&1.33\,\mathrm{KAlSi3O_8} + \mathrm{2NaAlSi_3O_8} + \mathrm{1.33H_2O} + \mathrm{Mg^{2+}}\\&\quad = \mathrm{0.33KMg_3(AlSi_3)O_{10}(OH)_2} + \mathrm{KAl_3Si_{13}O_{10}(OH)_2} + \mathrm{6SiO_2} + \mathrm{2Na^+}\end{aligned} \tag{5.178}$$

$$\begin{aligned}&1.75\,\mathrm{KAlSi_3O_8} + \mathrm{2NaAlSi_3O_8}\\&\quad + \mathrm{0.5Ca_2Al_3Si_3O_{12}(OH)} + \mathrm{1.5H_2O} + \mathrm{Mg^{2+}}\\&\quad = \mathrm{CaMgSi_2O_6} + \mathrm{1.75KAl_3Si_3O_{10}(OH)_2} + \mathrm{5.5SiO_2} + \mathrm{2Na^+}\end{aligned} \tag{5.179}$$

$$\begin{aligned}&\mathrm{1.3KAlSi_3O_8} + \mathrm{2NaAlSi_3O_8} + \mathrm{0.2Ca_2Al_3Si_3O_{12}(OH)} + \mathrm{1.4H_2O} + \mathrm{Mg^{2+}}\\&\quad = \mathrm{0.2Ca_2Mg_5Si_8O_{22}(OH)_2} + \mathrm{1.3KAl_3Si_3O_{10}(OH)_2} + \mathrm{5SiO_2} + \mathrm{2Na^+}\end{aligned} \tag{5.180}$$

$$\begin{aligned}&0.25\,\mathrm{KAlSi_3O_8} + 2\,\mathrm{NaAlSi_3O_8} + 2\,\mathrm{CaCO_3} + 0.5\,\mathrm{H_2O} + \mathrm{Mg^{2+}}\\&\quad = \mathrm{CaMg(CO_3)_2} + 0.5\,\mathrm{Ca_2Al_3Si_3O_{12}(OH)}\\&\quad + 0.25\,\mathrm{KAl_3Si_3O_{10}(OH)_2} + 4.5\,\mathrm{SiO_2} + 2\,\mathrm{Na^+}\end{aligned} \tag{5.181}$$

$$\begin{aligned}&\mathrm{KAlSi_3O_8} + 2\,\mathrm{NaAlSi_3O_8} + 1.33\,\mathrm{H_2O} + \mathrm{Mg^{2+}}\\&\quad = 0.33\,\mathrm{Mg_3Si_4O_{10}(OH)_2} + \mathrm{KAl_3Si_3O_{10}(OH)_2} + 4.67\,\mathrm{SiO_2} + 2\,\mathrm{Na^+}\end{aligned} \tag{5.182}$$

$$\begin{aligned}&6.06\,\mathrm{Na_{0.33}Mg_{0.33}Al_{1.67}Si_4O_{10}(OH)_2} + \mathrm{Mg^{2+}}\\&\quad = \mathrm{6.06Mg_{0.495}Al_{1.67}Si_4O_{10}(OH)_2} + \mathrm{2Na^+}.\end{aligned} \tag{5.183}$$

Clinozoisite was adopted to balance the calcium ions present in the lattice of diopside, tremolite, and dolomite. Calcite was assumed to take part to reactions (5.175) and (5.181) to balance the carbonate ions of dolomite. Apart from reactions (5.177) and (5.183), which comprise montmorillonites only, maximum-microcline and high-sanidine were alternatively involved in all the other reactions, in which the stoichiometric coefficients of alkali feldspars and silica minerals are higher than those of relevant Mg-bearing phases. Therefore, the contributions of Mg-bearing solid phases to the thermodynamic properties of all K–Mg and Na–Mg exchange reactions, apart from (5.177) and (5.183), are expected to be less important than those of alkali feldspars and silica minerals.

The ΔH°_r and ΔS°_r values of the empirical K–Mg geothermometers, calculated from their slope and intercept using Eqs. (5.13) and (5.14), are compared with the ΔH°_r and ΔS°_r values of the K–Mg exchange reactions of interest in the correlation diagram of Fig. 5.30. As expected, the ΔH°_r and ΔS°_r values of the K–Mg geothermometer of Giggenbach (1988) are consistent with the ΔH°_r and ΔS°_r values of

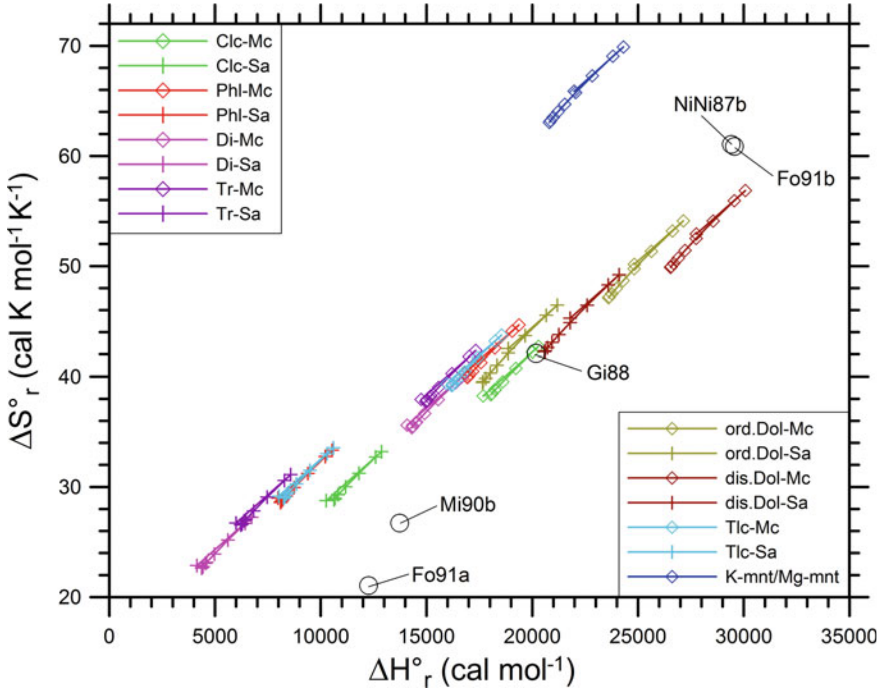

Fig. 5.30 Comparison of the temperature-independent $\Delta H°_r$ and $\Delta S°_r$ values of the empirical K–Mg geothermometers of Giggenbach (1988), Michard (1990), Fournier (1991), and that obtained from the Na–K–Mg relation of Nieva and Nieva (1987), all indicated by open black circles, with those of the K–Mg exchange reactions involving different hydrothermal minerals (see legend), computed as a function of temperature at water saturation pressures using SUPCRT92

the K–Mg exchange reaction (5.141) involving 7Å-clinochlore. However, the reactions comprising maximum-microcline together with phlogopite or talc or diopside or tremolite and those including high-sanidine and dolomite, ordered or disordered, might also control the K–Mg geothermometer of Giggenbach (1988), owing to the similar reaction entropies and the limited differences in reaction enthalpies. This finding is not surprising because of the small contributions of the different Mg-bearing solid phases to the thermodynamic properties of these exchange reactions. In contrast, the $\Delta H°_r$ and $\Delta S°_r$ values of the K–Mg geothermometer of Giggenbach (1988) are at variance with those of the reactions involving (i) K- and Mg-montmorillonites, (ii) high-sanidine together with 7Å-clinochlore or phlogopite or talc or diopside or tremolite, as well as (iii) maximum-microcline and dolomite, either disordered or ordered.

The high-slope K–Mg function of Fournier (1991), code Fo91b, and that obtained from Nieva and Nieva (1987), code NiNi87, have $\Delta H°_r$ values similar to those of the reactions including maximum-microcline and disordered dolomite, but higher $\Delta S°_r$ values. The low-slope K–Mg functions of both Michard (1990), code Mi90b, and Fournier (1991), code Fo91a, have (i) $\Delta S°_r$ values comparable with those of the exchange reactions comprising high-sanidine and diopside or tremolite, but much higher $\Delta H°_r$ values and (ii) $\Delta H°_r$ values similar to those of the exchange reactions involving high-sanidine and clinochlore, but much lower $\Delta S°_r$ values.

The $\Delta H°_r$ and $\Delta S°_r$ values of the empirical Na–Mg geothermometers, computed from their slopes and intercepts utilizing Eqs. (5.13) and (5.14), are compared with the $\Delta H°_r$ and $\Delta S°_r$ values of the considered Na–Mg exchange reactions in the binary diagram of Fig. 5.31. The low-slope Na–Mg functions of Michard (1990), code Mi90b, and Fournier (1991), code Fo91a, are at variance with all the considered exchange reactions. The high-slope Na–Mg function of Fournier (1991), code Fo91b, and the Na–Mg geothermometer obtained from the Na–K–Mg relation of Nieva and Nieva (1987), code NiNi87, have $\Delta H°_r$ and $\Delta S°_r$ values relatively similar to those of the reactions including maximum-microcline or high-sanidine and dolomite, either disordered or ordered.

The Na–Mg geothermometers derived from the K–Mg geothermometer of Giggenbach (1988) and different Na–K geothermometers distribute in the following two groups:

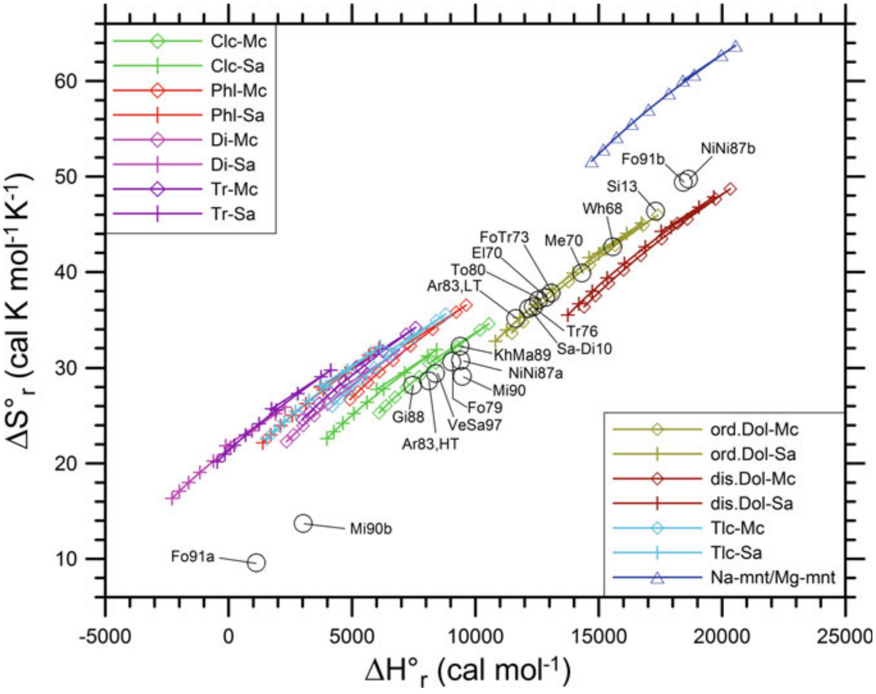

Fig. 5.31 Comparison of the temperature-independent $\Delta H°_r$ and $\Delta S°_r$ values of the empirical Na–Mg geothermometers (open black circles) with those of the Na–Mg exchange reactions involving different hydrothermal minerals, computed as a function of temperature at water saturation pressures using SUPCRT92

(i) Those related to the Na–K geothermometers of high slope (Fournier 1979; high-temperature function of Arnórsson et al., 1983a; Nieva and Nieva 1987; Kharaka and Mariner 1989; Giggenbach 1988; Michard 1990; Verma and Santoyo 1997) are consistent with the Na–Mg exchange reaction involving 7Å-clinochlore together with maximum-microcline or high-sanidine. The exchange reactions including phlogopite, diopside, talc, and tremolite have similar entropies but somewhat lower enthalpies.

(ii) Those linked to the Na–K geothermometers of low slope (White 1968; Ellis 1970; Mercado 1970; Fournier and Truesdell 1973; Truesdell 1976; Tonani 1980; low-temperature function of Arnórsson et al., 1983a; Santoyo and Díaz-González 2010; Simmons 2013) are consistent with the Na–Mg exchange reaction comprising ordered dolomite together with maximum-microcline or high-sanidine. The exchange reactions including disordered dolomite have comparable entropies and weakly higher enthalpies.

The $\Delta H°_r$ and $\Delta S°_r$ values of the reactions involving Na– and Mg-montmorillonites are at variance with those of all the Na–Mg geothermometers.

All in all, the K–Mg and Na–Mg geothermometers might be controlled by exchange reactions involving chlorites, as proposed by Giggenbach (1988), but the possible governing role of several other Mg-bearing solid phases cannot be excluded.

5.6.3 The Na–K–Mg$^{0.5}$ Triangular Diagram

Combining the fast-responding K–Mg geothermometer with the slowly re-equilibrating Na–K geothermometer by means of a triangular plot, Giggenbach (1988) suggested a graphical method (Fig. 5.32) to assess the degree of attainment of water-rock equilibrium.

In this Na–K–Mg$^{1/2}$ triangular diagram, the Na–K and K–Mg systems are represented by two sets of lines of constant Na/K and K/Mg$^{1/2}$ ratios, radiating from the Mg$^{1/2}$ and Na vertices, respectively. Since at each value of the Na/K and K/Mg$^{1/2}$ ratios corresponds a unique temperature value, each of these lines is an isotherm. The intersection points of the Na–K and K–Mg isotherms referring to the same temperature delineate the so-called "full equilibrium" curve comprising the compositions of waters in equilibrium with the mineral phases controlling both geothermometers.

The compositions of waters generated through isochemical dissolution of average crustal rocks, also shown in this triangular plot, delineate a rock dissolution area, which is far away from the full equilibrium curve.

Neutral chloride reservoir liquids encountered by deep geothermal wells generally plot along or close to the full equilibrium curve, at temperatures slightly higher than those physically measured in these wells. Corresponding neutral chloride spring waters generally plot in the field of partially equilibrated waters, being found below the full equilibrium curve and somewhat shifted towards the Mg$^{1/2}$ vertex. This might

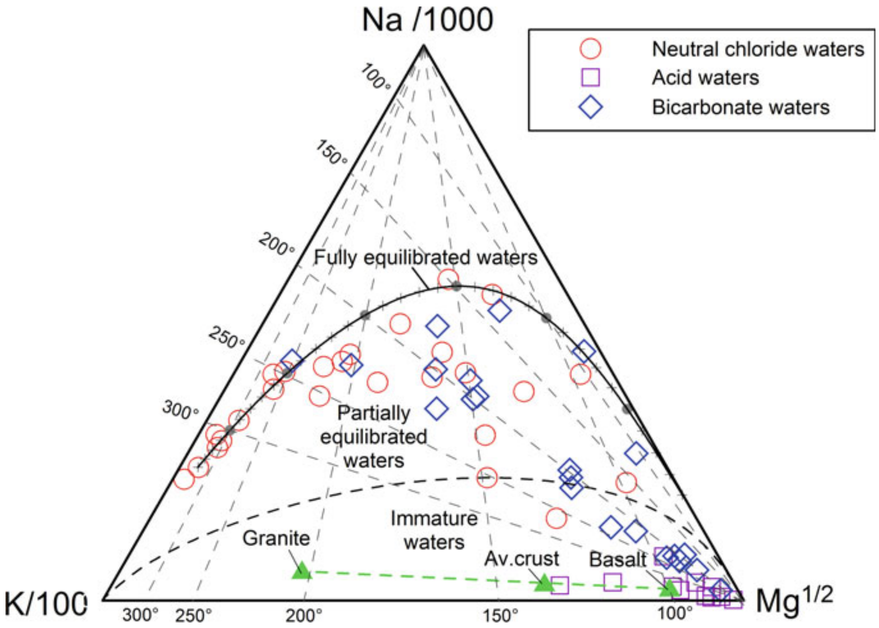

Fig. 5.32 Na–K–Mg$^{1/2}$ triangular diagram (modified from Giggenbach 1988) showing different types of geothermal waters (see legend), the compositions expected for rock dissolution (green closed triangles), the line of fully equilibrated waters, and the fields of both partially equilibrated waters and immature waters

be due to either Mg acquisition upon cooling, proceeding faster than Na acquisition, or to mixing of thermal waters with Mg-rich cold shallow waters.

Also some bicarbonate waters attain partial equilibrium, whereas other bicarbonate waters and the acid waters are situated close to the Mg$^{1/2}$ vertex. These are the so-called “immature waters”, which provide unreliable Na–K temperatures, whereas their K–Mg temperatures may still be valid, at least for not too acid aqueous solutions.

This Na–K–Mg$^{1/2}$ plot has become very popular in geochemical investigations because it allows: (i) the immediate distinction between waters suitable or unsuitable for the application of ionic solute geothermometers, (ii) the assessment of deep equilibrium temperatures, and (iii) the straightforward evaluation of re-equilibration and/or mixing effects on a large number of water samples.

However, as already pointed out by Fournier (1991), some words of caution are needed, because different full equilibrium curves can be defined based on distinct Na–K and K–Mg geothermometric functions. As shown in the Na–K–Mg$^{1/2}$ triangular diagram of Fig. 5.33, these full equilibrium curves occupy a large part of the field of the waters in partial equilibrium defined by Giggenbach (1988) and some of them extend in the field of the immature waters towards the Mg$^{1/2}$ vertex. The consequence of this spread of full equilibrium curves is that a given water may be assumed to be either in full equilibrium or in partial equilibrium or even immature, depending

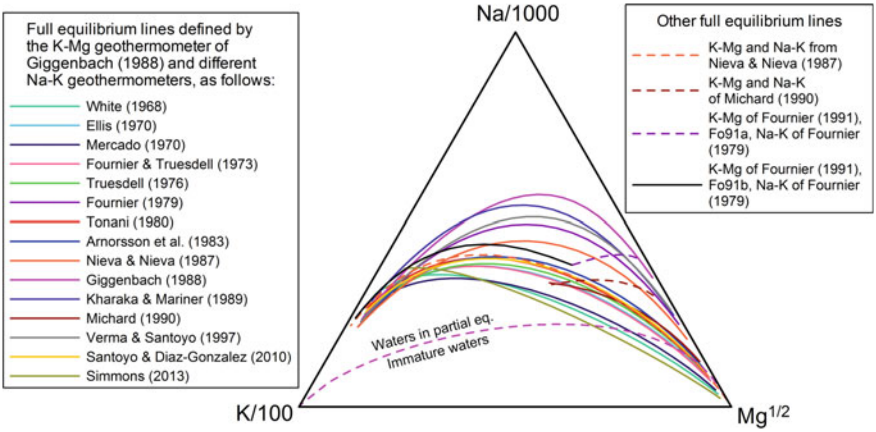

Fig. 5.33 Na–K–$Mg^{1/2}$ triangular diagram showing different "full equilibrium" curves defined by various Na–K and K–Mg geothermometers (see legend) as well as the line separating the field of the waters in partial equilibrium from the field of the immature waters, according to Giggenbach (1988)

on the Na–K and K–Mg of reference, as already pointed out by Fournier (1991). Alternatively, assuming that all the curves are actually representative of the full equilibrium conditions, the Na–K–$Mg^{1/2}$ triangular diagram of Fig. 5.33 suggests that a different approach to Na–K–Mg geothermometry is probably needed.

5.7 Other Ionic Solute Geothermometers

5.7.1 The Li-Based Geothermometers

Fouillac and Michard (1981) proposed two empirical Na–Li geothermometers calibrated considering a large number of geothermal waters. One relation applies to the waters with Cl < 0.2 M:

$$\mathrm{T} = \frac{1000}{\log(m_{\mathrm{Na}} / m_{\mathrm{Li}}) + 0.38} - 273.15. \tag{5.184}$$

The other equation is valid for Cl > 0.3 M:

$$\mathrm{T} = \frac{1195}{\log(m_{\mathrm{Na}} / m_{\mathrm{Li}}) - 0.19} - 273.15. \tag{5.185}$$

Fouillac and Michard (1981) identified also the following two functions relating temperature and Li molality:

$$T = \frac{2258}{1.44 - \log m_{\mathrm{Li}}} - 273.15 \quad \text{for Cl} < 0.2\text{M} \tag{5.186}$$

$$T = \frac{1436}{0.61 - \log m_{\mathrm{Li}}} - 273.15. \quad \text{for Cl} > 0.3\text{M} \tag{5.187}$$

More or less at the same time, a Na–Li geothermometer was also developed by Kharaka and coworkers (Kharaka et al. 1982; concentrations C_i in mg/L)

$$T = \frac{1590}{\log(c_{\mathrm{Na}} \big/ c_{\mathrm{Li}}) + 0.779} - 273.15. \tag{5.188}$$

Considering the chemical characteristics of thermal waters interacting with granitic rocks at temperatures <150 °C, Michard (1990) derived another Li–Na geothermometer:

$$T = \frac{1040}{\log(m_{\mathrm{Na}} \big/ m_{\mathrm{Li}}) + 0.43} - 273.15 \tag{5.189}$$

which is similar to Eq. (5.184).

Kharaka and coworkers assumed that the Mg-to-Li ratio may be a sensitive indicator of temperature because of both the decrease of Mg concentration with increasing temperature and the concurrent increase of Li concentration. Based on these premises, Kharaka et al. (1985) developed an Mg–Li geothermometer that can be applied up to 350 °C (concentrations C_i in mg/L):

$$T = \frac{1900}{\log(c_{\mathrm{Mg}}^{0.5} \big/ c_{\mathrm{Li}}) + 4.67} - 273.15. \tag{5.190}$$

The use of the $c_{\mathrm{Mg}}^{0.5} \big/ c_{\mathrm{Li}}$ ratio for water geothermometry was reconsidered by Kharaka and Mariner (1989) who derived two Mg–Li geothermometers (concentrations C_i in mg/L). One was calibrated using the whole database and applies up to 350 °C:

$$T = \frac{2200}{\log(c_{\mathrm{Mg}}^{0.5} \big/ c_{\mathrm{Li}}) + 5.47} - 273.15. \tag{5.191}$$

The other was calibrated utilizing oil-field waters alone and is similar to Eq. (5.190):

$$T = \frac{1910}{\log(c_{\mathrm{Mg}}^{0.5} \big/ c_{\mathrm{Li}}) + 4.63} - 273.15. \tag{5.192}$$

In our opinion, lithium geothermometers should be used with caution for at least two reasons. One is that lithium has virtually conservative (mobile) behavior in geothermal systems, although it may be incorporated into secondary quartz and chlorite, as found by Goguel (1983). In fact, owing to the conservative behavior of lithium, Giggenbach (1991) suggested to use it as tracer, together with rubidium and cesium and/or together with boron and chloride, to investigate the origin of geothermal fluids.

The second reason is that even admitting that Li has compatible behavior and its activity is therefore fixed by equilibrium with an unspecified solid solution[10], the Li content of this unspecified solid solution is expected to be small and highly variable from system to system and even within different portions of the same system. Therefore, the activity of the Li-endmember in the solid solution taking part to the exchange reactions supposedly governing the Na–Li and Mg–Li geothermometers cannot be properly constrained.

Actually, Fouillac and Michard (1981) recognized that "*it is unlikely that the Li temperature relationship is related to a chemical equilibrium between water and a lithium mineral. Lithium minerals seem to be very rare in hydrothermal environments.* In fact, they considered that "*lithium behaves in hot waters as a "soluble" element, i.e. it is not co-precipitated with any secondary mineral, except perhaps near-surface clays.*" Fouillac and Michard (1981) attributed the temperature—lithium relation to the increase in rock dissolution with increasing temperature coupled with the uptake of lithium in weathering products, such as clay minerals.

Accepting these explanations of Fouillac and Michard (1981), it follows that the development of a Na–Li geothermometer on a thermodynamic basis, by referring to a suitable exchange reaction, is meaningless. Therefore, Li-based geothermometers will not be considered any further in this work.

5.7.2 The "Auxiliary Geothermometers" of Michard (1990)

In addition to the Na–K, Ca–K, Mg–K, and Na–Li geothermometers which have been already discussed above, Michard (1990) calibrated other "auxiliary geothermometers" involving the Rb/Na, Cs/Na, Sr/K^2, Fe/K^2, and Mn/K^2 ratios as well as the F·K and $W{\cdot}K^2$ products for waters interacting with granitic rocks at temperatures lower than 150 °C. Michard (1990) suggested that these auxiliary geothermometers could be alternatively used to compute the concentrations of Rb, Cs, Sr, Fe, Mn, F, and W, for known temperature and concentrations of Na and K. However, Michard (1990) recognized that regional variations can be important for trace alkali elements, i.e., Li, Rb, and Cs. "*As these elements are governed by partition processes and not by equilibria with different solid phases, regional variations must be related to variations in the trace elements content of the granite.*" Similar to the Li-based geothermometers,

---

[10] We recall that the term compatible indicates the components whose solubility is limited by incorporation in authigenic minerals (Arnórsson et al. 1983b).

also those involving Rb, Cs, Sr, Fe, Mn, and W, will not be considered any further in this work. Discussion of F-based geoindicators will be resumed in the next section.

5.7.3 *The Ca–Mg and SO_4–F Theoretical Geothermometers for Thermal Waters from Carbonate-Evaporite Reservoirs*

Marini et al. (1986) proposed a Ca–Mg geothermometer and a SO_4–F geothermometer specific for waters coming from carbonate-evaporite aquifers. Both geothermometers were calibrated using the thermodynamic data of suitably selected exchange reactions. The Ca–Mg geothermometer is based on the exchange reaction involving calcite and dolomite:

$$2CaCO_3 + Mg^{2+} = CaMg(CO_3)_2 + Ca^{2+} \tag{5.193}$$

whereas the SO_4–F geothermometer is constrained by the exchange reaction between anhydrite and fluorite:

$$CaSO_4 + 2F^- = CaF_2 + SO_4^{2-}. \tag{5.194}$$

The thermodynamic equilibrium constant of reactions (5.193) and (5.194) are nearly equal to the free ion molality ratios $m_{Ca^{2+}} \big/ m_{Mg^{2+}}$ and $m_{SO_4^{2-}} \Big/ m^2_{F^-}$, respectively, assuming that the solid phases are pure, the activity coefficients of Ca^{2+} and Mg^{2+} ions cancel out, and the activity coefficient of ${SO_4}^{2-}$ ion is nearly equal to the squared activity coefficient of F^- ion.

A major problem in the application of the Ca–Mg geothermometer is the variable degree of order-disorder of dolomite, as discussed by several authors (e.g., Marini et al. 1986; Chiodini et al. 1995; Hyeong and Capuano 2001; Zhiqian et al. 2007; Vespasiano et al. 2014; Blasco et al. 2018, 2019).

Another major problem is caused by ion complexing (Guidi et al. 1990). In fact, due to the formation of ion pairs of Ca^{2+} ion (e.g., ${CaSO_4}^\circ$, ${CaCO_3}^\circ$, ${CaHCO_3}^+$, $CaCl^+$, ${CaCl_2}^\circ$, and CaF^+) and Mg^{2+} ion (e.g., ${MgSO_4}^\circ$, ${MgCO_3}^\circ$, ${MgHCO_3}^+$, $MgCl^+$, and MgF^+), the total molality ratio $m_{Ca} \big/ m_{Mg}$ deviates significantly from the free ion molality ratio $m_{Ca^{2+}} \big/ m_{Mg^{2+}}$ especially in Cl-poor solutions. Similarly, owing to the formation of ion complexes of ${SO_4}^{2-}$ ion (e.g., ${NaSO_4}^-$, ${KSO_4}^-$, ${KHSO_4}^\circ$, ${CaSO_4}^\circ$, and ${MgSO_4}^\circ$) and F^- ion (e.g., NaF°, CaF^+, and MgF^+), the total molality ratio $m_{SO_4} \big/ m^2_F$ departs considerably from the free ion molality ratio $m_{SO_4^{2-}} \Big/ m^2_{F^-}$, especially in Cl-rich solutions.

To eliminate the impact of ion complexing, the Ca–Mg and SO_4–F geothermometers and other theoretical geoindicators were recalibrated by Chiodini et al. (1995) for waters coming from carbonate-evaporite aquifers of medium-low temperature

Table 5.6 Theoretical geoindicators for aqueous solutions coming from carbonate-evaporite aquifers of medium-low temperature (50–150 °C; from Chiodini et al. 1995)

$\mathrm{pH} = 6.268 - 0.5564 \cdot \log \mathrm{P_{CO_2}} - 98.77/\mathrm{T} - 0.0005 \cdot \log \Sigma_{\mathrm{eq}}$	(5.195)
$\log m_{\mathrm{Ca}} = -3.809 + 727.29/\mathrm{T} + 0.1279 \cdot \log \mathrm{P_{CO_2}} + 0.2097 \cdot \log \Sigma_{\mathrm{eq}}$	(5.196)
$\log m_{\mathrm{Mg}} = -6.926 + 1707.1/\mathrm{T} + 0.0888 \cdot \log \mathrm{P_{CO_2}} + 0.1397 \cdot \log \Sigma_{\mathrm{eq}}$	(5.197)
$\log m_{\mathrm{HCO_3}} = -4.819 + 0.4570 \cdot \log \mathrm{P_{CO_2}} + 970.29/\mathrm{T} + 0.07323 \cdot \log \Sigma_{\mathrm{eq}}$	(5.198)
$\log m_{\mathrm{SO_4}} = -4.832 + 1145.9/\mathrm{T} + 0.3118 \cdot \log \Sigma_{\mathrm{eq}} - 0.07306 \cdot \log \mathrm{P_{CO_2}}$	(5.199)
$\log m_{\mathrm{F}} = -2.805 - 325.9/\mathrm{T} + 0.1127 \cdot \log \Sigma_{\mathrm{eq}} - 0.02174 \cdot \log \mathrm{P_{CO_2}}$	(5.200)
$\log \left(m_{\mathrm{Ca}} / m_{\mathrm{Mg}}\right) = 3.117 - 979.8/\mathrm{T} + 0.03904 \cdot \log \mathrm{P_{CO_2}} + 0.07003 \cdot \log \Sigma_{\mathrm{eq}}$	(5.201)
$\log \left(m_{\mathrm{HCO_3}} / m_{\mathrm{F}}\right) = -2.014 + 0.4787 \cdot \log \mathrm{P_{CO_2}} + 1296.2/\mathrm{T} - 0.03943 \cdot \log \Sigma_{\mathrm{eq}}$	(5.202)
$\log \left(m_{\mathrm{SO_4}} / m_{\mathrm{F}}^2\right) = -0.7782 + 1797.7/\mathrm{T} + 0.08653 \cdot \log \Sigma_{\mathrm{eq}} - 0.02963 \cdot \log \mathrm{P_{CO_2}}$	(5.203)
$\log \left(m_{\mathrm{HCO_3}}^2 / m_{\mathrm{SO_4}}\right) = -4.807 + 0.9871 \cdot \log \mathrm{P_{CO_2}} + 794.8/\mathrm{T} - 0.1655 \cdot \log \Sigma_{\mathrm{eq}}$	(5.204)

(50–150 °C). First, the total concentrations of Ca, Mg, SO_4, F, and HCO_3 were computed for aqueous solutions in equilibrium with calcite, disordered dolomite[11], anhydrite, and fluorite at temperatures between 0 and 150 °C, P_{CO_2} in the 0.1 to 100 bar range, and total concentrations of conservative components, Na and Cl, varying between 0.0001 and 0.3 mol/kg. These calculations were performed using the mineral-solution equilibrium model of Guidi et al. (1990) and Chiodini et al. (1991), representing the subject of the next section. Second, a stepwise multiple regression analysis was performed to describe the dependence of the total concentration of each chemical component and relevant concentration ratios upon 1/T(K), log P_{CO_2} and log Σ_{eq} (Σ_{eq} is total ionic salinity in eq/kg). The obtained theoretical geoindicators are reported in Table 5.6, indicating that: (i) the concentrations of Ca, Mg, SO_4, and F as well as the $SO_4/(F)^2$ and Ca/Mg ratios depend mainly on temperature and, therefore, can be used to formulate geothermometers, (ii) the $(HCO_3)^2/SO_4$ ratio and pH are mainly controlled by P_{CO_2} and, consequently, can be utilized as basis for P_{CO_2}-indicators (iii) the HCO_3/F ratio and HCO_3 concentrations are functions of both P_{CO_2} and temperature.

More recently, Vespasiano et al. (2014) developed geothermometric functions specific for the thermal aquifers discharging at the Luigiane Spa, near Guardia Piemontese (Calabria, Italy). These thermal aquifers are hosted in carbonate-evaporite rocks affected by low-grade metamorphic processes, which are presumably responsible of the order-disorder state of dolomite. The Ca–Mg and SO_4–F geothermometric functions obtained for these waters are (concentrations c_i in mg/kg):

$$\mathrm{T(K)} = \frac{896.8}{3.408 - \log\left(c_{\mathrm{Ca}} / c_{\mathrm{Mg}}\right)} - 273.15 \qquad (5.205)$$

---

[11] Disordered dolomite was considered because ordered dolomite provided results at variance with the analytical data of the thermal springs of Central Italy considered by Chiodini et al. (1995).

$$T(K) = \frac{1700.4}{\log(c_{SO_4} / c_F^2) + 3.171} - 273.15. \tag{5.206}$$

Summing up, the studies on the geothermometry of thermal waters coming from carbonate-evaporite aquifers have stimulated the investigation of the ion complexing influence on geothermometers and P_{CO_2}-indicators, which is further considered in the next section.

5.8 The Influence of Ion Complexing on Geothermometers and f_{CO_2}-Indicators

5.8.1 Theoretical Approach

The concentrations of compatible dissolved components can be predicted specifying the identity of the minerals presumably in equilibrium with the aqueous solution (one mineral for each compatible component) as well as the temperature and the concentration of chloride and other conservative components, if any. The predictability of the concentrations of compatible dissolved components was recognized by several studies, such as those of Shikazono (1978), Michard et al. (1981), and Arnórsson et al. (1983b).

Building on the outcomes of these studies, Guidi et al. (1990) and Chiodini et al. (1991) investigated the influence of ion complexing on geothermometers and f_{CO_2}-indicators using a mineral-solution equilibrium model which has the same computational structure of the model adopted by Michard et al. (1981). The following aqueous species are considered in the model: $H_2O°$, H^+, OH^-, Na^+, $NaCl°$, $NaSO_4{}^-$, $NaCO_3{}^-$, $NaF°$, $NaOH°$, K^+, $KCl°$, $KSO_4{}^-$, $KHSO_4°$, Ca^{2+}, $CaSO_4°$, $CaCO_3°$, $CaHCO_3{}^+$, CaF^+, $CaOH^+$, Mg^{2+}, $MgSO_4°$, $MgCO_3°$, $MgHCO_3{}^+$, MgF^+, $MgOH^+$, $H_2CO_3°$, $HCO_3{}^-$, $CO_3{}^{2-}$, $SO_4{}^{2-}$, F^-, Cl^-, $H_4SiO_4°$, $H_3SiO_4{}^-$, $Al(OH)_4^-$, Al^{3+}, $Al(OH)^{2+}$, $Al(OH)_2^+$. The model finds the roots of a polynomial equation of H^+ activity, which is obtained considering: the electroneutrality equation, the thermodynamic constant of the dissolution reactions of relevant mineral phases and gaseous CO_2, and the thermodynamic constant of the dissociation reactions of complex aqueous species. In the light of the available information on high-temperature geothermal systems:

(i) Na^+, K^+, Ca^{2+}, Mg^{2+}, $Al(OH)_4^-$, $H_4SiO_4°$, $SO_4{}^{2-}$, F^-, and $HCO_3{}^-$ were chosen as compatible dissolved components of interest, whereas only Cl^- was taken into account among conservative constituents.

(ii) The hydrothermal mineral assemblage was assumed to be made up of low-albite, K-feldspar, either a Ca–Al-silicate[12] and/or calcite, depending on the

---

[12] Laumontite up to 200 °C, clinozoisite in the 200–280 °C interval, and wairakite at higher temperatures.

f_{CO_2} computed by Eq. (5.137), clinochlore, muscovite, quartz, anhydrite, and fluorite.

(iii) In general, f_{CO_2} was considered an externally controlled parameter fixing the activity of HCO_3^- ion, apart from the cases of Ca–Al-silicate/calcite coexistence. In these particular cases, f_{CO_2} is fixed by temperature, calcite governs the activity of HCO_3^- ion, and the Ca–Al-silicate controls the activity of Ca^{2+} ion.

The composition of the aqueous solution was computed at temperatures ranging from 150 to 300 °C, at steps of 50 °C, f_{CO_2} varying from 0.1 to 100 bar, every half log-unit, and total chloride molality from 0.0003 to 1, every half log-unit. Calculated total concentrations are in satisfactory agreement with those observed in different high-temperature geothermal systems.

Then, the logarithms of total concentrations of compatible constituents and their log-ratios were treated as dependent variables in multiple stepwise regression analysis, in which 1/T(K), log f_{CO_2} and log Σ_{eq} (Σ_{eq} is total ionic salinity in eq/kg) were adopted as independent variables.

5.8.2 Complexing in Hydrothermal Aqueous Solutions and Related Effects

To simplify the discussion, in this section, we examine only the chemical speciation of a hydrothermal aqueous solution in equilibrium with low-albite, maximum-microcline, clinozoisite, calcite, 7 Å-clinochlore, muscovite, quartz, anhydrite, and fluorite at temperature of 250 °C, CO_2 fugacity fixed by coexistence of calcite and clinozoisite, and total Cl concentration varying from 0.003 to 3 mol/kg.

We have performed a new series of calculations by means of the computer code EQ3NR, version 7.2b (Wolery 1992). Reference was made to the COM thermodynamic database, which includes a large number of solid, aqueous, and gaseous species, whose thermodynamic properties are mostly derived from SUPCRT92 (Johnson et al. 1992 and references therein). The aqueous species considered in speciation computations are listed in Table 5.7. In spite of some differences in the considered aqueous species and in some thermodynamic data, results are comparable with those of Guidi et al. (1990) and Chiodini et al. (1991).

As discussed by Guidi et al. (1990) and Chiodini et al. (1991), ion association in hydrothermal aqueous solutions has different effects on dissolved components, mainly depending on the charge of relevant ions, as summarized below.

Sodium and potassium (Fig. 5.34). Although the concentrations of the Cl complexes $NaCl_{(aq)}$ and $KCl_{(aq)}$ increase with total Cl molality, the free ions Na^+ and K^+ are always the dominant species of dissolved sodium and potassium. Therefore, total (analyzed) Na and K concentrations are always representative of the concentrations of free ions.

Magnesium and calcium (Fig. 5.35). The free ion Ca^{2+} is the dominant species for

Table 5.7 Aqueous species considered in speciation computations

	Al^{3+}	Ca^{2+}	H^+	HCO_3^-	K^+	Mg^{2+}	Na^+
F^-	$Al(OH)_2^+$	$CaCO_{3(aq)}$	$HCl_{(aq)}$	$CO_{2(aq)}$	$KCl_{(aq)}$	$MgCO_{3(aq)}$	$NaAlO_{2(aq)}$
Cl^-	AlO_2^-	$CaCl^+$	$HF_{(aq)}$	CO_3^{2-}	$KHSO_{4(aq)}$	$MgCl^+$	$NaCO_3^-$
SO_4^{2-}	$HAlO_{2(aq)}$	$CaCl_{2(aq)}$	HF_2^-		KSO_4^-	MgF^+	$NaCl_{(aq)}$
$SiO_{2(aq)}$		CaF^+	HSO_4^-			$MgHCO_3^+$	$NaF_{(aq)}$
OH^-		$CaHCO_3^+$	$HSiO_3^-$			$MgSO_{4(aq)}$	$NaHCO_{3(aq)}$
		$CaSO_{4(aq)}$					$NaHSiO_{3(aq)}$
							$NaOH_{(aq)}$

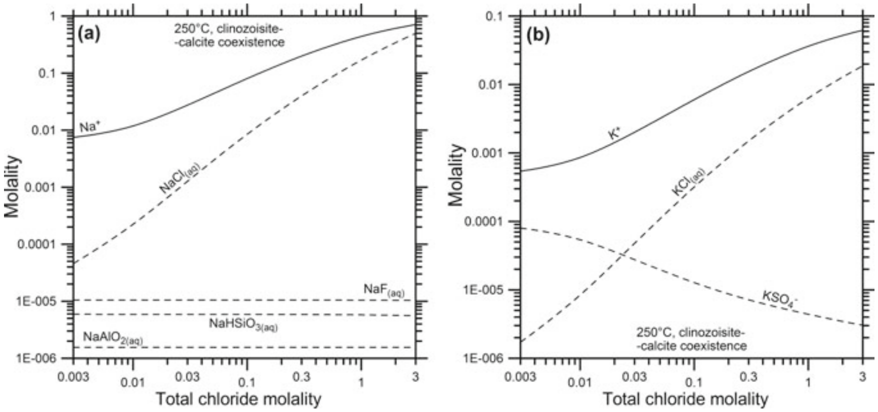

Fig. 5.34 Distribution of dissolved species of **a** sodium and **b** potassium in a hydrothermal aqueous solution in equilibrium with low-albite, maximum-microcline, clinozoisite, calcite, 7Å-clinochlore, muscovite, quartz, anhydrite, and fluorite at 250 °C as a function of total Cl molality

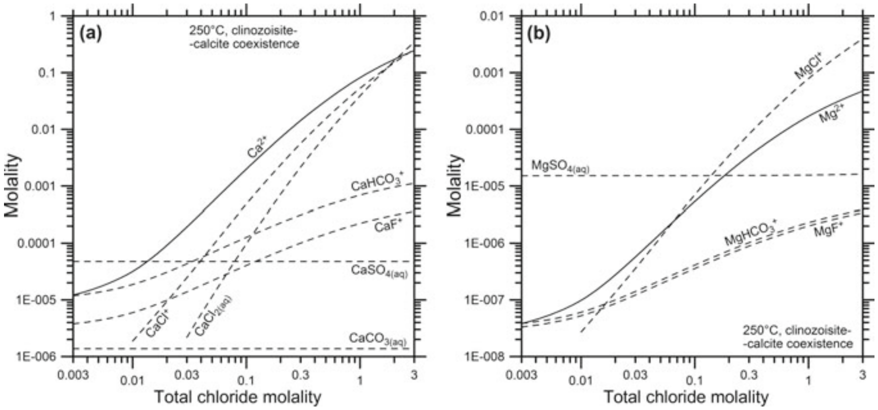

Fig. 5.35 Distribution of dissolved species of **a** calcium and **b** magnesium in a hydrothermal aqueous solution in equilibrium with low-albite, maximum-microcline, clinozoisite, calcite, 7Å-clinochlore, muscovite, quartz, anhydrite, and fluorite at 250 °C as a function of total Cl molality

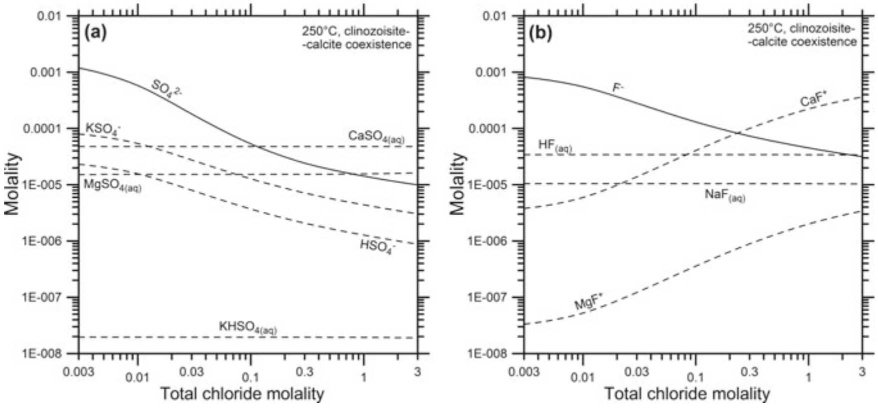

Fig. 5.36 Distribution of dissolved species of (a) sulfate and (b) fluoride in a hydrothermal aqueous solution in equilibrium with low-albite, maximum-microcline, clinozoisite, calcite, 7Å-clinochlore, muscovite, quartz, anhydrite, and fluorite at 250 °C as a function of total Cl molality

total Cl concentrations higher than 0.012 mol/kg and lower than 2 mol/kg, that is in the range 425–70,900 mg/kg. The Cl complexes $CaCl_2°$ and $CaCl^+$ dominate at high total Cl concentrations. In contrast, the $CaSO_4°$ ion pair prevails over other Ca-species at low total Cl concentrations. The free ion Mg^{2+} is never the main dissolved Mg species, because the $MgSO_4°$ aqueous complex dominates at total Cl concentrations lower than 0.13 mol/kg (4600 mg/kg) and the $MgCl^+$ ion pair prevails in Cl-rich solutions. Nevertheless, the relative proportion of Mg^{2+} ion increases with total Cl molality.

Sulfate and fluoride (Fig. 5.36). Free ions SO_4^{2-} and F^- are the prevailing species at total Cl concentrations lower than 0.1 mol/kg (3500 mg/kg) and 0.25 mol/kg (8900 mg/kg), respectively, while the $CaSO_4°$ and CaF^+ ion pairs are the dominant species at total Cl molalities higher than these values. Therefore total (analyzed) sulfate and fluoride concentrations are representative of the concentrations of free ions only at total Cl concentrations lower than 0.1 mol/kg (3500 mg/kg) and 0.25 mol/kg (8900 mg/kg), respectively.

Carbonate species (Fig. 5.37a). The main dissolved carbonate species is aqueous CO_2 (or carbonic acid, H_2CO_3) at all total Cl molalities. Similar to what has been observed for sulfate and fluoride, free HCO_3^- ion is the main carbonate species at total Cl concentrations lower than 0.18 mol/kg (6400 mg/kg), whereas the ion complex $CaHCO_3^+$ prevails at total Cl molalities above this value.

Proton donors and proton (Fig. 5.37b). Bicarbonate is the main acid (proton donor) at all total Cl molalities. The concentration of H^+ ion increases by almost 2 orders of magnitude with increasing total Cl concentrations, from 0.22 μmol/kg at total Cl concentration of 0.003 mol/kg to 13 μmol/kg at total Cl concentration of 3 mol/kg. Proton concentration is buffered by coexistence of aluminum-silicate minerals as already pointed out by Ellis (1970). For, instance, referring to the simplified system albite-muscovite-quartz-aqueous solution, if the concentration of Cl^-

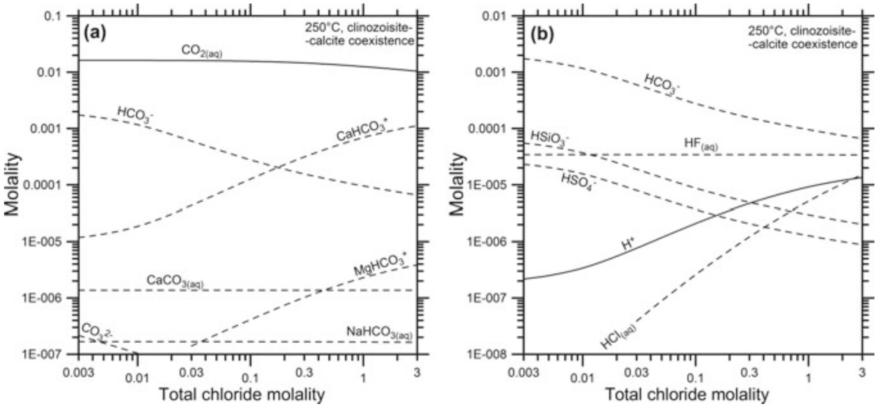

Fig. 5.37 Distribution of **a** carbonate species and **b** proton donors and H^+ in a hydrothermal aqueous solution in equilibrium with low-albite, maximum-microcline, clinozoisite, calcite, 7Å-clinochlore, muscovite, quartz, anhydrite, and fluorite at 250 °C as a function of total Cl molality

ion increases, the concentrations of Na^+ and K^+ ions have to increase accordingly, to maintain the electroneutrality condition. In turn, this increment in alkali concentrations determines an increase in H^+ molality owing to the equilibrium constraint dictated by the following reaction:

$$3\,\text{albite} + K^+ + 2H^+ = \text{muscovite} + 6\,\text{quartz} + 3Na^+. \tag{5.207}$$

Effects of ion complexing. Due to the effects of ion complexing, total (analytical) molalities of compatible cations (Na^+, K^+, Ca^{2+} and Mg^{2+}) and compatible anions ($SO_4{}^{2-}$, F^-, and $HCO_3{}^-$) diverge, to variable extents, from the molalities of free ions, which are uniquely fixed by mineral-solution equilibrium, at a given temperature or a given temperature, f_{CO_2} condition.

The ratios of total molalities exhibit variable deviations from the corresponding ratios of free ion activities, which are uniquely fixed by temperature. These effects are minor on the Na/K ratio because the total (analyzed) concentrations of both Na and K are representative of free ion concentrations, at all T–f_{CO_2}–Cl conditions (see above), and activity coefficients of Na^+ and K^+ ions are similar (Fig. 5.38a).

In contrast, the K^2/Mg total molality ratio deviates strongly from the free ion activity ratio (Fig. 5.38b), due to the differences in the speciation of K, which is dominated by free K^+ ion all T–f_{CO_2}–Cl conditions, and Mg, which is controlled by SO_4 and Cl complexes while the free Mg^{2+} ion is always present in lower concentrations (see above). The deviations of the total molality ratio from the free ion activity ratio are particularly important at low total Cl molality where the ion complexing effects are extremely important on Mg.

Also the K^2/Ca and Na^2/Ca total molality ratios exhibit considerable deviations from the corresponding free ion activity ratios (Fig. 5.39), because ion complexing is

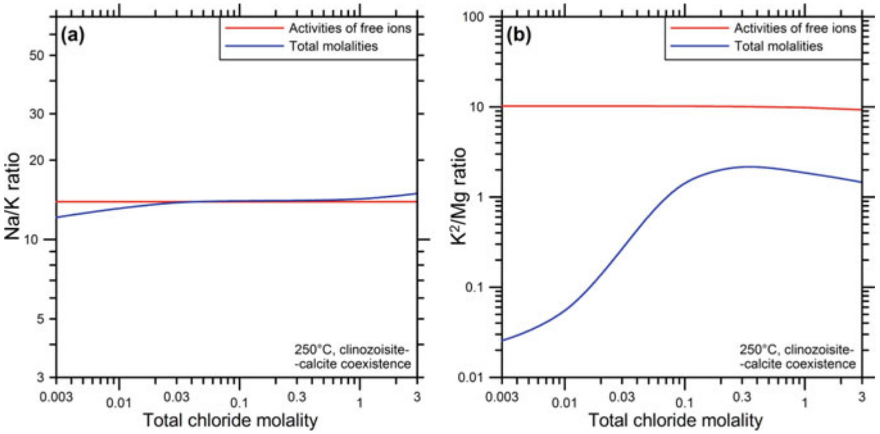

Fig. 5.38 Log-log diagrams of **a** Na/K and **b** K^2/Mg total molality ratios and free ion activity ratios as a function of total Cl molality in a hydrothermal aqueous solution in equilibrium with low-albite, maximum-microcline, clinozoisite, calcite, 7Å-clinochlore, muscovite, quartz, anhydrite, and fluorite at 250 °C

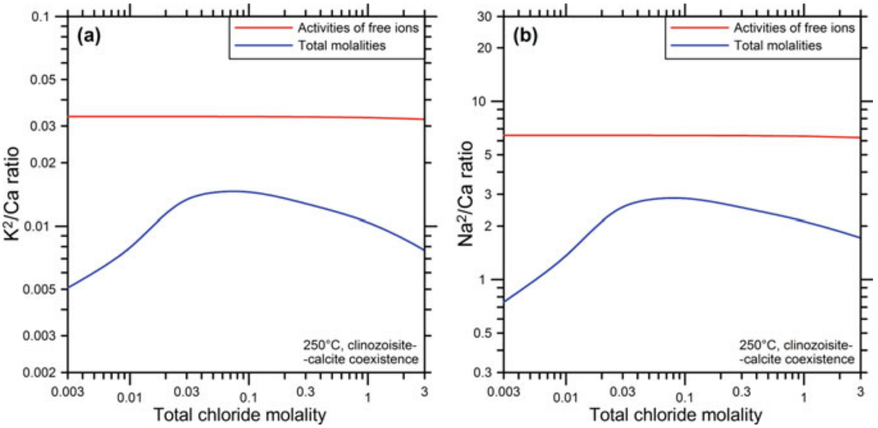

Fig. 5.39 Log-log diagrams of **a** K^2/Ca and **b** Na^2/Ca total molality ratios and free ion activity ratios as a function of total Cl molality in a hydrothermal aqueous solution in equilibrium with low-albite, maximum-microcline, clinozoisite, calcite, 7Å-clinochlore, muscovite, quartz, anhydrite, and fluorite at 250 °C

more important for Ca, especially at total Cl concentrations lower than 0.012 mol/kg and higher than 2 mol/kg, than for the two alkali metals (see above).

The SO$_4$/F^2 and SO$_4$/HCO$_3^2$ total molality ratios depart from the related free ion activity ratios as shown in Fig. 5.40. Nevertheless, these deviations are different from those of the ratios between mono- and bivalent cations, because SO$_4$, F, and HCO$_3$ have similar speciation, with the free ion prevailing at relatively low total Cl

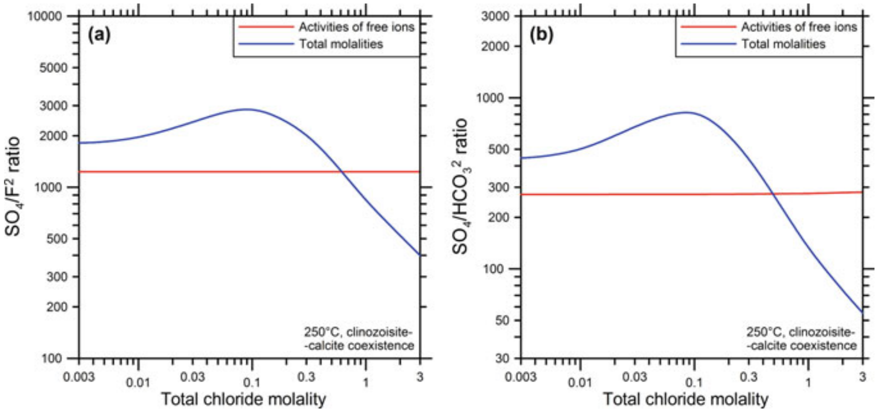

Fig. 5.40 Log-log diagrams of **a** SO_4/F^2 and **b** SO_4/HCO_3^2 total molality ratios and free ion activity ratios as a function of total Cl molality in a hydrothermal aqueous solution in equilibrium with low-albite, maximum-microcline, clinozoisite, calcite, 7Å-clinochlore, muscovite, quartz, anhydrite, and fluorite at 250 °C

molalities and the Ca-complexes dominating at comparatively high total Cl molalities (see above).

5.8.3 *The Theoretical Geoindicators of Chiodini et al. (1991)*

Chiodini et al. (1991) treated the logarithms of the total molalities of compatible components and their log-ratios as dependent variables in multiple stepwise regression analysis, in which 1/T(K), log f_{CO_2} and log Σ_{eq} were considered as independent variables. The final regression equations thus obtained, as well as a relation for pH, are reported in Tables 5.8 and 5.9.

Table 5.8 pH and logarithms of the total molalities of the compatible constituents dissolved in aqueous solutions in equilibrium with the neutral-pH hydrothermal mineral assemblage as a function of temperature, P_{CO_2} and ionic salinity (from Chiodini et al. 1991)

$\log m_{Na} = -0.527 + 0.982 \cdot \log \Sigma eq + 78.9/T + 0.0119 \cdot \log P_{CO_2}$	(5.208)
$\log m_{K} = +0.458 + 0.944 \cdot \log \Sigma eq - 1014/T + 0.0346 \cdot \log P_{CO_2}$	(5.209)
$\log m_{Ca} = -1.116 + 1.302 \cdot \log \Sigma eq - 0.390 \cdot \log P_{CO_2} - 443/T$	(5.210)
$\log m_{Mg} = -8.188 + 0.912 \cdot \log \Sigma eq + 2156/T + 0.356 \cdot \log P_{CO_2}$	(5.211)
$\log m_{HCO_3} = -10.004 + 0.904 \cdot \log P_{CO_2} + 3223/T - 0.489 \cdot \log \Sigma eq$	(5.212)
$\log m_{SO_4} = -12.503 + 4604/T + 0.501 \cdot \log P_{CO_2} - 0.626 \cdot \log \Sigma eq$	(5.213)
$\log m_{F} = -5.069 + 798/T + 0.127 \cdot \log P_{CO_2} - 0.0886 \cdot \log \Sigma eq$	(5.214)
$pH = +1.757 - 0.822 \cdot \log \Sigma eq + 1846/T - 0.0171 \cdot \log P_{CO_2}$	(5.215)

Table 5.9 Logarithms of the total molality ratios of compatible constituents dissolved in aqueous solutions in equilibrium with the neutral-pH hydrothermal mineral assemblage as a function of temperature, P_{CO_2} and ionic salinity (from Chiodini et al. 1991)

$\log(m_{Na}/m_K) = -0.985 + 1093/T + 0.0384 \cdot \log \Sigma\,eq - 0.0228 \cdot \log P_{CO_2}$	(5.216)
$\log(m_K^2/m_{Mg}) = +9.104 - 4184/T + 0.975 \cdot \log \Sigma eq - 0.286 \cdot \log P_{CO_2}$	(5.217)
$\log(m_{SO_4}/m_F^2) = -2.364 + 3007/T - 0.449 \cdot \log \Sigma eq + 0.247 \cdot \log P_{CO_2}$	(5.218)
$\log(m_K^2/m_{Ca}) = +2.031 + 0.459 \cdot \log P_{CO_2} + 0.585 \cdot \log \Sigma eq - 1584/T$	(5.219)
$\log(m_{Ca}/m_{Mg}) = +7.073 - 0.746 \cdot \log P_{CO_2} - 2600/T + 0.390 \cdot \log \Sigma eq$	(5.220)
$\log(m_{HCO_3}^2/m_{SO_4}) = -7.506 + 1.307 \cdot \log P_{CO_2} + 1843/T - 0.352 \cdot \log \Sigma eq$	(5.221)
$\log(m_{HCO_3}/m_F) = -4.935 + 0.777 \cdot \log P_{CO_2} + 2425/T - 0.401 \cdot \log \Sigma eq$	(5.222)
$\log(m_{Na}^2/m_{Mg}) = +7.134 + 1.052 \cdot \log \Sigma eq - 1999/T - 0.332 \cdot \log P_{CO_2}$	(5.223)
$\log(m_{Na}^2/m_{Ca}) = +0.061 + 0.662 \cdot \log \Sigma eq + 0.414 \cdot \log P_{CO_2} + 601/T$	(5.224)

Inspection of Tables 5.8 and 5.9 shows that:

(i) The Na/K, K^2/Mg, and SO_4/F^2 ratios as well as SO_4 and F molalities are mainly controlled by temperature and are therefore potential geothermometers.
(ii) The K^2/Ca, Ca/Mg, HCO_3/F, and $(HCO_3)^2/SO_4$ ratios as well as HCO_3 molality are largely controlled by f_{CO_2} and are therefore potential f_{CO_2}-indicators.
(iii) The Na^2/Mg and Na^2/Ca ratios, the molalities of cations, and pH are mainly constrained by total ionic salinity and are therefore less suitable, in principle, as either geothermometers or f_{CO_2}-indicators.

5.8.4 The Lesson Learned and the Way Forward

Summing up, the studies of Guidi et al. (1990) and Chiodini et al. (1991) found a theoretical justification for the ionic solute geothermometers and f_{CO_2}-indicators, which were originally derived on a purely empirical basis, and this is certainly a valuable result. The functions reported in Tables 5.8 and 5.9 can be used to investigate the behavior of each solute upon mixing and re-equilibration, as done by Marini et al. (1998) for the thermal waters of the San Marcos area, Guatemala.

However, the approach adopted by Chiodini et al. (1991), consisting in computing the speciation of fully-equilibrated geothermal aqueous solutions and processing the obtained results through multiple regression analysis with the ultimate aim to obtain geothermometers and f_{CO_2}-indicators involving the total concentrations of the compatible constituents, is probably not the best strategy. In fact, it is more correct to carry out speciation calculations on the water samples of interest obtaining the activities of the free ions of compatible constituents that are subsequently introduced into functions expressing the temperature dependence of the thermodynamic equilibrium constants of suitable exchange reactions (at water saturation pressures). In essence, the log K of these reactions are adopted as benchmarks in this second approach, which is therefore rigorous, whereas the same log K are manipulated in the first approach, a practice which leaves much to be desired, also considering that the rigmarole of multiple regression analysis introduces far from negligible approximations. Therefore, we decided to develop and investigate theoretical geothermometers and f_{CO_2}-indicators based on ion activity ratios, representing the subject of the next chapters of this book.

References

Akinfiev NN, Diamond LW (2009) A simple predictive model of quartz solubility in water–salt–CO_2 systems at temperatures up to 1000 °C and pressures up to 1000 MPa. Geochim Cosmochim Ac 73:1597–1608

Anderko A, Pitzer KS (1993) Equation-of-state representation of phase equilibria and volumetric properties of the system NaCl–H_2O above 573 K. Geochim Cosmochim Ac 57:1657–1680

Anderson G, Burnham CW (1965) The solubility of quartz in super-critical water. Am J Sci 263:494–511

Anderson GM, Burham CW (1967) Reactions of quartz and corundum with aqueous chloride and hydroxide solutions at high temperatures and pressures. Am J Sci 265:12–27

Arnórsson S (1970) Geochemical studies of thermal waters in the southern lowlands of Iceland. Geothermics 2:547–552

Arnórsson S (1975) Application of the silica geothermometer in low temperature hydrothermal areas in Iceland. Am J Sci 275:763–784

Arnórsson S (1985) The use of mixing models and chemical geothermometers for estimating underground temperatures in geothermal systems. J Volcanol Geoth Res 23:299–335

Arnórsson S (1998) Geothermal geochemistry. Historical overview, present status, future outlook. In: UNU-GTP 20th anniversary workshop, pp 179–185

Arnórsson S (2000) The quartz and Na/K geothermometers. I. New thermodynamic calibration. In: Proceedings of the world geothermal congress 2000, Kyushu-Tohoku, Japan, pp 929–934

Arnórsson S, Gunnlaugsson E (1985) New gas geothermometers for geothermal exploration—calibration and application. Geochim Cosmochim Ac 49:1307–1325

Arnórsson S, Stefánsson A (1999) Assessment of feldspar solubility constants in water in the range of 0° to 350 °C at vapor saturation pressures. Am J Sci 299:173–209

Arnórsson S, Gunnlaugsson E, Svavarsson H (1983a) The chemistry of geothermal waters in Iceland. III. Chemical geothermometry in geothermal investigations. Geochim Cosmochim Ac 47:567–577

Arnórsson S, Gunnlaugsson E, Svavarsson H (1983b) The chemistry of geothermal waters in Iceland. II. Mineral equilibria and independent variables controlling water compositions. Geochim Cosmochim Ac 47:547–566

Arnórsson S, Stefánsson A, Bjarnason JO (2007) Fluid-fluid interactions in geothermal systems. Rev Mineral Geochem 65:259–312

Azaroual M, Fouillac C, Matray JM (1997) Solubility of silica polymorphs in electrolyte solutions. II. Activity of aqueous silica and solid silica polymorphs in deep solutions from the sedimentary Paris Basin. Chem Geol 140:167–179

Bakker RJ (2003) Package FLUIDS 1. Computer programs for analysis of fluid inclusion data and for modelling bulk fluid properties. Chem Geol 194:3–23

Bayram AF (2001) Application of an artificial neural network model to a Na–K geothermometer. J Volcanol Geoth Res 112:75–81

Benjamin T, Charles R, Vidale R (1983) Thermodynamic parameters and experimental data for the Na–K–Ca geothermometer. J Volcanol Geoth Res 15:167–186

Bird DK, Helgeson HC (1981) Chemical interaction of aqueous solutions with epidote-feldspar mineral assemblages in geologic systems. II. Equilibrium constraints in metamorphic/geothermal processes. Am J Sci 281:576–614

Bird DK, Norton DL (1981) Theoretical prediction of phase relations among aqueous solutions and minerals: Salton Sea geothermal system. Geochim Cosmochim Ac 45:1479–1494

Bischoff JL (1991) Densities of liquids and vapors in boiling NaCl–H_2O solutions: a PVTX summary from 300° to 500 °C. Am J Sci 291:309–338

Bischoff JL, Rosenbauer RJ (1985) An empirical equation of state for hydrothermal seawater (3.2 percent NaCl). Am J Sci 285:725–763

Blasco M, Gimeno MJ, Auqué LF (2018) Low temperature geothermal systems in carbonate-evaporitic rocks: mineral equilibria assumptions and geothermometrical calculations. Insights from the Arnedillo thermal waters (Spain). Sci Total Environ 615:526–539

Blasco M, Auqué LF, Gimeno MJ, Acero P, Gómez J, Asta MP (2019) Mineral equilibria and thermodynamic uncertainties in the geothermometrical characterisation of carbonate geothermal systems of low temperature. The case of the Alhama-Jaraba system (Spain). Geothermics 78:170–182

Bödvarsson G (1960) Exploration and exploitation of natural heat in Iceland. B Volcanol 23:241–250

Bödvarsson G, Palmason G (1961) Exploration of subsurface temperature in Iceland. In: Geothermal energy. Proceedings of I: UN conference new sources energy, Rome 1961, vol 2, pp 91–98

Bowers TS, Jackson KJ, Helgeson HC (1984) Equilibrium activity diagrams for coexisting minerals and aqueous solutions at pressures and temperatures to 5 kb and 600 °C. Springer, 397pp

Brown ST, Kennedy BM, De Paolo DJ, Hurwitz S, Evans WC (2013) Ca, Sr, O and D isotope approach to defining the chemical evolution of hydrothermal fluids: example from Long Valley, CA, USA. Geochim Cosmochim Ac 122:209–225

Browne PRL (1970) Hydrothermal alteration as an aid in investigating geothermal fields. Geothermics 2:564–570

Browne PRL (1978) Hydrothermal alteration in active geothermal fields. Annu Rev Earth Pl Sci 6:229–248

Can I (2002) A new improved Na/K geothermometer by artificial neural networks. Geothermics 31:751–760

Capuano RM, Cole DR (1982) Fluid-mineral equilibria in a hydrothermal system, Roosevelt Hot Springs, Utah. Geochim Cosmochim Ac 46:1353–1364

Chiodini G, Cioni R, Guidi M, Marini L (1991) Chemical geothermometry and geobarometry in hydrothermal aqueous solutions: a theoretical investigation based on a mineral-solution equilibrium model. Geochim Cosmochim Ac 55:2709–2727

Chiodini G, Frondini F, Marini L (1995) Theoretical geothermometers and P_{CO2} indicators for aqueous solutions coming from hydrothermal systems of medium-low temperature hosted in carbonate-evaporite rocks. Application to the thermal springs of the Etruscan Swell, Italy. Appl Geochem 10:337–346

Christenson BW (1997) Kawerau geothermal field: geochemical structure of the reservoir and its response to exploitation. Geoth Res T 21:17–24

Crerar DA, Anderson GM (1971) Solubility and solvation reactions of quartz in dilute hydrothermal solutions. Chem Geol 8:107–122

Ellis AJ (1970) Quantitative interpretation of chemical characteristics of hydrothermal systems. Geothermics 2:516–528

Ellis AJ (1971) Magnesium ion concentrations in the presence of magnesium chlorite, calcite, carbon dioxide, quartz. Amer. J. Sci. 271:481–489

Ellis AJ, Mahon WAJ (1967) Natural hydrothermal systems and experimental hot water/rock interactions (part II). Geochim Cosmochim Ac 31:519–538

Fleming BA, Crerar DA (1982) Silicic acid ionization and calculation of silica solubility at elevated temperature and pH. Application to geothermal fluid processing and reinjection. Geothermics 11:15–29

Fouillac C, Michard G (1981) Sodium/lithium ratios in water applied to geothermometry of geothermal reservoirs. Geothermics 10:55–70

Fournier RO (1960) Solubility of quartz in water in the temperature interval from 25 to 300 °C. Geol Soc Am Bull 71:1867–1868

Fournier RO (1973) Silica in thermal waters: laboratory and field investigations. In: Proceedings international symposium on hydrogeochemistry and biogeochemistry, Tokyo, pp 122–139

Fournier RO (1977) Chemical geothermometers and mixing models for geothermal systems. Geothermics 5:41–50

Fournier RO (1979) A revised equation for the Na/K geothermometer. Geotherm Res Counc Trans 5:1–16

Fournier RO (1981) Application of water geochemistry to geothermal exploration and reservoir engineering (Chapter 4). In: Rybach L, Muffler LJP (eds) Geothermal systems: principles and case histories. Wiley, New York, pp 109–143

Fournier RO, Potter RW II (1982a) An equation correlating the solubility of quartz in water from 25° to 900°C at pressures up to 10,000 bars. Geochim Cosmochim Ac 46: 1969–1973

Fournier RO, Potter RW II (1982b) A revised and expanded silica (quartz) geothermometer. Geot Res Council Bull 11:3-12 (see also correction in vol. 12, page 32)

Fournier RO (1991) Water geothermometers applied to geothermal energy. Appl. Geochem. Geotherm. Reservoir Dev 37–69 (F. D'Amore, co-ordinator), UNITAR

Fournier RO, Potter RW (1979) Magnesium correction to the Na–K–Ca chemical geothermometer. Geochim Cosmochim Ac 43:1543–1550

Fournier RO, Rowe JJ (1962) The solubility of cristobalite along the three-phase curve, gas plus liquid plus cristobalite. Am Mineral 47:897–902

Fournier RO, Rowe JJ (1966) Estimation of underground temperatures from the silica content of water from hot springs and wet-steam wells. Am J Sci 264:685–697

Fournier RO, Truesdell AH (1970) Chemical indicators of subsurface temperature applied to hot spring waters of Yellowstone National Park, Wyoming, USA. Geothermics 2:529–535

Fournier RO, Truesdell AH (1973) An empirical Na–K–Ca geothermometer for natural waters. Geochim Cosmochim Ac 37:1255–1275

Fournier RO, White DE, Truesdell AH (1974) Geochemical indicators of subsurface temperature. Part I. Basic assumptions. J Res US Geol Surv 2:259–262

Fournier RO, Rosenbauer RJ, Bischoff JL (1982) The solubility of quartz in aqueous sodium chloride solution at 350 °C and 180 to 500 bars. Geochim Cosmochim Ac 46:1975–1978

Ganeyev IG (1975) Solubility and crystallization of silica in chloride. Doklady Acad Nauk SSSR 221:248–250 (citation from Shibue, 1996)

Giggenbach WF (1981) Geothermal mineral equilibria. Geochim Cosmochim Ac 45:393–410

Giggenbach WF (1984) Mass transfer in hydrothermal alterations systems. Geochim Cosmochim Ac 48:2693–2711

Giggenbach WF (1988) Geothermal solute equilibria. Derivation of Na–K–Mg–Ca geoindicators. Geochim Cosmochim Ac 52:2749–2765

Giggenbach WF (1991a) Chemical techniques in geothermal exploration. In Appl Geochem Geotherm Reservoir Dev 119–144 (F. D'Amore, co-ordinator), UNITAR

Giggenbach WF, Gonfiantini R, Jangi BL, Truesdell AH (1983) Isotopic and chemical composition of Parbati Valley geothermal discharges, NW-Himalaya, India. Geothermics 12:199–222

Gíslason SR, Heaney PJ, Oelkers EH, Schott J (1997) Kinetic and thermodynamic properties of moganite, a novel silica polymorph. Geochim Cosmochim Ac 61:1193–1204

Goguel RL (1983) The rare alkalies in hydrothermal alteration at Wairakei and Broadlands geothermal fields, NZ. Geochim Cosmochim Ac 47:429–437

Guidi M, Marini L, Scandiffio G, Cioni R (1990) Chemical geothermometry in hydrothermal aqueous solutions: the influence of ion complexing. Geothermics 19:415–441

Gunnarsson I, Arnórsson S (2000) Amorphous silica solubility and the thermodynamic properties of $H_4SiO_4{}^\circ$ in the range of 0° to 350 °C at P_{sat}. Geochim Cosmochim Ac 64:2295–2307

Heitmann HG (1965) Die Löslichkeit von Kieselsäure in Wasser und Wasserdampf. Glastech. Ber.-Glass 38:41–54

Helgeson HC (1968) Evaluation of irreversible reactions in geochemical processes involving minerals and aqueous solutions: I. Thermodynamic relations. Geochim Cosmochim Acta 32:853–877

Helgeson HC (1969) Thermodynamics of hydrothermal systems at elevated temperatures and pressures. Am J Sci 267:729–804

Helgeson HC, Brown TH, Nigrini A, Jones TA (1970) Calculation of mass transfer in geochemical processes involving aqueous solutions. Geochim Cosmochim Acta 34:569–592

Helgeson HC, Delany JM, Nesbitt HW, Bird DK (1978) Summary and critique of the thermodynamic properties of rock-forming minerals. Am J Sci 278A:229p

Helgeson HC, Garrels RM, Mackenzie FT (1969) Evaluation of irreversible reactions in geochemical processes involving minerals and aqueous solutions: II. Applications. Geochim Cosmochim Acta 33:455–481

Hemley JJ, Montoya JW, Marinenko JW, Luce RW (1980) Equilibria in the system Al_2O_3–SiO_2–H_2O and some general implications for alteration/mineralization processes. Econ Geol 75:210–228

Hyeong K, Capuano RM (2001) Ca/Mg of brines in Miocene/Oligocene clastic sediments of the Texas Gulf Coast: buffering by calcite/disordered dolomite equilibria. Geochim Cosmochim Ac 65:3065–3080

Ingebritsen SE, Sorey ML (1988) Vapor-dominated zones within hydrothermal systems: Evolution and natural state. J Geophys Res -Sol Ea 93(B11):13635–13655

James R (1968) Wairakei and Larderello: geothermal power systems compared. New Zeal. J Sci 11:706–719

Janecky DR, Charles RW, Bayhurst GK, Benjamin TM (1986) Physicochemical basis of the Na–K–Ca geothermometer. Los Alamos National Lab. Report No. LA-10806-MS, 10pp

Johnson JW, Oelkers EH, Helgeson HC (1992) SUPCRT 92: a software package for calculating the standard molal thermodynamic properties of minerals, gases, aqueous species, and reactions from 1 to 5000 bars and 0 to 1000 °C. Comput Geosci 18:899–947

Karingithi CW, Arnórsson S, Grönvold K (2010) Processes controlling aquifer fluid compositions in the Olkaria geothermal system, Kenya. J Volcanol Geoth Res 196:57–76

Kennedy GC (1950) A portion of the system silica-water. Econ Geol 45:629–653

Kharaka YK, Mariner RH (1989) Chemical geothermometers and their application to formation waters from sedimentary basins. In: Naeser ND, McCollon TH (eds) Thermal history of sedimentary basins. Springer, New York, pp 99–117

Kharaka YK, Lico MS, Law LM (1982) Chemical geothermometers applied to formation waters, Gulf of Mexico and California basins. Am Assoc Petr Geol B 66:588

Kharaka YK, Specht DJ, Carothers WW (1985) Low to intermediate subsurface temperatures calculated by chemical geothermometers. Am Assoc Petr Geol B 69:273

Khitarov NI (1956) The 400 °C isotherm for the system H_2O-SiO_2 at pressures up to 2,000 kg/cm^2. Geochem Int 1956:55–61

Kitahara S (1960) The solubility of quartz in water at high temperatures and high pressures. Rev Phys Chem Jpn 30:109–114

Lemmon EW, McLinden MO, Friend DG (2017) Thermophysical properties of fluid systems. In: Linstrom PJ, Mallard WG (eds) NIST chemistry webbook, NIST standard reference database number 69, National Institute of Standards and Technology, Gaithersburg MD. http://webbook.nist.gov/

Mackenzie FT, Gees R (1971) Quartz: synthesis at earth-surface conditions. Science 173:533–535

Mahon WAJ (1965) Calcium and magnesium in the natural thermal waters of New Zealand. New Zeal J Sci 8:66–78

Mahon WAJ (1966) Silica in hot water discharged from drillholes at Wairakei, New Zealand. New Zeal J Sci 9:135–144

Mahon WAJ (1970) Chemistry in the exploration and exploitation of hydrothermal systems. Geothermics 2:1310–1322

Manning CE (1994) The solubility of quartz in H_2O in the lower crust and upper mantle. Geochim Cosmochim Ac 58:4831–4839

Marini L (2006) Geological sequestration of carbon dioxide: Thermodynamics, kinetics, and reaction path modeling. In: Developments in geochemistry, vol 11. Elsevier, Amsterdam, 453pp

Marini L, Chiodini G, Cioni R (1986) New geothermometers for carbonate-evaporite geothermal reservoirs. Geothermics 15:77–86

Marini L, Cioni R, Guidi M (1998) Water chemistry of San Marcos area, Guatemala. Geothermics 27:331–360

Mercado S (1970) High activity hydrothermal zones detected by Na/K, Cerro Prieto, Mexico. Geothermics 2:1367–1376

Michard G (1990) Behaviour of major elements and some trace elements (Li, Rb, Cs, Sr, Fe, Mn, W, F) in deep hot waters from granitic areas. Chem Geol 89:117–134

Michard G, Fouillac C (1976) Remarques sur le geothermometre Na–K–Ca. J Volcanol Geoth Res 1:297–304

Michard G, Fouillac C, Grimaud D, Denis J (1981) Une méthode globale d'estimation des températures des resérvoirs alimentant les sources thermales. Exemple du Massif Central Français. Geochim Cosmochim Ac 45:1199–1207

Morey GW, Hesselgesser JM (1951a) The solubility of quartz and some other substances in superheated steam at high pressures. Am Soc Mech Eng Trans 73:864–875

Morey GW, Hesselgesser JM (1951b) The solubility of some minerals in superheated steam at high pressures. Econ Geol 46:821–835

Morey GW, Fournier RO, Rowe JJ (1962) The solubility of quartz in water in the temperature interval from 25° to 300 °C. Geochim Cosmochim Ac 26:1029–1043

Nieva D, Nieva R (1987) Developments in geothermal energy in Mexico—part twelve. A cationic geothermometer for prospecting of geothermal resources. Heat Recov Syst CHP 7:243–258

Novgorodov PG (1975) Solubility of quartz in H_2O-CO_2 mixtures at 700 °C and pressures of 3 and 5 kbar. Geochem Int 12:122–126

Novgorodov PG (1977) On the solubility of quartz in $H_2O + CO_2$ and $H_2O + NaCl$ at 700 °C and 1.5 kb pressure. Geochem Int 14:191–193

Opondo KM (2015) Carbonate scale formed in well OW-202 in Olkaria central field, Kenya. In: Proceedings world geothermal congress 2015, Melbourne, Australia, 19–25 Apr 2015, 10pp

Paces T (1975) A systematic deviation from Na–K–Ca geothermometer below 75 °C and above 10^{-4} atm P_{CO2}. Geochim Cosmochim Ac 39:541–544

Pieri S, Sabatelli F, Tarquini B (1989) Field testing results of downhole scale inhibitor injection. Geothermics 18:249–257

Pope LA, Hajash A, Popp RK (1987) An experimental investigation of the quartz, Na–K, Na–K–Ca geothermometers and the effects of fluid composition. J Volcanol Geoth Res 31:151–161

Puigdomènech I, Rard JA, Plyasunov AV, Grenthe I (1997) Temperature corrections to thermodynamic data and enthalpy calculations. In: I. Grenthe and I. Puigdomènech (Eds.) Modelling in Aquatic Chemistry, NEA-OECD Publications, Paris 427–493

Ragnarsdóttir KV, Walther JV (1983) Pressure sensitive "silica geothermometer" determined from quartz solubility experiments at 250 °C. Geochim Cosmochim Acta 47:941–946

Reyes AG (1990) Petrology of Philippine geothermal systems and the application of alteration mineralogy to their assessment. J Volcanol Geoth Res 43:279–309

Reyes AG, Giggenbach WF, Saleras JRM, Salonga ND, Vergara MC (1993) Petrology and geochemistry of Alto Peak, a vapor-cored hydrothermal system, Leyte Province, Philippines. Geothermics 22:479–519

Rimstidt JD (1997) Quartz solubility at low temperatures. Geochim Cosmochim Ac 61:2553–2558

Santoyo E, Díaz-González L (2010) A new improved proposal of the Na/K geothermometer to estimate deep equilibrium temperatures and their uncertainties in geothermal systems. In: Proceedings world geothermal congress 2010, Bali, Indonesia, 25–29 Ap 2010, 9pp

Semenova AI, Tsiklis DS (1970) Solubility of silicon dioxide in steam at high pressures and temperatures. Russ J Phys Chem 44:1420–1422

Serpen G, Palabiyik Y, Serpen U (2009) An artificial neural network model for Na/K geothermometer. In: Proceedings, 34th workshop on geothermal reservoir engineering, Stanford University, Stanford, California, 9–11 Feb 2009, SGP-TR-187, 12pp

Seward TM (1974) Determination of the first ionization constant of silicic acid from quartz solubility in borate buffer solutions to 350 C. Geochim Cosmochim Ac 38:1651–1664

Seyfried WE, Gordon PC, Dickson FW (1979) A new reaction cell for hydrothermal solution equipment. Am Mineral 64:646–649

Sheppard DS (1984) Fluid chemistry of Ngawha reservoir. Proceedings of the 6th New Zealand geothermal workshop, pp 151–154

Shibue Y (1996) Empirical expressions of quartz solubility in H_2O, $H_2O + CO_2$, and $H_2O + NaCl$ fluids. Geochem J 30:339–354

Shikazono N (1976) Thermodynamic interpretation of Na–K–Ca geothermometer in the natural water system. Geochem J 10:47–50

Shikazono N (1978) Possible cation buffering in chloride-rich geothermal waters. Chem Geol 23:239–254

Shock EL, Helgeson HC (1988) Calculation of the thermodynamic and transport properties of aqueous species at high pressures and temperatures: correlation algorithms for ionic species and equation of state predictions to 5 kb and 1000 °C. Geochim Cosmochim Ac 52:2009–2036

Shock EL, Helgeson HC, Sverjensky DA (1989) Calculation of the thermodynamic and transport properties of aqueous species at high pressures and temperatures: standard partial molal properties of inorganic neutral species. Geochim Cosmochim Ac 53:2157–2183

Siever R (1962) Silica solubility, 0-200 °C, and the diagenesis of siliceous sediments. J Geol 70:127–150

Simmons SF (2013) Fluid-mineral equilibria in Great Basin geothermal systems: implications for chemical geothermometry. In: Proceedings of the 38th workshop on geothermal reservoir engineering, Stanford University, Stanford, California, February 11–13, 2013, SGP-TR-198, 8 pp

Simmons SF, Christenson BW (1994) Origins of calcite in a boiling geothermal system. Am J Sci 294:361–400

Sommerfeld RA (1967) Quartz solution reaction: 400°–500 °C, 1000 bars. J Geophys Res 72(16):4253–4257

Tarcan G, Özen T, Gemici Ü, Çolak M, Karamanderesi İH (2016) Geochemical assessment of mineral scaling in Kızıldere geothermal field, Turkey. Environ Earth Sci 75:1317 (19pp)

Tassew M (2010) Maintenance and operational experience gained by operating the Aluto Langano geothermal pilot power plant. In: Proceedings world geothermal congress 2010, Bali, Indonesia, 25–29 Apr 2010, 4pp

Tonani F (1980) Some remarks on the application of geochemical techniques in geothermal exploration. In: Proceedings of 2nd symposium advances in European geothermal research, Strasbourg, pp 428–443

Truesdell A.H. (1976) Summary of section III—Geochemical techniques in exploration. In Proceedings of 2nd UN symposium on the development and use of geothermal resources, vol 1, pp 53–79

Truesdell AH, Fournier RO (1977) Procedure for estimating the temperature of a hot-water component in a mixed water by using a plot of dissolved silica versus enthalpy. U.S. Geol. Surv. J. Res. 5:49–52

Van Lier J, Bruyn PD, Overbeek JTG (1960) The solubility of quartz. J Phys Chem-US 64:1675–1682

Verma SP, Santoyo E (1997) New improved equations for Na/K, Na/Li and SiO_2 geothermometers by outlier detection and rejection. J Volcanol Geoth Res 79:9–23

Vespasiano G, Apollaro C, Muto F, Dotsika E, De Rosa R, Marini L (2014) Chemical and isotopic characteristics of the warm and cold waters of the Luigiane Spa near Guardia Piemontese (Calabria, Italy) in a complex faulted geological framework. Appl Geochem 41:73–88

Viveiros PV (2014) Calcium carbonate scaling control in geothermal well PV8 in Sao Miguel, Azores, combining chemical inhibition and mechanical reaming. UNU-GTP Rep 33:721–744

Von Damm KL, Bischoff JL, Rosenbauer RJ (1991) Quartz solubility in hydrothermal seawater: An experimental study and equation describing quartz solubility for up to 0.5 M NaCl solutions. Am J Sci 291:977–1007

Walshe JL (1986) A six-component chlorite solid solution model and the conditions of chlorite formation in hydrothermal and geothermal systems. Econ Geol 81:681–703

Walther JV, Orville PM (1983) The extraction-quench technique for determination of the thermodynamic properties of solute complexes: application to quartz solubility in fluid mixtures. Am Mineral 68:731–741

Weill DF, Fyfe WS (1964) The solubility of quartz in H_2O in the range 1000–4000 bars and 400–550 °C. Geochim Cosmochim Ac 28:1243–1255

White DE (1965) Saline waters of sedimentary rocks. In: Fluids in subsurface environments pp 342–366

White DE (1968) Environments of generation of some base-metal ore deposits. Econ Geol 63:301–335

White DE, Muffler LJP, Truesdell AH (1971) Vapor-dominated hydrothermal systems compared with hot-water systems. Econ Geol, 66:75–97

Wolery TJ (1992) EQ3NR, a computer program for geochemical aqueous speciation-solubility calculations: theoretical manual, user's guide and related documentation (version 7.0). Report UCRL-MA-110662 PT III. Lawrence Livermore National Laboratory, Livermore

Wolery TW, Jove-Colon C (2007) Qualification of thermodynamic data for geochemical modeling of mineral-water interactions in dilute systems. Sandia National Laboratories Report ANL-WIS-GS-000003 REV 01

Wyart J, Sabatier G (1955) Nouvelles mesures de la solubilité du quartz, de la tridymite et de la cristobalite dans l'eau sous pression au-dessus de la temperature critique. CR Hebd Acad Sci 240:1905–1907

Yoshida Y (1991) Geochemistry of the Nigorikawa geothermal system, southwest Hokkaido, Japan. Geochem J 25:203–222

Zheng X, Duan C, Xia B, Jiang Y, Wen J (2019) Hydrogeochemical modeling of the shallow thermal water evolution in Yangbajing geothermal field, Tibet. J Earth Sci 30:870–878

Zhiqian G, Bingsong Y, Xingyun L (2007) The equilibrium between diagenetic calcites and dolomites and its impact on reservoir quality in the sandstone reservoir of Kela 2 gas field. Prog Nat Sci 17:1051–1058